

*Study of the fundamentals of nucleation and growth mechanism behind the formation of titania nanostructures for photovoltaic application*

Thesis submitted to AcSIR  
for the Award of the degree of

**DOCTOR OF PHILOSOPHY**  
**in**  
**Chemical Sciences**



**By**  
**Subha Sadhu**

(Enroll. no. 10CC11J26016)

**Under the guidance of**  
**Dr. Pankaj Poddar**

*Physical & Material Chemistry Division,  
CSIR-NATIONAL CHEMICAL LABORATORY,  
PUNE-411008, INDIA.*

*August, 2014*

## **CERTIFICATE**

*This is to certify that the work incorporated in the thesis entitled: “Study of the fundamentals of nucleation and growth mechanism behind the formation of titania nanostructures for photovoltaic application”, submitted by Ms. Subha Sadhu, for the degree of Doctor of Philosophy in Chemical Sciences, was carried out under my supervision at the Physical and Materials Chemistry Division, CSIR-National Chemical Laboratory, Pune, India. Such materials as have been obtained from other sources have been duly acknowledged. To the best of my knowledge, the present work or any part thereof has not been submitted to any other University for the award of any other degree or diploma.*

Date:

**Dr. Pankaj Poddar**

Place: Pune

Research guide

## **DECLARATION**

*I, hereby declare that this thesis entitled “Study of the fundamentals of nucleation and growth mechanism behind the formation of titania nanostructures for photovoltaic application” is entirely original and was carried out by me under the supervision of Dr. Pankaj Poddar in the Physical and Materials Chemistry Division, NCL, Pune. Any material borrowed from other sources has been duly acknowledged. The work is original and has not been submitted in part or full by me for the award of any degree or diploma of any University or Institution.*

Date:

**Subha Sadhu**

Place

(Research student)

*Dedicated to my world,  
my parents Aparna & Sujit Sadhu  
&  
The almighty God*

## Acknowledgement

*During my PhD days, I came across with so many nice people, without whom, it is not possible to complete the work. I would like to take the opportunity to express my gratitude to all of them.*

*First of all, I would like to thank my guide Dr. Pankaj Poddar for giving me the opportunity to work with him and for his continuous encouragement and spirited thinking to do better. He always encouraged me in various ways to achieve the goal. For him only, it has been possible for me to become independent in all sorts of life. I will treasure the experience of working with him.*

*I owe my gratitude to all my DAC members Dr. Sudip Roy, Dr. C.S. Gopinath, Dr. Suresh Bhat and Dr. Shouvik Dutta for their time, guidance, motivation and constructive criticism.*

*I am highly thankful to Mrs. Suguna Adhyanthaya for helping me to learn TGA and her support for solving any problem.*

*I would like to thank my seniors Ramya, Umesh, Imran, Adhish, Raja, Tuhin, Vivek for getting me familiarized with all the lab facilities and their helping nature. I am grateful to Priya to make me feel like home and always be with me in my initial PhD days. Special thanks goes to all my lab mates and juniors Neetu, Subhadip, Aanchal, Asha, Preeti, Preeti P, Mousumi, Puneet, Samir and Anupam for always standing by my side and for the pleasant working environment. I am extremely thankful to Preeti and Puneet for helping me to prepare the diagrams.*

*I am truly grateful to have Preeti, Mousumi and Preeti P as my friends :) more than lab mates and always bear me and the special bonding we share. Thank you for keeping my parents relieved as they know, if any trouble arise, you all are always ready to assist me any time.*

*I am thankful to Dr. S. B. Ogale, Dr. S. K. Asha, Dr. C. S. Gopinath, Dr. K. Patil, Dr. Shouvik Dutta, Dr. Rahul Banerjee for allowing me to use their lab instruments for my research work.*

*This thesis will be incomplete without thanking Shruti, Mukta, Vivek, Omkar, Joyasish da, Sandeep, Prajitha, Koushal, Chinmay, Nisha, Kanak, Manoj, Anil, Puspanjali, Sharath, Arijit, Ketan and Anuj for their help to carry out various experiments.*

*I am thankful to all my project trainees Rima, Mousumi, Anindita, Karan, Vasudev, Vinay and Karishma for their enthusiasm in work which have been advantageous for me to improve the eminence of the work, presented in this thesis.*

*I feel honored to thank Dr. Anil Kumar, Dr. Sourav Pal and Dr. Sivram for providing me all the required facilities.*

*I want to thank all my roommates Kalyani, Beena, Neha, Nikita and Munmun. I am lucky to have such awesome roommates who are always there with me. I will always memorize all the midnight cooking, fun and chit chats.*

*I thank my friends Supriya, Shilpi, Supratik, Sharmin, Sanghamitra, Padma, Arnab, Satwik, Samayita, Mehaboob, Supriyo, Shyam and Sujoy for their spontaneous help, encouragement to complete the thesis and always cheering me in my dreadful temper. I am obliged to Sujoy for teaching me electrochemistry and all the fruitful discussions. I am really grateful to have such wonderful friends.*

*Last but not the least, I want to thank my parents from the bottom of my heart for everything I have. They are my life line. Without their continuous support and encouragement, it is impossible for me to spend even a single day in my life. Their curiosity towards my research work, motivates me to excel. I thank my Pisa, Bubai dada and Babui dada for their positive suggestions whenever I needed and my dida, thakuma and all the family members for their blessings.*

*Subha Sadhu*

# Table of contents

## Chapter I

### Introduction

|       |  |    |
|-------|--|----|
| 1.1   | Introduction   | 3  |
| 1.2   | Synthesis methods (solution based chemical techniques) | 3  |
| 1.2.1 | Sol-gel method   | 3  |
| 1.2.2 | Solvothermal/Hydrothermal method                       | 5  |
| 1.2.3 | Microwave method                                       | 7  |
| 1.2.4 | Micelle and Inverse Micelle Method                     | 7  |
| 1.2.5 | Electrodeposition                                      | 8  |
| 1.2.6 | Electrospinning  | 8  |
| 1.3   | Properties of TiO <sub>2</sub>                         | 9  |
| 1.3.1 | Crystal structure                                      | 9  |
| 1.3.2 | Optical properties                                     | 12 |
| 1.3.3 | Electronic properties                                  | 13 |
| 1.4   | Growth mechanism                                       | 15 |
| 1.4.1 | Effect of solvent                                      | 16 |
| 1.4.2 | Effect of surfactant                                   | 17 |
| 1.4.3 | Effect of pH   | 17 |
| 1.5   | Modification of TiO <sub>2</sub> nanostructures        | 18 |
| 1.5.1 | Synthesis of metal doped nanostructures                | 18 |
| 1.5.2 | Synthesis of nonmetal doped nanostructures             | 19 |

|         |  |    |
|---------|--|----|
| 1.5.3   | Properties of metal doped TiO <sub>2</sub> nanostructures          | 20 |
| 1.5.4   | Properties of nonmetal doped TiO <sub>2</sub> nanostructures       | 21 |
| 1.5.5   | Synthesis of metal-TiO <sub>2</sub> composite                      | 21 |
| 1.5.6   | Synthesis of branched TiO <sub>2</sub> nanostructures              | 22 |
| 1.6     | Application of TiO <sub>2</sub> nanostructures                     | 23 |
| 1.6.1   | Photovoltaic applications  | 23 |
| 1.6.1.1 | DSSC based on 1D TiO <sub>2</sub> nanostructures                   | 26 |
| 1.6.1.2 | Comparison of rutile and anatase based TiO <sub>2</sub> solarcells | 26 |
| 1.6.1.3 | DSSC based on doped and composite TiO <sub>2</sub> nanostructures  | 27 |
| 1.6.2   | Photocatalytic applications  | 27 |
| 1.6.3   | Photocatalytic water splitting                                     | 29 |
| 1.6.4   | Batteries and supercapacitors                                      | 29 |
| 1.6.5   | Electrochromic devices   | 30 |
| 1.7     | Thesis outline   | 30 |
| 1.8     | References   | 33 |

## **Chapter II**

### **Understanding the nucleation and growth mechanism of single crystalline TiO<sub>2</sub> nanorods on transparent conducting oxide substrate**

|       |   |    |
|-------|---|----|
| 2.1   | Introduction  | 44 |
| 2.2   | Materials and method                                      | 46 |
| 2.2.1 | Synthesis of TiO <sub>2</sub> NRs on different substrates | 46 |
| 2.2.2 | Fabrication of DSSC                                       | 47 |

|         |   |    |
|---------|---|----|
| 2.2.3   | Characterization techniques                               | 48 |
| 2.3     | Results and Discussion                                    | 49 |
| 2.3.1   | XRD analysis  | 49 |
| 2.3.2   | Determination of shape and size                           | 50 |
| 2.3.2.1 | SEM analysis  | 50 |
| 2.3.2.2 | TEM analysis  | 51 |
| 2.3.3   | Growth mechanism  | 52 |
| 2.3.3.1 | XPS analysis  | 53 |
| 2.3.4   | Optical properties  | 55 |
| 2.3.4.1 | UV-vis analysis   | 55 |
| 2.3.4.2 | PL analysis   | 56 |
| 2.3.5   | Growth of TiO <sub>2</sub> NRs on Au-coated FTO substrate | 57 |
| 2.3.5.1 | SEM analysis  | 57 |
| 2.3.5.2 | STM analysis  | 57 |
| 2.3.5.3 | XRD analysis  | 60 |
| 2.3.5.4 | SEM analysis  | 60 |
| 2.3.5.5 | Contact angle measurement                                 | 61 |
| 2.3.6   | Photovoltaic properties                                   | 62 |
| 2.4     | Conclusion  | 63 |
| 2.5     | References  | 65 |

## Chapter III

### **Growth of surfactant free 3D TiO<sub>2</sub> microsphere assembly on transparent conducting oxide substrate for photovoltaic and photocatalytic applications**

|         |  |    |
|---------|--|----|
| 3.1     | Introduction   | 70 |
| 3.2     | Materials and method   | 72 |
| 3.2.1   | Materials  | 72 |
| 3.2.2   | Synthesis of 3D-TiO <sub>2</sub> nanoflowers on FTO substrates | 72 |
| 3.2.3   | Fabrication of DSSC  | 73 |
| 3.2.4   | Characterization techniques                                    | 73 |
| 3.3     | Results and Discussion   | 75 |
| 3.3.1   | X-Ray diffraction study  | 75 |
| 3.3.2   | Determination of shape and size                                | 77 |
| 3.3.2.1 | SEM analysis   | 77 |
| 3.3.2.2 | TEM analysis   | 78 |
| 3.3.3   | Growth mechanism   | 80 |
| 3.3.3.1 | Effect of time   | 80 |
| 3.3.3.2 | Effect of precursor  | 82 |
| 3.3.4   | Optical properties   | 83 |
| 3.3.4.1 | Photoluminescence study  | 83 |
| 3.3.4.2 | Raman study  | 84 |
| 3.3.5   | BET study  | 86 |

|       |                         |    |
|-------|-------------------------|----|
| 3.3.6 | Photovoltaic property   | 87 |
| 3.3.7 | Photocatalytic property | 89 |
| 3.3.8 | Wettability study       | 92 |
| 3.3.9 | Dielectric property     | 93 |
| 3.4   | Conclusion              | 94 |
| 3.5   | References              | 95 |

## **Chapter IV**

### **Study the growth mechanism and optoelectronic properties of La-doped TiO<sub>2</sub> nanorods for enhanced photoelectrochemical activity**

|         |   |     |
|---------|---|-----|
| 4.1     | Introduction  | 100 |
| 4.2     | Materials and method  | 101 |
| 4.2.1   | Synthesis of TiO <sub>2</sub> and La-doped TiO <sub>2</sub> NRs on FTO substrates | 102 |
| 4.2.2   | Fabrication of DSSC   | 102 |
| 4.2.3   | Characterization techniques   | 102 |
| 4.3     | Results and discussion  | 103 |
| 4.3.1   | X-Ray diffraction study   | 103 |
| 4.3.2   | Determination of shape and size   | 105 |
| 4.3.2.1 | SEM analysis  | 105 |
| 4.3.2.2 | TEM analysis  | 109 |
| 4.3.2.3 | STEM analysis   | 111 |
| 4.3.3   | Optical properties  | 112 |

|         |                         |     |
|---------|-------------------------|-----|
| 4.3.3.1 | UV-vis-DRS spectra      | 112 |
| 4.3.3.2 | Photoluminescence study | 114 |
| 4.3.3.3 | Raman study             | 115 |
| 4.3.4   | Electrochemical study   | 116 |
| 4.3.5   | Photovoltaic property   | 118 |
| 4.4     | Conclusion              | 120 |
| 4.5     | References              | 121 |

## **Chapter V**

### **In situ synthesis of one dimensional TiO<sub>2</sub> – MWCNT nanocomposites and study their optoelectronic properties for photovoltaic applications**

|       |  |     |
|-------|--|-----|
| 5.1   | Introduction   | 125 |
| 5.2   | Materials and method   | 126 |
| 5.2.1 | Materials  | 126 |
| 5.2.2 | Synthesis of TiO <sub>2</sub> and TiO <sub>2</sub> -MWCNT composites | 126 |
| 5.2.3 | Fabrication of DSSC  | 127 |
| 5.2.4 | Characterization techniques  | 128 |
| 5.3   | Results and discussion   | 129 |
| 5.3.1 | XRD analysis   | 129 |
| 5.3.2 | Raman study  | 131 |
| 5.3.3 | XPS study  | 132 |
| 5.3.4 | TGA study  | 134 |
| 5.3.5 | FESEM study  | 135 |

|         |                    |     |
|---------|--------------------|-----|
| 5.3.6   | TEM analysis       | 136 |
| 5.3.7   | Optical properties | 139 |
| 5.3.7.1 | UV-vis-DRS spectra | 139 |
| 5.3.7.2 | PL study           | 140 |
| 5.3.8   | Mott-Schotky study | 141 |
| 5.3.9   | BET study          | 143 |
| 5.3.10  | Photovoltaic study | 144 |
| 5.4     | Conclusion         | 146 |
| 5.5     | References         | 147 |

## **Chapter VI**

### **Conclusion**

|     |                        |     |
|-----|------------------------|-----|
| 6.1 | Summary of the work    | 151 |
| 6.2 | Scope for future study | 153 |

### **List of publications**

## List of figures

---

- Fig. 1.1:** Schematic of a solvothermal method.
- Fig. 1.2:** Schematic of the formation of TiO<sub>2</sub> network.
- Fig. 1.3:** Schematic of the cell structure of three TiO<sub>2</sub> polymorphs.
- Fig. 1.4:** Equilibrium crystal shape of rutile and anatase TiO<sub>2</sub>.
- Fig. 1.5:** Different shapes of rutile and anatase crystals.
- Fig. 1.6:** Bonding diagram of TiO<sub>2</sub>.
- Fig. 1.7:** Schematic of oriented attachment mechanism.
- Fig. 1.8:** Schematic of the operational principle of DSSC.
- Fig. 1.9:** Outline of a dye-sensitized solar cell constructed with a working electrode consisting of dye-sensitized semiconducting oxide film, a counter electrode made of platinum-coated glass substrate, and electrolyte filled between the working and counter electrodes.
- Fig. 1.10:** Schematic of photocatalytic activation using TiO<sub>2</sub> nanoparticles.
- Fig. 2.1:** Schematic of the synthesis of oriented TiO<sub>2</sub> NRs on substrate.
- Fig. 2.2:** XRD pattern of rutile TiO<sub>2</sub> NRs grown on (A) (FTO) (B) FSO glass substrate.
- Fig. 2.3:** SEM images of TiO<sub>2</sub> NRs (A) grown on FTO coated glass substrate (top view) (B) (cross-sectional view), (C) FSO substrate.
- Fig. 2.4:** (A) TEM image (B) HRTEM image with inset showing FFT pattern (C) selected area electron diffraction pattern of single TiO<sub>2</sub> NR grown on FTO glass substrate. (D) TEM image (E) HRTEM image with inset showing FFT pattern (F) selected area electron diffraction pattern of single TiO<sub>2</sub> nanorod grown on FSO substrate.
- Fig. 2.5:** XPS spectra of O 1s core level for TiO<sub>2</sub> NRs grown on (A) FTO (B) FSO glass substrates.

- Fig. 2.6:** UV-visible absorption spectra of TiO<sub>2</sub> NRs grown on FTO and FSO glass substrates. The inset shows the dependence of the absorption coefficient as a function of  $h\nu$  for the TiO<sub>2</sub> NRs.
- Fig. 2.7:** PLE and photoluminescence (PL) of TiO<sub>2</sub> NRs grown on FTO and FSO glass substrates.
- Fig. 2.8:** SEM images of (A) FTO substrate and (B) 10 nm Au coated FTO substrate.
- Fig. 2.9:** The top panel shows the STM height image on FTO substrate and the bottom panel shows the line scan analysis on the lines show in the top image. The respective line colors represent the marks in the top image where the analysis was done in top image.
- Fig. 2.10:** The top panel shows the STM height image on 10 nm Au-coated FTO substrate and the bottom panel shows the line scan analysis on the lines show in the top image. The respective line colors represent the marks in the top image where the analysis was done in top image.
- Fig. 2.11:** XRD pattern of TiO<sub>2</sub> NRs grown on 10 nm gold coated FTO substrate.
- Fig. 2.12:** SEM images of TiO<sub>2</sub> NRs grown on 10 nm gold coated FTO substrate.
- Fig. 2.13:** Water contact angle measurement of (A) FTO glass substrate (B) 10 nm gold coated FTO glass substrate.
- Fig. 2.14:** Current density vs. potential curves for dye sensitized solar cell fabricated from TiO<sub>2</sub> NRs grown on FTO glass substrate.
- Fig. 3.1:** XRD patterns of 3D rutile TiO<sub>2</sub> microspheres directly grown on FTO substrate with different reaction time.
- Fig. 3.2:** (A)–(D) SEM images of 3D rutile TiO<sub>2</sub> microspheres grown on FTO substrate after 8 h of hydrothermal reaction with different magnifications.
- Fig. 3.3:** (A)–(D) TEM micrograph of TiO<sub>2</sub> NWs of a microsphere with different magnifications.
- Fig. 3.4:** (A)–(C) TEM images of single TiO<sub>2</sub> NWs with different magnifications. (D) FFT pattern of the NW.

- Fig. 3.5:** (A)–(F) SEM images of 3D rutile TiO<sub>2</sub> microspheres grown on FTO substrates with varying reaction time.
- Fig. 3.6:** (A)–(F) SEM images of rutile TiO<sub>2</sub> grown on FTO substrate using different precursors (A, B) TiCl<sub>4</sub>, (C, D) Ti(OBu)<sub>4</sub>.
- Fig. 3.7:** PLE and PL spectra of TiO<sub>2</sub> microspheres grown on FTO substrate after 2 and 10 h of hydrothermal reaction.
- Fig. 3.8:** Raman spectra for TiO<sub>2</sub> grown on FTO substrate for 2 and 10 h of hydrothermal reaction.
- Fig. 3.9:** N<sub>2</sub> adsorption and desorption isotherm of TiO<sub>2</sub> grown on FTO substrate for 2 and 10 h of hydrothermal reaction.
- Fig. 3.10:** UV-vis absorption spectra for the dye adsorbed TiO<sub>2</sub> photoanode grown on FTO substrate for 2 and 10 h of hydrothermal reaction.
- Fig. 3.11:** Current density vs. potential curves for dye sensitized solar cell fabricated from TiO<sub>2</sub> grown on FTO substrate for 2 and 10 h of hydrothermal reaction.
- Fig. 3.12:** (A) UV-vis absorption spectra, (B) photocatalysis degradation profiles of RhB as a function of time in sunlight, (C) Photocatalytic degradation of RhB dye up to three cycles and (D) kinetic plot of photocatalytic degradation.
- Fig. 3.13:** Water contact angle measurement of TiO<sub>2</sub> microspheres grown on FTO substrate after 10 h of hydrothermal reaction.
- Fig. 3.14:** Room temperature dielectric permittivity and (B) loss tangent as a function of frequency for as-prepared TiO<sub>2</sub> microspheres grown on FTO substrate after 10 h of hydrothermal treatment.
- Fig. 4.1:** XRD patterns of pure TiO<sub>2</sub> and La-doped TiO<sub>2</sub> NRs with various amounts of doping. 1La\_TiO<sub>2</sub>, 2La\_TiO<sub>2</sub>, 3La\_TiO<sub>2</sub> and 4La\_TiO<sub>2</sub> denote the samples where the added amount of La(NO<sub>3</sub>)<sub>3</sub>·6H<sub>2</sub>O was 1, 2, 3 and 4 mol% with respect to molar concentration of TBOT.
- Fig. 4.2:** SEM images of (A) 1 (B) 2 (C) 3 and 4 mol % (D) La-doped TiO<sub>2</sub> NRs grown on FTO coated glass substrates (top view).

- Fig. 4.3:** SEM images of (A) 1 (B) 2 (C) 3 and 4 mol % (D) La-doped TiO<sub>2</sub> NRs grown on FTO coated glass substrates (cross-sectional view).
- Fig. 4.4:** (A) TEM image and (B) selected area electron diffraction pattern of 2 mol% La-doped single TiO<sub>2</sub> nanorod grown on FTO coated glass substrate. (C) HRTEM image of the nanorod. (D) FFT pattern of the nanorod. (E) Reciprocal lattice points not corresponding to the c-plane has been removed. (F) Results of IFFT based on the lattice points shown in (E).
- Fig. 4.5:** (A) STEM image of a representative 2 mol % La-doped TiO<sub>2</sub> nanorod. (B, C,) The corresponding elemental mapping of (B) Ti-K (C) La-M (100 nm scale bar for all). (D) Line scanning analysis across the single nanorod indicated by the line as shown in the inset (scale bar 50 nm).
- Fig. 4.6 :** (A) UV-visible DRS spectra, (B) the dependence of the absorption coefficient as a function of energy plot for pure TiO<sub>2</sub> and La-doped TiO<sub>2</sub> NRs with various amounts of doping.
- Fig. 4.7 :** PL spectra, for pure TiO<sub>2</sub> and La-doped TiO<sub>2</sub> NRs with various amounts of doping.
- Fig. 4.8:** Raman spectra, for pure TiO<sub>2</sub> and La-doped TiO<sub>2</sub> NRs with various amounts of doping.
- Fig. 4.9:** Mott-Schottky plots measured at a frequency of 10 kHz at 298 K in 3M KCl solution for TiO<sub>2</sub> and 2 and 3 mol% La-doped TiO<sub>2</sub> NRs.
- Fig. 4.10:** Current density vs. potential curves for dye sensitized solar cell fabricated from pure TiO<sub>2</sub> and La-doped TiO<sub>2</sub> NRs grown on FTO glass substrates.
- Fig. 5.1:** Schematic of the simultaneous synthesis of 1D-R-TiO<sub>2</sub>-MWCNT film and 1D-R- TiO<sub>2</sub>-MWCNT powder.
- Fig. 5.2:** XRD patterns of 1D rutile TiO<sub>2</sub>-MWCNT powder and film directly grown on FTO.
- Fig. 5.3:** Raman spectra for (A) 1D rutile TiO<sub>2</sub>-MWCNT powder, (B) 1D rutile TiO<sub>2</sub>-MWCNT film directly grown on FTO, (C) MWCNT and (D) rutile TiO<sub>2</sub>.

- Fig. 5.4:** (A) XPS survey spectra of TiO<sub>2</sub> and TiO<sub>2</sub>-MWCNT powder, (B) C 1s, (C) O 1s and (D) Ti 2p core level spectra of TiO<sub>2</sub>-MWCNT powder.
- Fig. 5.5:** TGA graph of TiO<sub>2</sub>, TiO<sub>2</sub>-MWCNT powder and MWCNT.
- Fig. 5.6:** FESEM images of 1D rutile TiO<sub>2</sub>-MWCNT film directly grown on FTO (A) cross-sectional view, (B) top view (C) zoom view of (B) and (D) 1D rutile TiO<sub>2</sub>-MWCNT powder.
- Fig. 5.7:** (A)–(D) TEM images of 1D rutile TiO<sub>2</sub>-MWCNT powder with different magnification.
- Fig. 5.8:** (A) HRTEM image with inset showing FFT pattern, (B) SAED pattern of 1D rutile TiO<sub>2</sub>-MWCNT powder, (C) masked reciprocal lattice points corresponding to (110) plane and (D) Results of IFFT based on the lattice points shown in (C).
- Fig. 5.9:** (A) UV-vis-DRS spectra with inset showing the dependence of the absorption coefficient as a function of energy plot for TiO<sub>2</sub> and 1D rutile TiO<sub>2</sub>-MWCNT film.
- Fig. 5.10:** PL spectra of TiO<sub>2</sub> and 1D rutile TiO<sub>2</sub>-MWCNT film.
- Fig. 5.11:** Mott-Schottky plots measured at a frequency of 10 kHz at 298 K in 3M KCl solution for TiO<sub>2</sub> and 1D rutile TiO<sub>2</sub>-MWCNT film.
- Fig. 5.12:** N<sub>2</sub> adsorption and desorption isotherm of TiO<sub>2</sub> and 1D rutile TiO<sub>2</sub>-MWCNT powder.
- Fig. 5.13:** Current density vs. potential curves for dye sensitized solar cell fabricated from TiO<sub>2</sub> and 1D rutile TiO<sub>2</sub>-MWCNT film.

## List of tables

---

- Table 4.1.** Structural properties of La-doped TiO<sub>2</sub> NRs grown on FTO substrate.
- Table 4.2.** EDX Analysis.
- Table 4.3.** Flat band potential ( $V_{FB}$ ) and donor density ( $N_d$ ) Of TiO<sub>2</sub> and La-doped TiO<sub>2</sub> NR.
- Table 4.4.** Photovoltaic Properties of DSSCs Assembled with TiO<sub>2</sub> and La-doped TiO<sub>2</sub> NRs.

## Abbreviations

---

|                                |  |
|--------------------------------|--|
| AAM                            | anodic alumina membrane                          |
| CVD                            | chemical vapor deposition                        |
| DMF                            | dimethyl formamide                               |
| DI                             | deionized  |
| DSSC                           | dye sensitized solar cell                        |
| EDX                            | energy disperse X-ray analysis                   |
| FFT                            | fast Fourier transform                           |
| FTO                            | fluorine doped tin oxide                         |
| H <sub>3</sub> PO <sub>4</sub> | phosphoric acid                                  |
| HNO <sub>3</sub>               | nitric acid                                      |
| HCl                            | hydrochloric acid                                |
| HF                             | hydrogen fluoride                                |
| H <sub>2</sub> SO <sub>4</sub> | sulfuric acid                                    |
| HVEM                           | high-voltage electron microscopy                 |
| HAADF                          | high-angle annular dark-field                    |
| HRTEM                          | high-resolution transmission electron microscope |
| J <sub>sc</sub>                | short-circuit current density                    |
| LiFePO <sub>4</sub>            | lithium iron phosphate                           |
| MB                             | methylene blue                                   |
| MWCNT                          | multiwalled carbon nanotube                      |

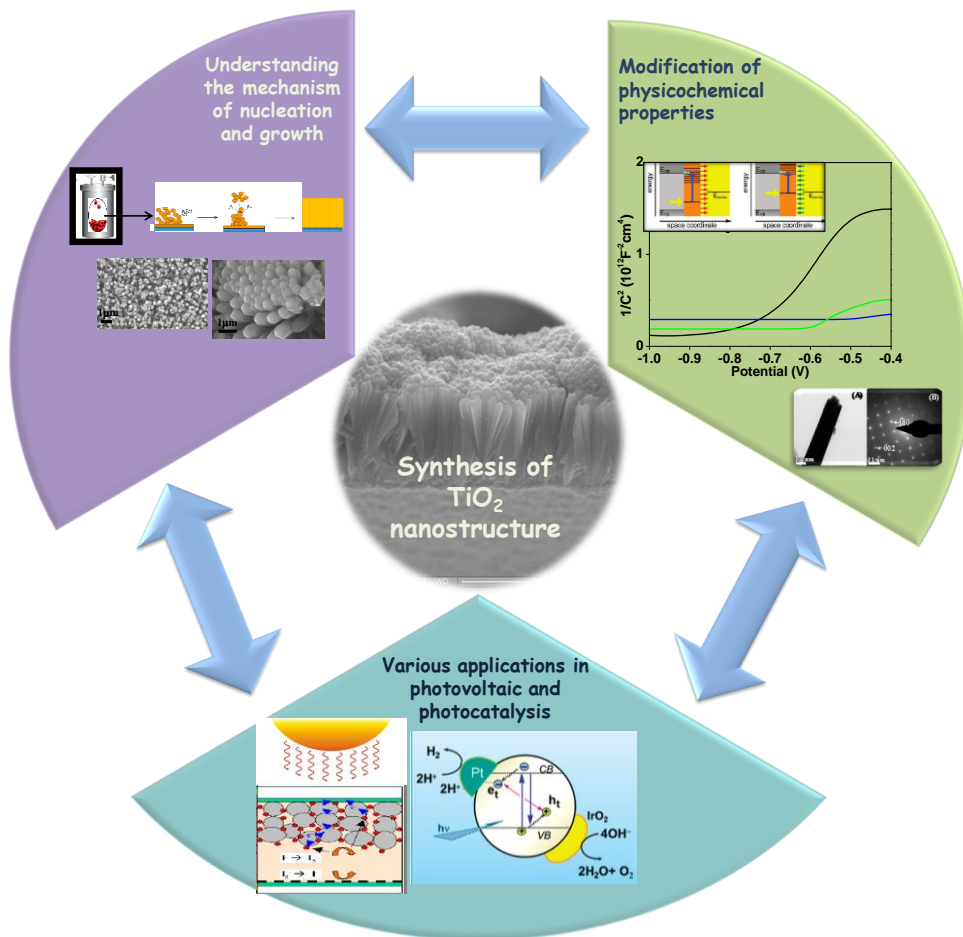
|                                 |  |
|---------------------------------|--|
| NC                              | nanocrystal  |
| NR                              | nanorod  |
| NW                              | nanowire   |
| NT                              | nanotube   |
| NP                              | nanoparticle   |
| NS                              | nanospheres  |
| NaOH                            | sodium hydroxide   |
| Na <sub>2</sub> SO <sub>4</sub> | sodium sulphate  |
| N719 dye                        | cisbis(isothiocyanato)bis(2,2'-bipyridyl-4-4'-dicarboxylato)-ruthenium(II)bis-tetrabutylammonium |
| OH <sup>-</sup>                 | hydroxyl ion   |
| PVA                             | polyvinyl acetate  |
| PL                              | photoluminescence  |
| PLE                             | photoluminescence excitation   |
| RT                              | room temperature   |
| STEM                            | scanning transmission electron microscopy  |
| STM                             | scanning tunneling microscopy  |
| SEM                             | scanning electron microscope   |
| SAED                            | selected area electron diffraction   |
| TTIP                            | titanium isopropoxide  |

|                                   |                                  |
|-----------------------------------|----------------------------------|
| TiO <sub>2</sub>                  | titania                          |
| TiCl <sub>4</sub>                 | titanium tetrachloride           |
| TiCl <sub>3</sub>                 | titanium trichloride             |
| Ti(SO <sub>4</sub> ) <sub>2</sub> | titanium(IV) sulfate             |
| TiB <sub>2</sub>                  | titanium diboride                |
| TiS <sub>2</sub>                  | titanium disulfide               |
| Ti(Bu) <sub>4</sub>               | titanium butoxide                |
| TCO                               | transparent conducting oxide     |
| TMSA                              | titania microsphere array        |
| UV                                | ultra-violet                     |
| V <sub>oc</sub>                   | open circuit voltage             |
| XRD                               | X-ray diffraction                |
| XPS                               | X-ray photoelectron spectroscopy |
| 1D                                | one-dimensional                  |
| 3D                                | three-dimensional                |



# Chapter I

## Introduction



### Outline

---

This chapter briefly describes various chemical methods for the synthesis of TiO<sub>2</sub> NCs, its distinctive optoelectronic properties and sundry photoelectrochemical applications followed by a general impression of the work carried out in the thesis.

---

### 1.1 Introduction

So far, diverse methods are used for synthesis of different types of TiO<sub>2</sub> nanostructures. This chapter explains a brief overview of nucleation and growth mechanism of TiO<sub>2</sub> nanostructures. Major solution based chemical techniques, to synthesize titania, have been discussed thoroughly in the introduction. Similar to all other semiconductor materials, the growth of titania depends mainly on four factors i.e. temperature, pressure, time and solvent. So the effect of these parameters on controlling the size and shape of titania has been explained. Next, the structural, optical and electronic properties of titania have been discussed. An understanding of the correlation of structural and optoelectronic properties is required to design single-crystalline, faceted growth of titania. Thus, the structural and optoelectronic properties of titania have also been explained in the introduction. Due to typical electronic configuration of metal oxide semiconductors, it is possible to alter its optoelectronic properties by preferential doping with *s*, *p*, *d*, or *f* block elements or by synthesizing different types of nanocomposite materials. Hence, modification of the optoelectronics and charge-transport properties of titania through doping or synthesis of composite material has also been explained. Finally, various uses of titania in photovoltaic and photocatalytic applications as well as other applications have also been explored thoroughly in this chapter.

### 1.2 Synthesis methods (solution based chemical techniques)

#### 1.2.1 Sol-gel method

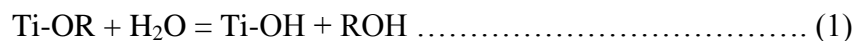
Sol-gel method is quite popular technique used for the synthesis of oxide ceramic materials. In a sol-gel method, first the hydrolysis and subsequently the condensation of the precursor takes place to form colloidal suspension or sol. A 3D network or the gel-phase is

## Chapter 1

---

formed after the complete polymerization of the sol and loss of solvent.<sup>1</sup> In this process, usually metal alkoxides or metal salts are used as precursors. Anisotropic titania nanostructures have been synthesized via sol-gel method by acid catalyzed hydrolysis of titania alkoxide precursors. Through this route, NRs or NWs can be nucleated by specific crystal orientation of the seed layer. If there is low water content, rate of hydrolysis will decrease which facilitate the growth of Ti-O-Ti chains and in the presence of larger amount of excess water, polymeric Ti-O-Ti chains are developed. Adachi *et al.* synthesized short and straight NRs by using aqueous solution of laurylamine hydrochloride, tetraisopropylorthotitanate and acetylacetone as sol. After heat treatment for 8 h at 353 K, this colloidal solution or sol, got converted into a gel suspension and the titania nanoparticles got attached with each other and formed a titania NW network.<sup>2</sup>

The formation of TiO<sub>2</sub> through sol-gel method can be explained by the following reactions.<sup>3</sup>



Where R = alkyl group

The size and shape of the titania nanoparticles is strongly influenced by the relative rate of hydrolysis and polycondensation steps. The growth of highly anisotropic anatase NWs was developed by Buonsanti *et al.* by scheming the hydrolysis of TTIP in oleic acid.<sup>4</sup> The reaction was carried out in inert atmosphere and dried oleic acid was added at 100 °C under continuous stirring. The formation of the highly anisotropic structure is due to the kinetically overdriven growth of titania nanoparticles. Zhang *et al.* also reported similar method to

synthesize titania NRs. Here, they use octadecane as solvent and oleic acid as complexing agent.<sup>5</sup>

Titania NRs have also been synthesized by the sol-gel method using anodic alumina membrane as template. In this method, an AAM was dipped in to the titania sol solution for 10 min and then, it was dried in air for 10 h. After that the NRs were collected by dissolving the AAM template in 10 %  $\text{H}_3\text{PO}_4$  solution.<sup>6</sup>

### 1.2.2 Solvothermal/Hydrothermal method

Solvothermal method is one of the mostly used means to synthesize titania NCs. The synthesis process is carried out in autoclaves at elevated temperature and pressure.<sup>7</sup> If water is used as solvent, the method is called hydrothermal method. For nonaqueous solvents, the temperature can be elevated much higher owing to high boiling points of organic solvents. Solvothermal method is very useful for controlling size, shape and crystallinity of titania NPs. A very narrow size distribution can be achieved through this method. At elevated temperature and pressure, formation of supercritical fluid takes place, which enhances the solubility of various inorganic precursors and allows the precipitation of different oxide compounds and with an increase in reaction time, larger NCs are formed. Fig.1.1 shows the schematic of a solvothermal method.

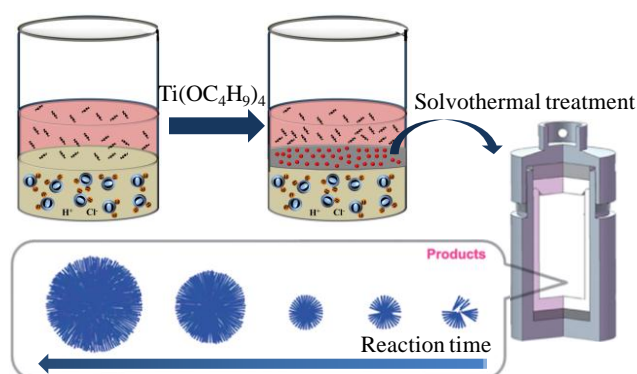


**Fig.1.1:** Schematic of a solvothermal method.

Two main steps are followed for the synthesis of TiO<sub>2</sub>: Hydrolysis of titanium precursors to form hydroxyalkoxides and subsequent condensation reactions to form Ti-O-Ti network.<sup>8</sup> Fig.1.2 shows the schematic of the formation of TiO<sub>2</sub> network.

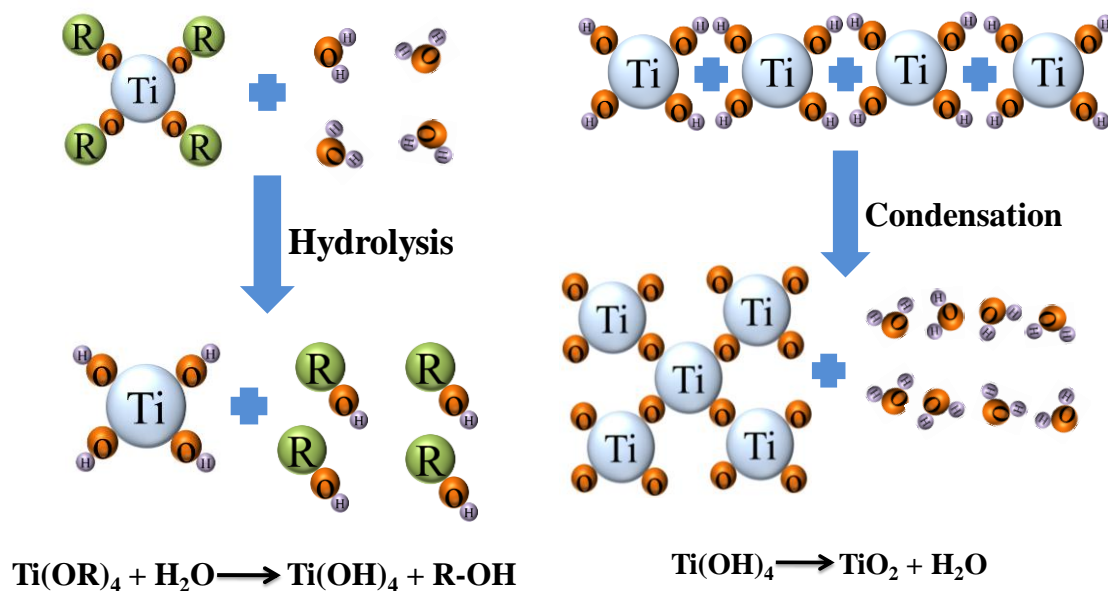


**Fig.1.2:** Schematic of the formation of TiO<sub>2</sub> network.

The size and shape of titania NCs is greatly influenced by the rate of these two steps. Zhang *et al.* have synthesized TiO<sub>2</sub> NRs by mixing TiCl<sub>4</sub> as Ti precursor with dilute acid or inorganic salts and by heating them at different temperatures ranging between 333-423 K for 12 h.<sup>9</sup> Melcarne *et al.* used benzyl alcohol and TTIP to synthesize anatase TiO<sub>2</sub> NRs. They used the acetic acid for morphology control, as the acetic acid is known to bind certain crystal facets and is also known to favor the formation of 1D structures.<sup>10</sup> Monodisperse titania NWs were synthesized by Kim *et al.* by dissolving the TTIP in anhydrous toluene solution and the reaction was carried out at 250 °C for 20 h.<sup>11</sup> Ye *et al.* developed a facile method for the synthesis of rutile titania NRs by using both HCl and ethanol as solvents and by using trivalent TiCl<sub>3</sub> as a precursor.<sup>12</sup>

### 1.2.3 Microwave method

Microwave method is used to prepare various size and shaped titania NPs. Titania is a highly dielectric material and thus, it can be easily synthesized by using high frequency electromagnetic waves. The main advantages of using this method are selective heating and rapid heat transfer.<sup>1</sup> In this process, reactions can be controlled kinetically and due to microwave flash heating, significant reduction of reaction time take place. Ma *et al.* synthesized highly-crystalline, phase-pure rutile titania NRs within 15 min of microwave reaction and observed that the radial assembly of rods occurs instantly.<sup>13</sup> Wu *et al.* synthesized both rutile and anatase titania NTs using certain microwave radiation and aqueous solution of NaOH. The average diameter and length of the as-synthesized NTs were around 12 and 500 nm respectively.<sup>14</sup>

Generally, microwave method is integrated with hydrothermal process using similar precursors and solvents used for only hydrothermal method. Using microwave heating, large rutile titania NRs were synthesized by Lin *et al.* by the direct hydrolysis of  $\text{TiCl}_4$  solution, in dilute HCl.<sup>15</sup>

### 1.2.4 Micelle and Inverse micelle method

Micelle and inverse micelles are frequently used to synthesize titania NCs by controlling the water/surfactant and water/titania precursor ratio.<sup>1</sup> Micelles are formed in aqueous medium and the hydrophilic groups of the surfactant are oriented outwards in the solvent where as reverse micelles are formed in non-aqueous medium, where the hydrophobic tails of the surfactant are directed toward the non-aqueous medium. Zhang *et al.* synthesized shuttle-like titania NCs in the presence of four different acids: HCl,  $\text{HNO}_3$ ,  $\text{H}_2\text{SO}_4$  and  $\text{H}_3\text{PO}_4$  in NP-5(Igepal CO-520)-cyclohexane reverse micelles at room

temperature.<sup>16</sup> Lin *et al.* showed that this method can be used to synthesize highly crystalline titania NPs with minimum aggregation.<sup>17</sup>

### 1.2.5 Electrodeposition

Using AAM, titania NWs are frequently synthesized by the electrodeposition process. Similar to all anodization methods to deposit titanium, the AAM substrate is used as cathode and immersed into 0.2 M  $\text{TiCl}_3$  solution at pH 2 and titanium is deposited into the pores of AAM through pulsed electrodeposition. After that, to remove the template and for the conversion of titanium to titania, the deposited template is heated at 500 °C for 4 h and then dissolved into  $\text{H}_3\text{PO}_4$  solution.<sup>18</sup>

### 1.2.6 Electrospinning

Electrospinning method is used for the large-scale synthesis of titania nanofiber. In this process, using electric field or spinning force, precursors are forced to move through a fine orifice and thus formed fibrous structures.<sup>7</sup> Generally, three components: precursor, binder and stabilizer are required for electrospinning of titania. Any titanium precursor, which is dissolvable in the binder and stabilizer, can be used. The primary function of the binder is to bind the  $\text{TiO}_2$  powders strongly to form titania fibers after spinning where as the role of stabilizer is to control the hydrolysis of the precursor. DMF, a dipolar aprotic solvent is used to synthesize uniform, elongated and fine nanofibers as it is nonvolatile in ambient conditions and enhances the conductivity of the polymer solution. Duan *et al.* synthesized ultrafine (~ 40 nm diameter) and uniform titania nanofibers by using tetrabutyl titanate and DMF.<sup>19</sup> In another approach, Onozuka *et al.* synthesized PVA/titania composite through electrospinning, using acidic acid as the stabilizer and PVA as the binder.<sup>20</sup> Titania nanofibers can also be fabricated by the combination of sol-gel method with electrospinning where the precursors

are processed through sol-gel technique and after that injected through the orifice, forming nanofibres.<sup>7</sup>

### 1.3 Properties of $\text{TiO}_2$

#### 1.3.1 Crystal structure

Naturally occurring  $\text{TiO}_2$  crystals mainly exist in three polymorphs: rutile, anatase and brookite. In addition to that, various metastable polymorphs of  $\text{TiO}_2$  like,  $\text{TiO}_2(\text{B})$ ,  $\text{TiO}_2(\text{H})$  *etc.* have also been synthesized using very particular precursor and meticulous conditions.<sup>21</sup> Among all titania NCs, rutile is the thermodynamically most stable phase. The other phases are metastable and always transformed to rutile at higher temperature. Fig. 1.3 shows the crystallographic unit cell structure of the three polymorphs of  $\text{TiO}_2$ .

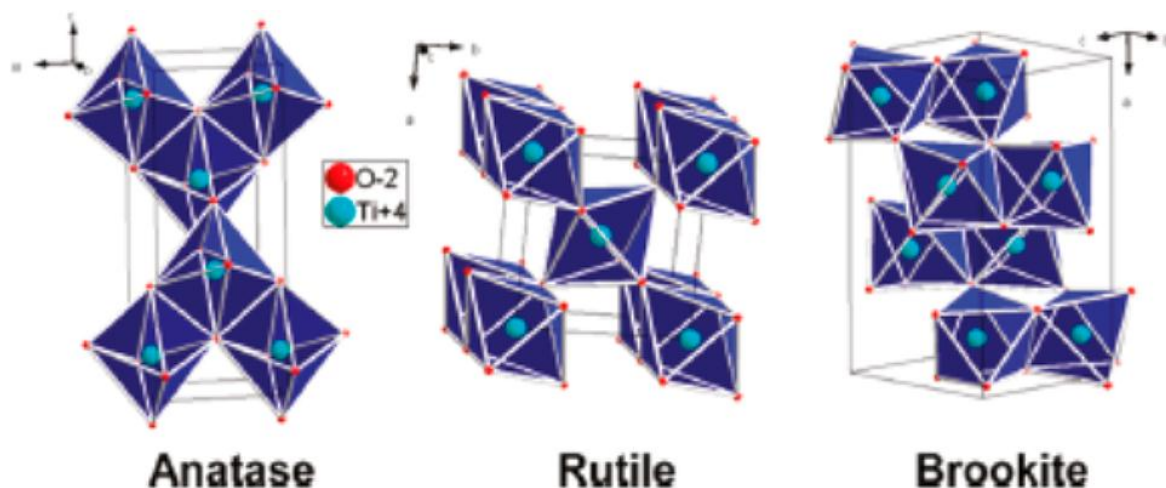


*Fig. 1.3: Schematic of the cell structure of three  $\text{TiO}_2$  polymorphs.*<sup>22</sup>

The fundamental building block of any polymorph of  $\text{TiO}_2$  is  $\text{TiO}_6$  octahedra. The different arrangement and distortion of the octahedra lead to different crystal structure. Each octahedron of rutile crystal, is connected to two edge sharing and six corner sharing octahedra, where the edge-sharing octahedra are arranged along the (001) surface direction. In anatase crystal, each octahedron is connected with four edge-shared octahedra and aligned along the (100) and (010) direction and thus, a double chain perpendicular to the c-axis is formed.<sup>7</sup> Both rutile and anatase  $\text{TiO}_2$  have tetragonal structure but the c-axis (0.951 nm) of anatase is significantly larger compared to a-axis (0.379 nm).<sup>23</sup> In case of rutile, the surface energy of (110) facet is the lowest and thus, it is considered to be the most stable surface while for anatase (101) is found to be the most stable one.<sup>24,25</sup> The shape of rutile and anatase crystals in equilibrium according to Wulff construction are shown in Fig 1.4.

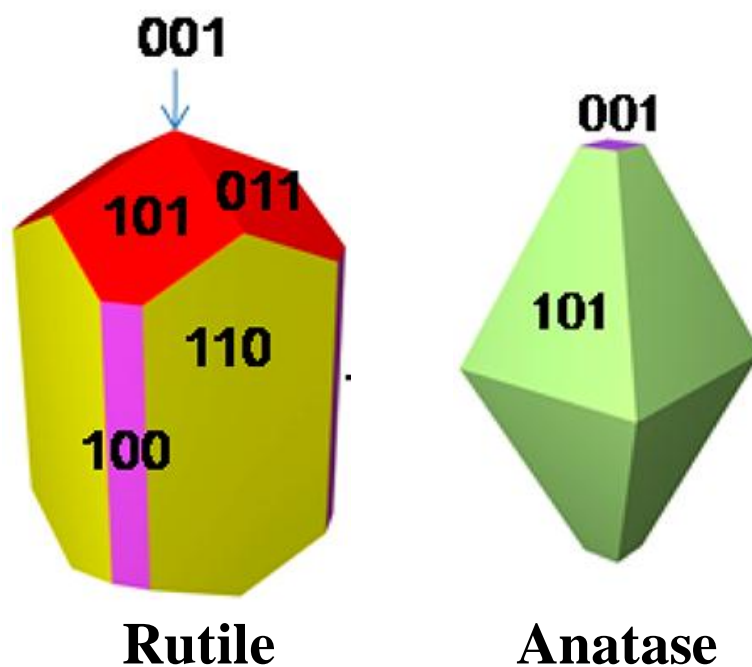


*Fig.1.4: Equilibrium crystal shape of rutile and anatase  $\text{TiO}_2$ .*<sup>24</sup>

Both the rutile and anatase preferred truncated octahedron morphology. In rutile, {110} facets dominate; whereas, in anatase, almost 94 % of the surface is enclosed by {001} facets. Some possible shapes of rutile and anatase crystals evolved from the equilibrium shape are shown in Fig. 1.5.

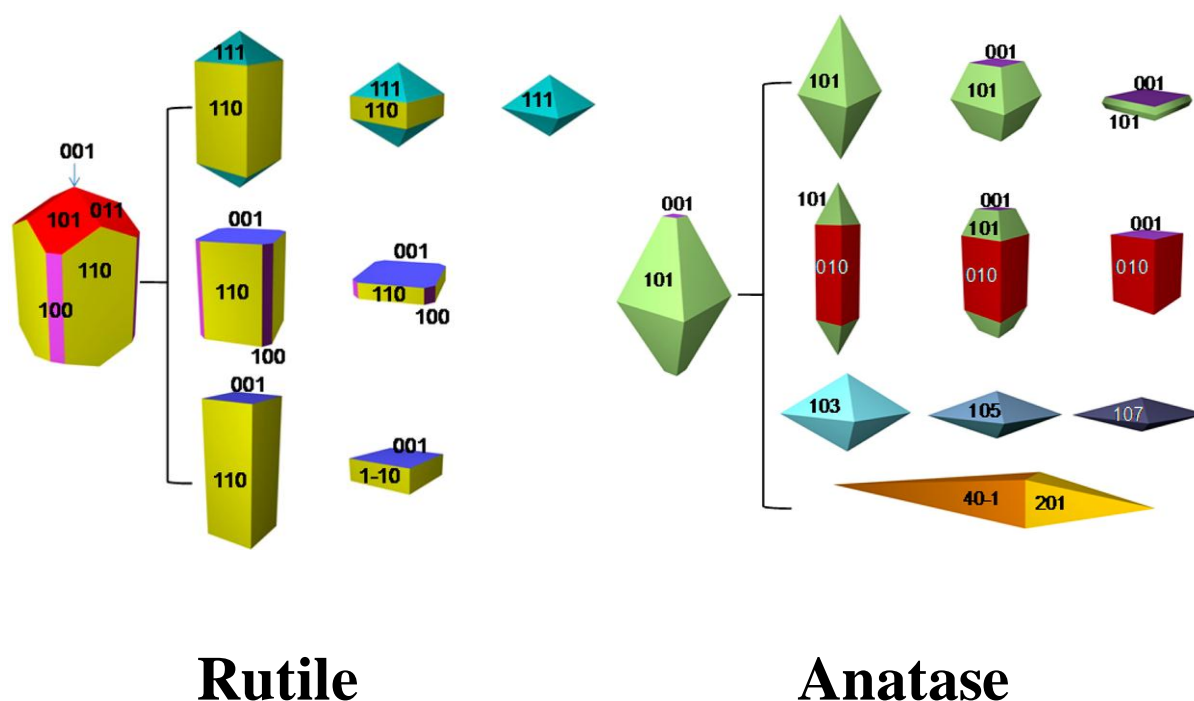


*Fig.1.5: Different shapes of rutile and anatase crystals.*<sup>24</sup>

During crystal growth process, surfaces having high energy are eliminated. The increasing order of specific surface energy for different facets of anatase TiO<sub>2</sub> is {001}>{100}>{101} having surface energy 0.9, 0.53, and 0.4 J/m<sup>2</sup> respectively.<sup>26</sup> Hence, synthesis of anatase TiO<sub>2</sub> with exposed {001} facet is very challenging. The surface energies of rutile TiO<sub>2</sub> for {011}, {110}, and {100} surfaces are 1.85, 1.78, and 2.08 J/m<sup>2</sup> respectively.<sup>27</sup> The unit cell of a rutile titania contains two Ti atoms and four O atoms where

as a anatase unit cell have four Ti and six O atoms. Brookite  $\text{TiO}_2$  is orthorhombic and has a large unit cell having 8  $\text{TiO}_2$  groups.  $\text{TiO}_2$  (B) possesses monoclinic structure with long a-axis (1.216 nm).<sup>28</sup>

Various advanced microscopy techniques are used to determine the exact atomic structures of different phases of titania. Using HVEM, HAADF and STEM, Shibata *et al.* observed the reduced (110) rutile surface.<sup>29</sup> Gong *et al.* acquired STM images of the (101) anatase surface step edge configuration with atomic resolution.<sup>30</sup> De caro *et al.* imaged  $\text{TiO}_2$  lattice using regular HRTEM, having sub-angstrom level resolution.<sup>31</sup>

### 1.3.2 Optical properties

$\text{TiO}_2$  is an indirect semiconductor and so, direct electron transitions between the band centers are forbidden due to crystal symmetry. Braginsky *et al.* showed that due to the momentum nonconservation at the interface, indirect electronic transition takes place, leading to the enhancement of light absorption in titania NCs.<sup>32</sup> Here, the indirect transition is allowed owing to the presence of large electron density states in the valence band and large dipole matrix element. The dielectric functions of the anatase and rutile crystals, parallel and perpendicular to the c-axis for an applied electric field show that anatase is less anisotropic than rutile in the IR to visible spectral range, where the anatase  $\text{TiO}_2$  show anisotropy in UV region.<sup>21</sup> Dimensionality plays an important role in determining the band gap of  $\text{TiO}_2$ . Sakai *et al.* showed both theoretically and experimentally that the band gap of titania nanosheets (1.4 eV) is larger than bulk  $\text{TiO}_2$  (3.2 eV) due to transition from 3D to 2D.<sup>33</sup> As a result of the size quantization effect, the band gap of titania nanosheets is blue-shifted and strong photoluminescence due to the well developed fine structure was also observed.<sup>34</sup> The optical absorption and photoluminescence properties of titania NTs, with inner-diameter between

2.5–5 nm, have been studied thoroughly by Bavykin *et al* and they found that regardless of different diameter, the optical properties of the NTs remain unchanged.<sup>35</sup> Enyashin *et al.* theoretically studied the band structures of anatase nanotubes, nanostrips and nanorolls and found that the density of states of the nanostructures is almost similar to the corresponding bulk phase.<sup>36</sup> The valence band structure of both bulk and nano-TiO<sub>2</sub> is composed of 3*d* Ti-2*p* O states. Besides the study of the bulk electronic structures of various size and shaped titania NCs, the surface states of different titania nanomaterials have also been investigated. Mora *et al.* studied the Fermi level of surface states of titania NPs through non-equilibrium steady state statistics of electrons.<sup>37</sup> From the detailed calculation, it is revealed that the trapped electrons in the surface state did not equilibrate with the Fermi level of the free electrons and thus, they tend to occupy a separate Fermi level, far from equilibrium. The value of the difference between the free electrons and surface Fermi level is around several hundred meV.

### 1.3.3 Electronic properties

From the detailed calculations of density of states, it is found that the band structure of titania is composed of Ti *e<sub>g</sub>*, Ti *t<sub>2g</sub>*, O *p<sub>σ</sub>* and O *p<sub>π</sub>*.<sup>38</sup> The valence band and conduction band of TiO<sub>2</sub> is formed by O 2*p* and Ti 3*d* states respectively. Quantum confinement size effects are observed in TiO<sub>2</sub> around 2 nm size scale as the size of TiO<sub>2</sub> is comparable to the Bohr radius.<sup>39</sup> It is known that when the particle-size of any semiconductor nanoparticle is comparable to the de-Broglie wavelength of the charge carriers or Bohr radius of the first excitation state, quantum confinement of the charge carrier take place which lead to discrete electronic states.<sup>40</sup> The critical diameter also depends on the effective masses of the charge carriers.<sup>41</sup> From the study of the electronic states of TiO<sub>2</sub> by Sortain *et al.* it is known that electronic states of TiO<sub>2</sub> can be divided into three parts. Fig. 1.6 shows the bonding diagram of TiO<sub>2</sub>.

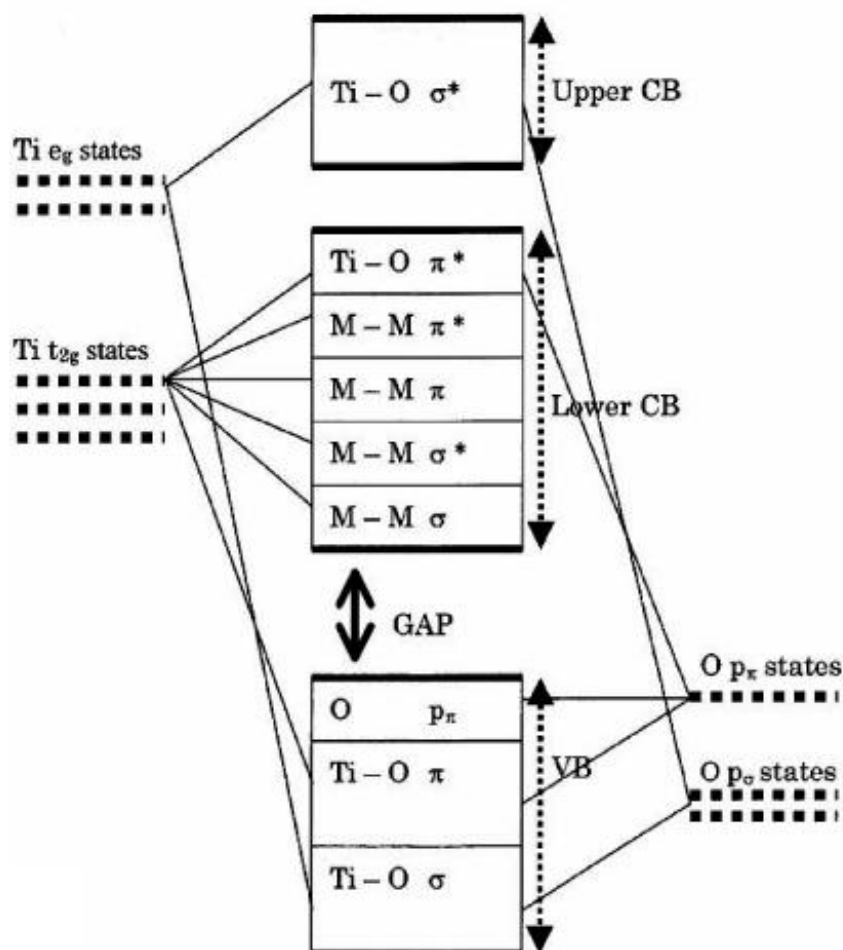


**Fig.1.6:** Bonding diagram of  $\text{TiO}_2$ .<sup>42</sup>

It is cleared from the figure that the higher energy region i.e. upper conduction band is composed of only O  $p$  state whereas the middle region possesses  $\pi$ -bonding of O  $p\pi$  and Ti  $e_g$  state.

Titania crystal possesses high resistivity ( $\sim 10^{15} \Omega\text{cm}$ ).<sup>21,43</sup> The electric conductivity of titania is due to the presence of shallow electron donor level which originates from interstitial Ti ions, reduced crystal surfaces and bulk oxygen vacancy. Interstitial titanium ions having different charges and double charged oxygen vacancies are known to affect the conductivity and ionization energy of rutile titania.<sup>44</sup> Depending on temperature, the

ionization energies of titanium interstitials have been reported around 0.007– 0.08 eV.<sup>45</sup> For anatase crystals, both oxygen vacancies and Ti interstitials are known to equally dominate crystal defects. The activation energy for the carrier generation is around 4 meV.<sup>46</sup>

The transport phenomena of rutile TiO<sub>2</sub> is known to follow through either phonon scattering or hopping of polaron. Due to the presence of large polaron, mobility is known to decrease at higher temperature. Anatase titania shows mobility due to Arrhenius type thermal activation rather than hopping of polaron.<sup>21</sup>

### 1.4 Growth mechanism

It is known that large crystals of TiO<sub>2</sub> are formed through Ostwald ripening process, where the bigger spherical crystals are nucleated from the small particles in TiO<sub>2</sub> nutrient solution, where as for anisotropic growth, oriented attachment mechanism is followed.<sup>7</sup> In this process, TiO<sub>2</sub> NCs are formed by the removal of crystal facets with higher surface energy and thus, the NCs are organized based on their crystallographic orientations. In oriented attachment mechanism, growth of NCs occurred through directional aggregation where as in Ostwald ripening, unidirectional aggregation takes place. Fig. 1.7 shows the schematic of oriented attachment mechanism where NCs form one dimensional structure by coalesce of NCs through (001) facets.<sup>47</sup>

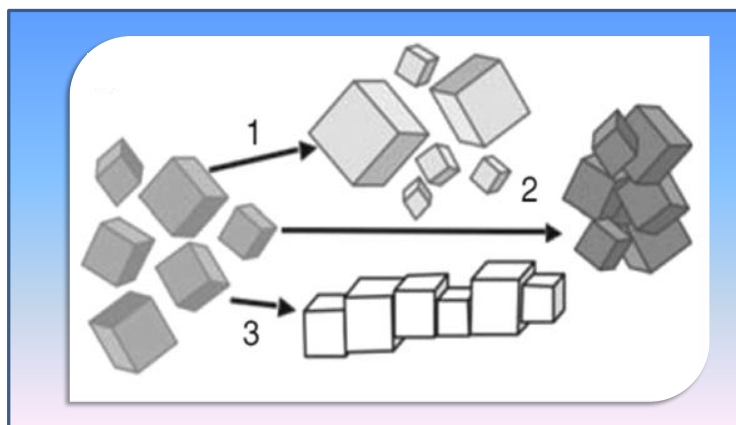


*Fig. 1.7: Schematic of oriented attachment mechanism.*<sup>47</sup>

### 1.4.1 Effect of solvent

Solvent plays an important role for synthesis of  $\text{TiO}_2$  as it controls the state of active Ti species during the growth. However, to achieve a better control over titania-morphology, sometimes, co-solvents are used to control polarity, coordination ability and reactivity of the intermediate phases. In a typical solvothermal synthesis of titania, sodium titanate nanosheet is an important intermediate phase, responsible to control the  $\text{TiO}_2$  crystal growth. It is found that when mixture of alkaline–water ethanol co-solvent is used, long  $\text{TiO}_2$  NWs are synthesized instead of NRs which is the result of high decomposition rate of  $\text{NaTi}_2\text{O}_7$  nanosheets.<sup>7</sup> One-dimensional titania nanostructures are synthesized using the mixture of water and ethylene glycol as solvents where the function of ethylene glycol as a co-solvent is to chelate with  $\text{NaTi}_2\text{O}_7$  nanosheets and to form titania nanotubes by the stacking and rolling of the nanosheets.<sup>48</sup> Das *et al.* also investigated the role of co-solvent and they have grown three different types of 1D-titania nanostructures : NRs, ultralong NWs and NTs by using water, mixture of water-ethanol and mixture of water-ethylene glycol as a solvent

respectively. The growth solution contains TiO<sub>2</sub> powder and caustic soda along with the solvent and the mixture was kept in an autoclave for 16 h at 150 °C.

### 1.4.2 Effect of surfactant

Surfactant also plays a very decisive role to achieve the desired TiO<sub>2</sub> morphology due to its selective affinity for particular surfaces due to change in the binding energy with crystalline facet. The oleic acid is used to synthesize NRs whereas the oleyl amine is used to prepare nanosheets and rhombic-shaped TiO<sub>2</sub> NCs. Wu *et al.* synthesized rhombic-shaped anatase TiO<sub>2</sub> NC by using oleyl amine as a surfactant.<sup>49</sup> Bullet and diamond shaped TiO<sub>2</sub> NPs has been synthesized by Jun *et al.* using lauric acid and phosphin oxide as selective and nonselective surfactant respectively.<sup>50</sup> Adachi *et al.* synthesized network structure of single-crystal-like TiO<sub>2</sub> NWs using the mixture of laurylamine hydrochloride as surfactant and tetraisopropylortho titanate as precursor.<sup>2</sup>

### 1.4.3 Effect of pH

pH control of reaction is also required to get preferred size, shape and phase of TiO<sub>2</sub> NCs. It is observed that for the synthesis of anatase TiO<sub>2</sub> cubic, hexagonal and short NRs with {110}, {101}, and {001} facets alkaline condition is preferred, whereas acidic pH is chosen to prepare tetragonal bipyramidal NCs.<sup>51</sup> The rate of formation of the NCs is also depended on the pH of the medium.

### 1.5 Modification of TiO<sub>2</sub> nanostructures

#### 1.5.1 Synthesis of metal doped nanostructures

Doping of TiO<sub>2</sub> with different metals and nonmetals are performing routinely in order to improve the physicochemical properties of titania. Metals can be doped into TiO<sub>2</sub> through three different methods: wet chemistry, high-temperature treatment and ion implantation.<sup>1</sup> Generally, in wet chemical method hydrolysis of titanium precursor in the presence of other reagents and doping ions take place followed by consecutive heating. Nagvani *et al.* doped anatase TiO<sub>2</sub> with six different transition metal ions through solution combustion method and observed that the concentration of metal ions in the solution has a great effect on the morphology of the titania structure.<sup>52</sup> Wang *et al.* prepared Fe<sup>3+</sup> doped titania NCs and studied the effect of pH on the growth of doped nanostructure. It is seen that, at almost neutral pH homogeneous doping of Fe occur while in acidic pH distribution of Fe ions is nonuniform and formation of mixed phase take place.<sup>53</sup> Li *et al.* synthesized La-doped TiO<sub>2</sub> through sol gel method and observed that La doping not only hinder the phase transformation of TiO<sub>2</sub> and increase the Ti<sup>3+</sup> content on the surface but also reduce the size of the doped NC.<sup>54</sup> In order to be acquainted with the effect of doping of various alkaline metals, Bessekhoud *et al.* prepared Li, Na and K doped titania NCs via sol-gel method and found that Li-doped TiO<sub>2</sub> produced the best crystalline structure.<sup>55</sup> Sn-doped TiO<sub>2</sub> was synthesized by Cao *et al.* through CVD and found that the surface defects increase with increase of dopant concentration.<sup>56</sup> Both doped rutile and anatase TiO<sub>2</sub> NCs have been synthesized by Gracia *et al.* by varying the concentration of dopant metal cations through ion beam induced CVD method.<sup>57</sup>

### 1.5.2 Synthesis of nonmetal doped nanostructures

Nonmetal doped titania nanomaterials have also been studied extensively. In this process, different nonmetals such as B, C, N, P, I, F has been implanted into the anionic site of  $\text{TiO}_2$  by using various process which include wet chemical, electrochemical and physical methods.<sup>21</sup> N-doping can be easily achieved by annealing titania NCs in ammonia atmosphere in a tube furnace. The amount of N-dopindg is dependent on pressure of  $\text{NH}_3$ , time and annealing temperature. Besides that, N-doped  $\text{TiO}_2$  has also been synthesized by hydrolysis of titania precursors in water/amine mixture followed by post treatment of the titania sol ballmilling of  $\text{TiO}_2$  in ammonia water solution.<sup>58</sup> Various other methods such as calcination of the hydrolysis product of  $\text{Ti}(\text{SO}_4)_2$  with ammonia or decomposition of the gas phase  $\text{TiCl}_4$  in the presence of microwave plasma torch has been used for synthesis of N- doped  $\text{TiO}_2$ .<sup>59</sup> The influence of carbon doped  $\text{TiO}_2$  has also been investigated extensively for different titania nanostructures.<sup>60</sup>

Boron doped anatase  $\text{TiO}_2$  microspheres was synthesized by hydrothermal method using  $\text{TiB}_2$  as precursor and HCl solution containing  $\text{Na}_2\text{SO}_4$ .<sup>61</sup> Here, though substitution of oxygen takes place but no change in the intrinsic band gap of  $\text{TiO}_2$  is observed which consisted well with the theoretical results. Depending on various doping methods different valence state of the same nonmetal can be incorporated into either anionic or cationic site of titania. Direct heating of  $\text{TiS}_2$  is used to dope  $\text{S}^{2-}$  while thiourea is used to incorporate  $\text{S}^{4+}$  or  $\text{S}^{6+}$  into  $\text{TiO}_2$ .<sup>62</sup>

Fluorine doped  $\text{TiO}_2$  was synthesized by similar wet chemical method *i.e.* adding titania precursor in ethanol solution, containing water and ammonium fluoride or heating  $\text{TiO}_2$  in the presence of HF.<sup>63</sup>

### 1.5.3 Properties of metal doped TiO<sub>2</sub> nanostructures

Detailed study of the electronic structure of various transition metal doped titania, through ab initio band calculations based on density functional theory reveals that, compared to the pure TiO<sub>2</sub> structure, the electron densities around the dopants increase in the valence band and decrease near the conduction band. Localized characteristics of an electron is prominent within the bandgap.<sup>64</sup> Umebayashi *et al.* calculated the electronic structures of different transition metal oxide doped titania (e.g. V, Fe, Cr, Co, Ni *etc.*) and found that in case of heavier dopants, the localized levels move to the lower energy.<sup>65</sup> When Co is used as the dopant, the localized levels reside very close to the valence band, but, when Ni, which is more heavier than Co is used for doping, delocalization of corresponding dopant levels occurs. Thus, the dopant levels of heavier elements also participate in the valence band along with Ti 3d and O p electrons resulting into a significant change in the photochemical activity of TiO<sub>2</sub>. When Cr is used as a dopant, absorption of visible light occurs as the doping levels reside in the middle of TiO<sub>2</sub> band gap.<sup>66</sup> Owing to the charge transfer between the d orbital electrons of the dopant and valence or conduction band of TiO<sub>2</sub>, a decrease in the band gap energy takes place for doping of V, Mn or Fe in titania lattice. Li *et al.* found that, during substitutional doping of Nd in titania, band gap narrowing takes-place, as the electron states form new lowest unoccupied molecular state, resulting into the reduction of the band gap energy by around 0.55 eV.<sup>67</sup> A general strategy for synthesis of different transition metal doped titania NWs is developed by Liu *et al.* to tune the optoelectrical and catalytical properties of TiO<sub>2</sub>.<sup>68</sup> The overpotential for the oxygen evolution reaction reduced significantly by doping any transition metal ions caused by the strong interaction of the absorbed species on the doped NW surface. It is found that, in comparison to the pristine TiO<sub>2</sub> NWs, 2 % Mn-doped NWs have 28 % lower over potential (0.488 V). However, the

photoelectrochemical conversion ability of the metal oxide doped titania NWs is not studied in detail in comparison to the anion doping.

### 1.5.4 Properties of nonmetal doped TiO<sub>2</sub> nanostructures

Nonmetal dopants are also used extensively to narrow the band gap of TiO<sub>2</sub>. After calculating the band gap of C-doped TiO<sub>2</sub>, Asahi *et al.* found that a deep state is introduced in the gap.<sup>69</sup> Two new levels are explored by Nakano *et al.* in the band structure of C-doped TiO<sub>2</sub>, located at ~1.3 and ~2.34 eV below the conduction band.<sup>70</sup> It is found that the main cause for band gap narrowing in C-doped TiO<sub>2</sub> is due to the presence of this 2.34 eV band which overlapped with the O 2*p* valence band.

Owing to the mixing of 3*p* atomic orbital of sulfur with the valence band, an increase in the band gap width of the VB take place and thus band gap narrowing of S-doped TiO<sub>2</sub> occurs.<sup>71</sup> In case of F doping, F substitutes O in TiO<sub>2</sub> lattice and thus, no overlapping between the 2*p* atomic orbitals of F and the O 2*p* valence state takes place and the 2*p* states of F reside just below the valence state of O 2*p*.<sup>72</sup> Lee *et al.* determined the band structure of N-doped TiO<sub>2</sub> and found that there is a very weak overlap between O 2*p* and N 2*p* states and thus significant band narrowing is not observed.<sup>73</sup>

### 1.5.5 Synthesis of metal-TiO<sub>2</sub> composite

Recently, different types of metal-TiO<sub>2</sub> composites, for *e.g.*, Au-TiO<sub>2</sub> or Ag-TiO<sub>2</sub> have been synthesized by various researchers. Through photodeposition method, Ding *et al.* decorated Ag-clusters homogeneously at the surface of TiO<sub>2</sub> NWs.<sup>74</sup> A significant improvement of the photocatalytic performance is observed for the as-synthesized Ag-TiO<sub>2</sub> NW composite material by the degradation of MB dye. Due to the presence of ultra small

Ag-particles at the surface of titania, there is a dramatic increase of the surface active sites which leads to the augmentation of photocatalytic activity. Pu *et al.* decorated the surface of TiO<sub>2</sub> with three types of morphologies of Au nanoparticles: (1) nanospheres, (2) NRs and (3) mixture of NSs and NRs and they compared the photocatalytic activity.<sup>75</sup> It is found that, when TiO<sub>2</sub> is decorated with Au NRs, there is a dramatic increase in the photocatalytic activity in UV region. On the other hand, when Au-nanospheres are decorated on TiO<sub>2</sub>, slight increase in the catalytic activity occurs in both visible and UV regions. For the mixture of nanospheres and NRs, there is a remarkable increase in the photocatalytic activity in a broad wavelength range from 300 – 800 nm.

### 1.5.6 Synthesis of branched TiO<sub>2</sub> nanostructures

Branched 1D titania nanostructures can be synthesized through the hydrothermal method.<sup>76</sup> To initiate the nucleation on titania surface to achieve a branched morphology, a larger driving force is required, in comparison to the growth of initial 1D-seed. Oh *et al.* synthesized homogeneous branched rutile TiO<sub>2</sub> NRs branch on the surface of TiO<sub>2</sub>, using TTIP as a precursor. In this method, the secondary nucleation became energetically favorable as the surface of initial titania NWs is terminated by the foreign molecules, leading to an increase in the energy and it facilitates a continuous crystal growth.<sup>77</sup> The as-grown length and diameter of the branches are around ~150 and ~20 nm respectively. Wang *et al.* synthesized rutile-anatase heterogeneous branched structure, by utilizing the effect of polar/non-polar interface, using water-dichloromethane system and TiCl<sub>4</sub> precursor.<sup>78</sup>

Following similar hydrothermal reaction and stepwise nucleation, synthesis of various combinations of mixed TiO<sub>2</sub> heterostructures, such as TiO<sub>2</sub> NRs on Si NWs, TiO<sub>2</sub> branches on copper oxide NWs have been developed.<sup>79,80</sup> These mixed heterostructures show unique

## Chapter 1

physicochemical properties. The photo-electrochemical properties of these branched structures got enhanced dramatically due to the presence of low loss charge inner conductors. Sometimes, magnetic or plasmonic particles like Co or Ag can also be decorated on the surface of titania through the colloidal nucleation process to enhance magnetic and optical properties. By the simultaneous hydrolysis of copper acetate and titanium butoxide in the presence of HF solution, Li *et al.* synthesized ultra small Cu<sub>2</sub>O nanoparticles (~ 1.5 to 3 nm) on the anatase titania nanosheet.<sup>81</sup> The photocatalytic performance of these Cu<sub>2</sub>O- TiO<sub>2</sub> heterostructure increased almost three times compared to N-doped anatase TiO<sub>2</sub> nanosheets which is attributed to the presence of p-n interface which promotes charge transfer of the carriers.

## 1.6 Applications of TiO<sub>2</sub> nanostructures

### 1.6.1 Photovoltaic applications

TiO<sub>2</sub> NCs have been widely used in sensitized solar cells as adsorbent of the sensitizer and as a carrier to transport photogenerated electrons. The working principle of a DSSC is shown in Fig. 1.8.

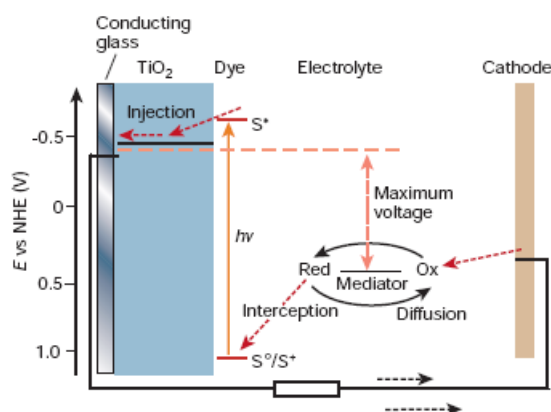


**Fig. 1.8:** Schematic of the operational principle of DSSC.<sup>82</sup>

As the sensitizer absorbs photon, the photoexcitation of the sensitizer takes place and the electrons move to the conduction band of the sensitizer from the valence band and electron-hole pairs or excitons are generated followed by the injection of electron to the conduction band of titania crystals. Here, the time scale of the injection process is comparable to the decay of the excited state of the sensitizer to the ground state. When ruthenium dye is used as sensitizer, the excited-state lifetime of the dye is around 20-60 ns whereas the injection of electrons occurs in femtosecond scale.<sup>83</sup> Koops *et al.* observed that the halftime of the electron injection in a complete DSSC is around 150 ps.<sup>84</sup> After injection of electrons, they are conducted through titania and reach at the anode and subsequently through the external load to the counter electrode. In short, after photon absorption, the excited dye molecules inject electrons to  $\text{TiO}_2$  and the oxidized dye-molecules are reduced by the redox electrolyte. The injected electrons, after travelling through  $\text{TiO}_2$ , are collected at the anode and then move through the external circuit to the cathode and reduce the oxidized electrolyte. Thus, a close circuit is formed which continuously converts solar light to electricity.<sup>85</sup> Fig 1.9. shows the schematic of a DSSC.

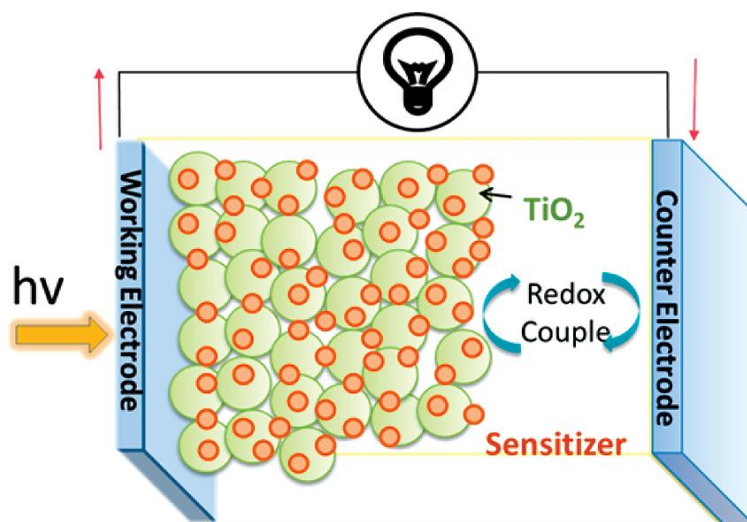


**Fig. 1.9:** Outline of a DSSC constructed with a working electrode consisting of dye-sensitized semiconducting oxide film, a counter electrode made of platinum-coated glass substrate, and electrolyte filled between the working and counter electrodes.<sup>86</sup>

The primary mechanism for generation of photovoltage and photocurrent can be explained in terms of separation, recombination and transport of electronic charges.<sup>87</sup> The photovoltage can be calculated by the difference between the Fermi level of the electron conductor *i.e.*  $\text{TiO}_2$  and the redox level of the electrolyte.<sup>88</sup> The primary cause for the generation of photovoltage is due to the injection of electrons *i.e.* charge from the dye, leads to the change of electron concentration in the conducting NCs *i.e.*  $\text{TiO}_2$ .

The turnover number for a DSSC cell to be durable in the outdoor conditions, for more than 15 years, is around  $10^{18}$ .<sup>89</sup> In a DSSC, the major functions of  $\text{TiO}_2$  are (1) to provide the right medium for the dye-monolayer self-assembly, (2) to accept electrons from the excited state of the dye and (3) to transport the electrons to the collecting layer of the anode *i.e.* on the surface of the transparent conducting oxide electrode.<sup>90</sup> The two foremost ways, to increase the efficiency of DSSC are to extend the light harvesting region of the chromophores towards NIR region and to increase the  $V_{oc}$  by reducing the redox potential of the electrolyte.<sup>91</sup> It is

observed that the current density is increased by 40 % using a dye which absorbs around 980 nm i.e. in the NIR region.<sup>92</sup>

### 1.6.1.1 DSSC based on 1D-TiO<sub>2</sub> nanostructures

Wang *et al.* found that the DSSC fabricated from TiO<sub>2</sub> NWs showed better performance compared to nanospheres due to better electron transport.<sup>93</sup> It is found that under the same illumination condition, the value of electron diffusion coefficient of single-crystalline rutile was almost double compared to the single-crystalline rutile NPs.<sup>94</sup> Using the intensity modulated photovoltage and photocurrent spectroscopy techniques, it is observed by Lee *et al.* that the electron lifetime of titania NRs is ~ 8 times higher in comparison to the titania nanospheres.<sup>95</sup> Grimes *et al.* fabricated ordered titania nanotube arrays having average length around 360 nm directly on FTO substrates through anodic oxidization. The values of photocurrent density and the efficiency of the DSSC, fabricated using this titania nanotube substrate as anode, was ~7.87 mA/cm<sup>2</sup> and ~2.9 % respectively.<sup>96</sup> Adachi *et al.* fabricated DSSC using disordered single-crystalline nanotube as photoanode which exhibited ~ 4.88 % efficiency.<sup>97</sup> Liu *et al.* synthesized 4 μm thick single-crystalline TiO<sub>2</sub> NRs directly on FTO substrates through hydrothermal method and they achieved the photon to electron conversion efficiency around 3 % .<sup>98</sup>

### 1.6.1.2 Comparison of rutile and anatase based TiO<sub>2</sub> solarcells

For solar cell applications anatase phase TiO<sub>2</sub> is preferred due to the presence of its higher conduction band energy. On the other hand, rutile is more stable and possesses better light scattering property. Park *et al.* found that the photocurrent-voltage response of rutile and anatase DSSC having similar thickness is almost identical.<sup>99</sup> The photovoltage response of both the cells are similar where as photocurrent of rutile is 30 % lower than that of anatase

based DSSC. It is also found that owing to the difference of interparticle connectivity due to less particle packing density in rutile, the electron transport property of rutile is slower than anatase.

### 1.6.1.3 DSSC based on doped and composite TiO<sub>2</sub> nanostructures

Lindgren *et al.* found that when N-doped TiO<sub>2</sub> is used as a photoanode, the value of photocurrent increases almost 200 times compared to pure TiO<sub>2</sub> electrode.<sup>100</sup> TiO<sub>2</sub>-carbon nanomaterial composites showed enhanced photon to electron conversion efficiency due to the presence of highly conductive carbon materials and thus, increase the electron mobility and lifetime. Guo *et al.* synthesize TiO<sub>2</sub> NRs coated with carbon fibers and fabricated the photoanode by using this composite material and used it in a DSSC.<sup>101</sup> The efficiency of the as-fabricated solar cell is around 1.28 % and it is seen that the increase in the photocurrent is almost twice compared to only TiO<sub>2</sub> NRs based solar cell. Flexible and integratable fibrous solar cell can be fabricated following this method. Yang *et al.* synthesized different TiO<sub>2</sub>-MWCNT composite core-shell structures by varying the weight of MWCNT in TiO<sub>2</sub> and found a significant increase in solar cell efficiency.<sup>102</sup>

## 1.6.2 Photocatalytic applications

From several years, TiO<sub>2</sub>, the most environmentally benevolent photocatalyst, is widely used for photodegradation of different types of pollutants and to exterminate bacteria owing to its strong oxidizing efficiency upon irradiation.<sup>1</sup> TiO<sub>2</sub> absorbs the photons having energy more than its band gap and excites the electrons to its conduction band and generates charge-carriers. These charge carriers react with the chemicals attached to the surface of

titania and decompose them through producing various free-radicals and intermediates like  $\cdot\text{OH}$ ,  $\text{O}^{2-}$ ,  $\text{H}_2\text{O}_2$  etc. A schematic of photocatalytic activation of  $\text{TiO}_2$  is shown in Fig. 1.10.

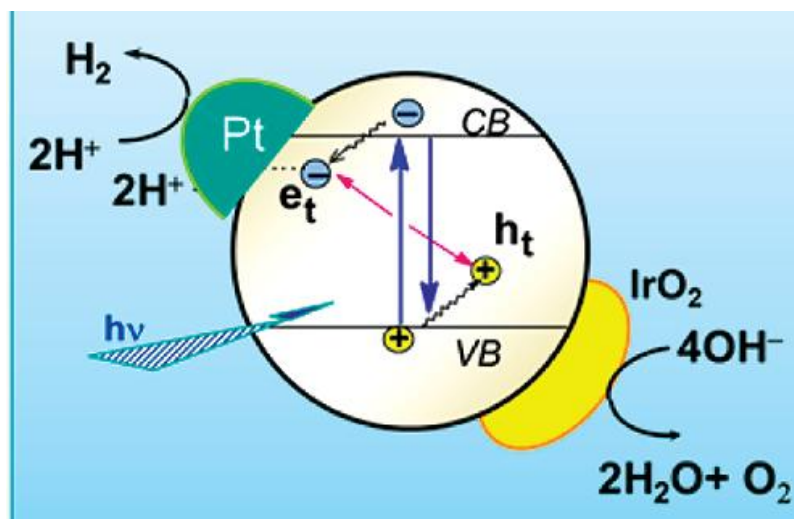


**Fig. 1.10:** Schematic of photocatalytic activation using  $\text{TiO}_2$  nanoparticles.<sup>86</sup>

The photocatalytic activity of titania is primarily controlled by photon absorption properties, rate of redox reactions on the surface by the excitons and the rate of recombination of the excitons. It is found that with decrease in the particle size of  $\text{TiO}_2$ , photocatalytic activity increases which is caused by the increase in the surface area. Anpo *et al.* found that  $\text{TiO}_2$  NPs, having particle size less than 10 nm, showed a dramatic increase in the photocatalytic activity.<sup>103</sup> Chen *et al.* decomposed 2-propanol using three different sized titania NPs having diameter ~30, 15 and 7 nm respectively and they found that the  $\text{TiO}_2$  NPs having diameter 7 nm is the most effective photocatalyst.<sup>104</sup> Photocatalytic activity of metal and non-metal doped  $\text{TiO}_2$  has also been studied thoroughly and they are called as second generation and third generation photocatalysts respectively. Whereas, the pure  $\text{TiO}_2$  nanomaterials are called as first generation photocatalyst.<sup>1</sup>

### 1.6.3 Photocatalytic water splitting

Photocatalytic splitting of water into H<sub>2</sub> and O<sub>2</sub> using TiO<sub>2</sub> under light illumination is proved to be the most clean and sustainable energy source. In 1972, Fujishima *et al.*, for the first time explored the possibility of photocatalytic water splitting.<sup>105</sup> Salvador *et al.* studied the thermodynamic and kinetic effect of water splitting and found that the overvoltage for oxygen evolution is 0.6 eV for TiO<sub>2</sub> electrode loaded with RuO<sub>2</sub>.<sup>106</sup> It has been noted that in simple aqueous system, pure TiO<sub>2</sub> is unable to split water easily. Thus, to generate active site for H<sub>2</sub> evolution, Pt and NiO are frequently loaded.<sup>107</sup> Khan *et al.* covered the TiO<sub>2</sub> nanocrystalline film with Mn<sub>2</sub>O<sub>3</sub> and found significant increase of the stability of the as-covered electrode under light illumination compare to only titania film.<sup>108</sup> The efficiency of water splitting also increased dramatically when, carbonate salt was added to Pt loaded TiO<sub>2</sub> suspension.<sup>109</sup> Mor *et al.* used highly ordered TiO<sub>2</sub> nanotube arrays for water splitting under UV illumination and revealed that the efficiency of splitting of water highly depends on the diameter of the nanotube wall.<sup>110</sup> They achieved 12.25 % photoconversion efficiency under illumination at 320-400 nm. Park *et al.* found that for C-doped TiO<sub>2</sub> nanotubes, the efficiency for decomposition of water increased significantly in both UV and visible region compared to pure TiO<sub>2</sub> NT arrays.<sup>111</sup>

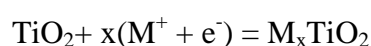
### 1.6.4 Batteries and supercapacitors

Among several polymorphs of titania, TiO<sub>2</sub> (B) is used as an anode in lithium-ion batteries owing to its large intercalation capacity and lower density.<sup>112</sup> It is used in lithium-ion batteries due to its high operating potential (>1 V) for reducing various electrolytes and solvents. The TiO<sub>2</sub>(B) NWs posses petite ionic transport path which leads to better charge/discharge operation compared to its bulk counterpart.<sup>113</sup> Armstrong *et al.* found that

the charging/discharging rate of TiO<sub>2</sub>(B) NWs is faster than TiO<sub>2</sub>(B) film and achieved Li/Ti ratio of 0.91 in TiO<sub>2</sub>(B) NWs having capacity of 305 mA h g<sup>-1</sup>.<sup>114</sup> The cycling stability of NWs based batteries is also very good (~80%). To further improve the charge/discharge rate, metal NWs or graphene are integrated with in the TiO<sub>2</sub> electrodes. Rutile TiO<sub>2</sub> NRs were directly synthesized on graphene sheets for the application in Li-ion batteries and large enhancement of specific capacity was observe at high charging rate.<sup>115</sup> To fabricate rechargeable Li-ion batteries, different types of cathodes such as LiFePO<sub>4</sub> have been integrated with TiO<sub>2</sub>(B) anode.<sup>116</sup> It is known from literature that diffusion coefficient of Li-ions along the c-axis is 9 times higher (10<sup>-6</sup> cm<sup>2</sup>s<sup>-1</sup>) than the diffusion in the ab plane. Thus, for high Li storage, it is required to have larger percentage of {001} facets. Chen *et al.* investigated the Li storage capacity of rose shaped TiO<sub>2</sub> crystals, having higher percentage of {001} facets and found enhanced storage capability at a current rate of 600 mA g<sup>-1</sup>.<sup>117</sup>

### 1.6.5 Electrochromic devices

TiO<sub>2</sub> NCs can be used in electrochromic devices as the oxidation or reduction processes result in the change in color of TiO<sub>2</sub>. Intercalation of monovalent ions into TiO<sub>2</sub> lattice leads to change of color from transparent to bluish. In TiO<sub>2</sub>, the well-accepted model for electrochromism is



The extent of coloration depends on the concentration of metal ions or protons incorporated in TiO<sub>2</sub>.<sup>117</sup> Two types of electrochromism are reported for nanocrystalline TiO<sub>2</sub>. The first is the electrochromism due to the reversible intercalation of Li ions in TiO<sub>2</sub> electrodes in

electrolytes and the other is the electrochromism of TiO<sub>2</sub> electrodes in the presence of different organic molecules such as viologens or anthraquinones having surface anchoring groups.<sup>119,120</sup>

Xia *et al.* coated TiO<sub>2</sub> NWs with different types of conducting polymers and found effective electrochromic property with four-color modes due to high aspect ratio of NWs, which leads to higher intercalation ratio. One of the uses of the electrochromic devices is in the smart windows where the color of the windows can change in order to control the amount of energy entering through the window for effective air-conditioning.<sup>1</sup>

### 1.7 Thesis outline

The present thesis comprises of six chapters, as follows:

In chapter 2, we have studied the formation of desired crystalline facets of highly oriented, single crystalline titania NRs on different substrates and have tried to understand the interplay between the surface chemistry and growth. We have shown that two differently faceted TiO<sub>2</sub> NRs can be synthesized following same synthetic condition by varying only the substrate properties.

In chapter 3, we have synthesized surfactant-free, 3D-self-assembly of titania microsphere arrays (TMSAs) by means of a facile single step solvothermal method and have studied the effect of polar and nonpolar interface on the formation of the self-assembly. The dielectric and optical behavior of these 3D-TMSAs was studied. We have also looked into the scattering related issues like surface/interfacial roughness for efficient photon absorption. The photocatalytic and photon to electron conversion efficiency of the self-assembled titania in DSSCs was also measured.

In chapter 4, we have investigated the effect of lanthanum doping in TiO<sub>2</sub> NR arrays, in order to modify the electrical conductivity and optoelectronic properties of oriented single-crystalline titania NRs, grown on FTO substrates. Homogeneous distribution of lanthanum in titania lattice is confirmed by STEM elemental mapping and line-scan analysis. After doping with lanthanum, there is a negative shift of the flat-band potential of the TiO<sub>2</sub> NRs and there is an improvement in the charge carrier density of the NRs. The energy-conversion efficiency of a DSSC fabricate from 4 mol% La-doped NRs is increased about 21 % compared with the undoped one.

In chapter 5, we summarize the one-step synthesis of oriented, single-crystalline, 1D-rutile TiO<sub>2</sub>-MWCNT composite film on FTO substrates along with 1D rutile TiO<sub>2</sub>-MWCNT powder through a simple low temperature hydrothermal method. Detailed optical studies revealed that the TiO<sub>2</sub>-MWCNT composite efficiently act as quencher and with incorporation of MWCNT, rate of recombination decreases and thus it could be efficiently used in photovoltaics and photocatalysis applications. Electrochemical impedance measurement was done to calculate the band-edge position and electron carrier density of the composite material and it was found that the donor density increased almost 10 times with incorporation of MWCNT in TiO<sub>2</sub> NR network. The composite film was successfully used as a photoanode in a DSSC and we reported an increase in the photon to electron conversion efficiency by 60 % after inclusion of MWCNT.

Chapter 6 presents the brief summary of the results achieved during the thesis work. The future scope for possible further research for designing hybrid material and investigate the growth mechanism in molecular level has been explained concisely.

### 1.8 References

1. Chen, X.; Mao, S. *Chem. Rev.* **2007**, *107*, 72891.
2. Adachi, M.; Murata, Y.; Takao, J.; Jiu, J.; Sakamoto, M.; Wang, F. *J. Am. Chem. Soc.* **2004**, *126*, 14943.
3. Wang, S.C.; Ying, J.Y. *Chem. Mater.* **1999**, *11*, 3113.
4. Buonsanti, R.; Grillo, V.; Carlino, E.; Giannini, C.; Curri, M. L.; Innocenti, C.; Sangregorio, C.; Achterhold, K.; Parak, F. G.; Agostiano, A.; Cozzoli, P. D. *J. Am. Chem. Soc.* **2006**, *128*, 16953.
5. Zhang, Z.; Zhong, X.; Liu, S.; Li, D.; Han, M. *Angew. Chem.* **2005**, *44*, 3466.
6. Miao, L.; Tanemura, S.; Toh, S.; Kaneko, K.; Tanemura, M. *Appl. Surf. Sci.* **2004**, *238*, 175.
7. Wang, X.; Li, Z.; Shi, J.; Yu, Y. *Chem. Rev.* [dx.doi.org/10.1021/cr400633s](https://doi.org/10.1021/cr400633s).
8. Dinh, C.; Nguyen, T.; Kleitz, F.; Do, T. *ACS Nano.* **2009**, *3*, 3737.
9. Zhang, Q.; Gao, L. *Langmuir.* **2003**, *19*, 967.
10. Melcarne, G.; De Marco, L.; Carlino, E.; Martina, F.; Manca, M.; Cingolani, R.; Gigli, G.; Ciccarella, G. *J. Mater. Chem.* **2010**, *20*, 7248.
11. Kim, C. S.; Moon, B. K.; Park, J. H.; Choi, B. C.; Seo, H. J. *J. Cryst. Growth.* **2003**, *257*, 309.
12. Ye, Z. Z.; Huang, J. Y.; Xu, W. Z.; Zhou, J.; Wang, Z. L. *Solid State Commun.* **2007**, *141*, 464.

## Chapter 1

---

13. Ma, G.; Zhao, X.; Zhu, J. *Int. J. Mod. Phys. B.* **2005**, *19*, 2763.
14. Wu, X.; Jiang, Q. Z.; Ma, Z. F.; Fu, M.; Shangguan, W. F. *Solid State Commun.* **2005**, *136*, 513
15. Lin, K.-L.; Mai, F.-D.; Chan, Y.-C.; Chung, J.-C.; Lin, K.-M.; Yu, C.-C.; Liao, M.-Y.; Li, F.-Y. *J. Chin. Chem. Soc.* **2012**, *59*, 603.
16. Zhang, D.; Qi, L.; Ma, J.; Cheng, H. *J. Mater. Chem.* **2002**, *12*, 3677.
17. Lin, J.; Lin, Y.; Liu, P.; Meziani, M. J.; Allard, L. F.; Sun, Y. P. *J. Am. Chem. Soc.* **2002**, *124*, 11514.
18. Lei, Y.; Zhang, L. D.; Fan, J. C. *Chem. Phys. Lett.* **2001**, *338*, 231.
19. Duan, H. G.; Xie, E. Q.; Zhao, J. G.; Jia, C. W. *Mater. Sci. Technol.* **2008**, *24*, 241.
20. Onozuka, K.; Ding, B.; Tsuge, Y.; Naka, T.; Yamazaki, M.; Sugi, S.; Ohno, S.; Yoshikawa, M.; Shiratori, S. *Nanotechnology.* **2006**, *17*, 1026.
21. Banerjee A. N. *Nanotechnology Science and Applications*, **2011**, *4*, 35.
22. Dambournet, D.; Belharouak, I.; Amine, K. *Chem. Mater.* **2010**, *22*, 1173.
23. F Zhou, W. J.; Du, G. J.; Hu, P. G.; Li, G. H.; Wang, D. Z.; Liu, H.; Wang, J. Y.; Boughton, R. I.; Liu, D.; Jiang, H. D. *J. Mater. Chem.* **2011**, *21*, 7937.
24. Liu, G.; Yang, H. G.; Pan, J.; Yang, Y. Q.; Lu, G. Q.; Cheng, H-M. *Chem. Rev.* [dx.doi.org/10.1021/cr400621z](https://doi.org/10.1021/cr400621z).
25. Wang, H.; Shao, W.; Gu, F.; Zhang, L.; Lu, M.; Li, C. *Inorg. Chem.* **2009**, *48*, 9732.
26. Hua, X.; Zhen, Y.; Sun, L. C.; Yang, H. G.; Li, C. *Chem. Mater.* **2011**, *23*, 3486.

## Chapter 1

---

27. Kakiuchi, K.; Hosono, E.; Imai, H.; Kimura, T.; Fujihara, S. *J. Cryst. Growth* **2006**, *293*, 541–545.
28. Marchand, R.; Brohan, L.; Tournoux, M. *Mater. Res. Bull.* **1980**, *15*, 1129.
29. Shibata, N.; Goto, A.; Choi, S.-Y.; Mizoguchi, T.; Findlay, S. D.; Yamamoto, T.; Ikuhara, Y. *Science* **2008**, *322*, 570.
30. Gong, X.-Q.; Selloni, A.; Batzill, M.; Diebold, U. *Nat. Mater.* **2006**, *5*, 665.
31. De Caro, L.; Carlino, E.; Caputo, G.; Cozzoli, P. D.; Giannini, C. *Nat. Nanotechnol.* **2010**, *5*, 360.
32. Braginsky, L.; Shklover, V. *Eur. Phys. J. D* **1999**, *9*, 627.
33. T Sakai, N.; Ebina, Y.; Takada, K.; Sasaki, T. *J. Am. Chem. Soc.* **2004**, *126*, 5851.
34. Sasaki, T.; Watanabe, M. *J. Phys. Chem. B* **1997**, *101*, 10159. Sasaki, T. *Supramol. Sci.* **1998**, *5*, 367.
35. Bavykin, D. V.; Gordeev, S. N.; Moskalenko, A. V.; Lapkin, A. A.; Walsh, F. C. *J. Phys. Chem. B* **2005**, *109*, 8565.
36. Enyashin, A. N.; Seifert, G. *Phys. Status Solidi B* **2005**, *242*, 1361.
37. Mora-Sero, I.; Bisquert, J. *Nano Lett.* **2003**, *3*, 945.
38. Asahi, R.; Taga, Y.; Mannstadt, W.; Freeman, A. J. *Phys. Rev. B* **2000**, *61*, 7459.
39. Li, Y.; White, T. J.; Lim, S. H. *J. Solid State Chem.* **2004**, *177*, 1372.
40. Henglein, A. *Chem. Rev.* **1989**, *89*, 1861.
41. Serpone, N.; Lawless, D.; Khairutdinov, R.; Pelizzetti, E. *J. Phys. Chem.* **1995**, *99*, 16655.

## Chapter 1

---

42. Sorantin, P. I.; Schwarz, K. *Inorg. Chem.* **1992**, *31*, 567.
43. Ardakani, H. K. *Thin Solid Films.* **1994**, *248*, 234.
44. Kofstad P. *J Less CommonMet.* **1967**, *13*, 635.
45. Frederikse HPR. *J Appl Phys.* **1961**, *32*, 2211.
46. Forro L, Chauvet O, Emin D, Zuppiroli L, Berger H, Lévy F. *J Appl Phys.* **1994**, *75*, 633.
47. Penn, R. L.; Banfield, J. F. *Geochim. Cosmochim. Acta* **1999**, *63*, 1549.
48. Das, K.; Panda, S. K.; Chaudhuri, S. *J. Cryst. Growth* **2008**, *310*, 3792.
49. Wu, B.H.; Guo, G.Y.; Zheng, N.F.; Xie, X.Z.; Stucky, G.D. *J.Am. Chem. Soc.* **2003**, *125*, 14539.
50. Jun, W. Y.; Casula, M. F.; Sim, J. H.; Kim, S. Y.; Cheon, J.; Alivastos A. P. *J.Am. Chem. Soc.* **2003**, *125*, 15981.
51. Barnad, A.S.; Curtiss, L. A. *Nano Lett.* **2005**, *5*, 1261-1266.
52. Nagaveni, K.; Hegde, M. S.; Madras, G. *J. Phys. Chem. B* **2004**, *108*, 20204.
53. Wang, Y.; Cheng, H.; Hao, Y.; Ma, J.; Li, W.; Cai, S. *Thin Solid Films* **1999**, *349*, 120.
54. Li, F. B.; Li, X. Z.; Hou, M. F. *Appl. Catal. B* **2004**, *48*, 185.
55. Bessekhoad, Y.; Robert, D.; Weber, J. V.; Chaoui, N. *J. Photochem.Photobiol. A* **2004**, *167*, 49.
56. Cao, Y.; Yang, W.; Zhang, W.; Liu, G.; Yue, P. *New J. Chem.* **2004**, *28*, 218.

## Chapter 1

---

57. Gracia, F.; Holgado, J. P.; Caballero, A.; Gonzalez-Eliphe, A. R. *J. Phys. Chem. B* **2004**, *108*, 17466.
58. Irie, H.; Watanabe, Y.; Hashimoto, K. *J. Phys. Chem. B* **2003**, *107*, 5483.
59. Huang, X. H.; Tang, Y. C.; Hu, C.; Yu, H. Q.; Chen, C. S. *J. Environ.Sci.* **2005**, *17*, 562.
60. Irie, H.; Watanabe, Y.; Hashimoto, K. *Chem. Lett.* **2003**, *32*, 772.
61. Liu, G.; Pan, J.; Yin, L.; Irvine, J. T. S.; Li, F.; Tan, J.; Wormald, P.; Cheng, H.-M. *Adv. Funct. Mater.* **2012**, *22*, 3233.
62. Umebayashi, T.; Yamaki, T.; Sumita, T.; Yamamoto, S.; Miyashita, A.; Tanaka, S.; Asai, K. *JAERI-Rev.* **2003**, 222.
63. Yu, J. C.; Yu, J. G.; Ho, W. K.; Jiang, Z. T.; Zhang, L. Z. *Chem.Mater.* **2002**, *14*, 3808.
64. Sorantin, P. I.; Schwarz, K. *Inorg. Chem.* **1992**, *31*, 567.
65. Umebayashi, T.; Yamaki, T.; Itoh, H.; Asai, K. *J. Phys. Chem.Solids* **2002**, *63*, 1909.
66. Umebayashi, T.; Yamaki, T.; Itoh, H.; Asai, K. *Appl. Phys. Lett.* **2002**, *81*, 454.
67. Li, W.; Wang, Y.; Lin, H.; Shah, S. I.; Huang, C. P.; Doren, D. J.; Rykov, S. A.; Chen, J. G.; Barteau, M. A. *Appl. Phys. Lett.* **2003**, *83*, 4143.
68. Liu, B.; Chen, H. M.; Liu, C.; Andrews, S. C.; Hahn, C.; Yang, P. D. *J. Am. Chem. Soc.* **2013**, *135*, 9995.
69. Asahi, R.; Morikawa, T.; Ohwaki, T.; Aoki, K.; Taga, Y. *Science*, **2001**, *293*, 269.
70. Nakano, Y.; Morikawa, T.; Ohwaki, T.; Taga, Y. *Appl. Phys. Lett.* **2005**, *87*, 052111/1.

## Chapter 1

---

71. Umebayashi, T.; Yamaki, T.; Yamamoto, S.; Miyashita, A.; Tanaka, S.; Sumita, T.; Asai, K. *J. Appl. Phys.* **2003**, *93*, 5156.
72. Yamaki, T.; Umebayashi, T.; Sumita, T.; Yamamoto, S.; Maekawa, M.; Kawasuso, A.; Itoh, H. *Nucl. Instrum. Methods Phys. Res., Sect. B* **2003**, *206*, 254.
73. Lee, J. Y.; Park, J.; Cho, J. H. *Appl. Phys. Lett.* **2005**, *87*, 011904/1.
74. Dinh, C. T.; Nguyen, T. D.; Kleitz, F.; Do, T. O. *ACS Appl. Mater. Interfaces* **2011**, *3*, 2228.
75. Pu, Y. C.; Wang, G.; Chang, K. D.; Ling, Y.; Lin, Y. K.; Fitzmorris, B. C.; Liu, C. M.; Lu, X.; Tong, Y.; Zhang, J. Z.; Hsu, Y. J.; Li, Y. *Nano Lett.* **2013**, *13*, 3817.
76. Shi, J.; Hara, Y.; Sun, C.; Anderson, M. A.; Wang, X. *Nano Lett.* **2011**, *11*, 3413.
77. Oh, J.-K.; Lee, J.-K.; Kim, H.-S.; Han, S.-B.; Park, K.-W. *Chem. Mater.* **2010**, *22*, 1114.
78. Wang, C.; Zhang, X.; Shao, C.; Zhang, Y.; Yang, J.; Sun, P.; Liu, X.; Liu, H.; Liu, Y.; Xie, T.; Wang, D. *J. Colloid Interface Sci.* **2011**, *363*, 157.
79. Shi, J.; Hara, Y.; Sun, C.; Anderson, M. A.; Wang, X. *Nano Lett.* **2011**, *11*, 3413.
80. Feng, Y.; Cho, I. S.; Rao, P. M.; Cai, L.; Zheng, X. *Nano Lett.* **2013**, *13*, 855.
81. Liu, L.; Gu, X.; Sun, C.; Li, H.; Deng, Y.; Gao, F.; Dong, L. *Nanoscale* **2012**, *4*, 6351.
82. Grätzel, M. *Nature* **2001**, *414*, 338.
83. Hagfeldt, A.; Grätzel, M. *Acc. Chem. Res.* **2000**, *33*, 269.
84. Koops, S. E.; O'Regan, B. C.; Barnes, P. R. F.; Durrant, J. R. *J. Am. Chem. Soc.* **2009**, *131*, 4808.

## Chapter 1

---

85. Qu, J.; Lai, C. *J. Nanomaterials* **2013**, *2013*, 11pp.
86. Kamat P.V. *J. Phys. Chem. C* **2012**, *116*, 11849.
87. Cahen, D.; Hodes, G.; Graetzel, M.; Guillemoles, J. F.; Riess, I. *J. Phys. Chem. B* **2000**, *104*, 2053.
88. Pichot, F.; Gregg, B. A. *J. Phys. Chem. B* **2000**, *104*, 6.
89. Hagfeldt, A.; Boschloo, G.; Sun, L.; Kloo, L.; Pettersson, H. *Chem. Rev.*, **2010**, *110*, 6595.
90. Chandiran, A. K.; Sauvage, F.; Casas-Cabanas, M.; Comte, P.; Zakeeruddin, S. M.; Graetzel, M. *J. Phys. Chem. C* **2010**, *114*, 15849.
91. Hardin, E. B.; Snaith, J. H.; Mcghee, D. M. *Nat. Photonics* **2012**, *6*, 162.
92. Snaith, J. H. *Adv. Funct. Mater.* **2010**, *20*, 13.
93. Wang, M.; Bai, J.; Le Formal, F.; Moon, S.-J.; Cevey-Ha, L.; Humphry-Baker, R.; Grätzel, C.; Zakeeruddin, S. M.; Grätzel, M. *J. Phys. Chem. C* **2012**, *116*, 3266.
94. Feng, X.; Shankar, K.; Varghese, O. K.; Paulose, M.; Latempa, T. J.; Grimes, C. A. *Nano Lett.* **2008**, *8*, 3781.
95. Lee, B. H.; Song, M. Y.; Jang, S.-Y.; Jo, S. M.; Kwak, S.-Y.; Kim, D. Y. *J. Phys. Chem. C* **2009**, *113*, 21453.
96. Mor, G. K.; Shankar, K.; Paulose, M.; Varghese, O. K.; Grimes, C.A. *Nano Lett.* **2006**, *6*, 215.
97. Adachi, M.; Murata, Y.; Okada, I.; Yoshikawa, S. *J. Electrochem. Soc.* **2003**, *150*, G488.

## Chapter 1

---

98. Liu, B.; Aydil, E. S. *J. Am. Chem. Soc.* **2009**, *131*, 3985.
99. Park, N.; Lagemaat, J.; Frank, A. *J. Phys. Chem. B* **2000**, *104*, 8989.
100. Lindgren, T.; Mwabora, J. M.; Avendano, E.; Jonsson, J.; Hoel, A.; Granqvist, C. G.; Lindquist, S. E. *J. Phys. Chem. B* **2003**, *107*, 5709.
101. Guo, W.; Xu, C.; Wang, X.; Wang, S.; Pan, C.; Lin, C.; Wang, Z. L. *J. Am. Chem. Soc.* **2012**, *134*, 4437.
102. Yang, L.; Leung, W. W. *Adv. Mater.* **2013**, *25*, 1792.
103. Anpo, M.; Shima, T.; Kodama, S.; Kubokawa, Y. *J. Phys. Chem.* **1987**, *91*, 4305.
104. Chae, S. Y.; Park, M. K.; Lee, S. K.; Kim, T. Y.; Kim, S. K.; Lee, W. I. *Chem. Mater.* **2003**, *15*, 3326.
105. Fujishima, A.; Honda, K. *Nature* **1972**, *37*, 238.
106. Salvador, P. *New J. Chem.* **1988**, *12*, 35.
107. Moon, S. C.; Mametsuka, H.; Tabata, S.; Suzuki, E. *Catal. Today* **2000**, *58*, 125.
108. Khan, S. U. M.; Akikusa, J. *J. Electrochem. Soc.* **1998**, *145*, 89.
109. Sayama, K.; Arakawa, H. *Faraday Trans.* **1997**, *93*, 1647.
110. Mor, G. K.; Shankar, K.; Paulose, M.; Varghese, O. K.; Grimes, C. A. *Nano Lett.* **2005**, *5*, 191.
111. Park, J. H.; Kim, S.; Bard, A. J. *Nano Lett.* **2006**, *6*, 24.
112. Armstrong, A. R.; Armstrong, G.; Canales, J.; Garcia, R.; Bruce, P. G. *Adv. Mater.* **2005**, *17*, 862.

## Chapter 1

---

113. Armstrong, A. R.; Armstrong, G.; Canales, J.; Bruce, P. G. *Angew. Chem.* **2004**, *43*, 2286.

114. Armstrong, A. R.; Armstrong, G.; Canales, J.; Garcia, R.; Bruce, P. G. *Adv. Mater.* **2005**, *17*, 862.

115. Wang, W.; Tian, M.; Abdulagatov, A.; George, S. M.; Lee, Y.C.; Yang, R. *Nano Lett.* **2012**, *12*, 655.

116. Wang, X.; Neff, C.; Graugnard, E.; Ding, Y.; King, J. S.; Pranger, L. A.; Tannenbaum, R.; Wang, Z. L.; Summers, C. J. *Adv. Mater.* **2005**, *17*, 2103.

117. Chen, J. S.; Lou, X. W. *Chem. Sci.* **2011**, *2*, 2219.

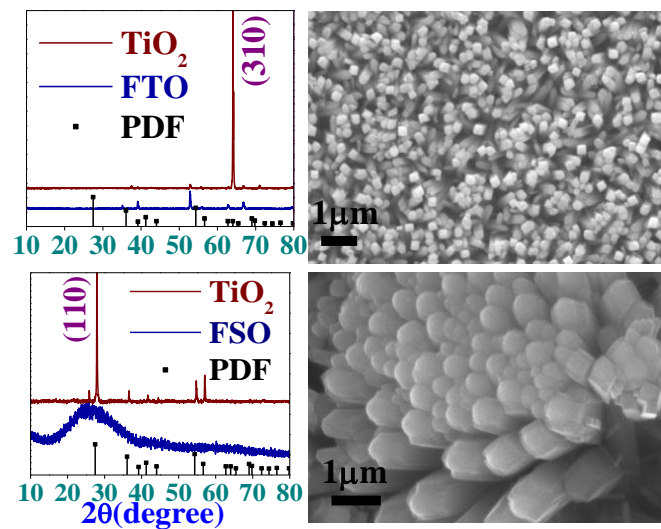
118. Xia, X.; Luo, J.; Zeng, Z.; Guan, C.; Zhang, Y.; Tu, J.; Zhang, H.; Fan, H. J. *Sci. Rep* **2012**, *2*, 981.

119. Hagfeldt, A.; Vlachopoulos, N.; Grätzel, M. *J. Electrochem. Soc.* **1994**, *141*, L82.

120. Garcia-Canadas, J.; Peter, L. M.; Upe Wijayantha, K. G. *Electrochem. Commun.* **2003**, *5*, 199.

## Chapter II

### Understanding the nucleation and growth mechanism of single crystalline TiO<sub>2</sub> nanorods on transparent conducting oxide substrate



### Outline

---

The fabrication of rods or wires of titania in desired crystalline facets is quite exciting due to unique optoelectronic properties. The single crystalline, oriented NRs directly grown on TCO substrates are finding a lot of interest in solar photovoltaics and several other optoelectronic devices attributed to enhanced electron transport and lower exciton recombination rates. However, the growth of desired crystalline facets of highly oriented, single crystalline NRs on different substrates and understanding the interplay between the surface chemistry and growth mechanism still remain non-trivial and challenging task. Here, we have shown that TiO<sub>2</sub> NRs can be grown along two different facets following same synthetic conditions by varying only the material properties of the substrates. To investigate the role of substrate chemistry on the morphology and single crystallinity of TiO<sub>2</sub> NRs, electron microscopy, XPS and contact angle measurements had been done. The results clearly indicate an important link between the surface chemistry and morphology of TiO<sub>2</sub> NRs. It can be assumed that there is a role of OH<sup>-</sup> and water groups which are responsible for the growth of (110) plane which has less surface energy. It is possible to tune the diameter of the titania NRs by further coating the FTO substrates with thin gold layer thereby increasing the hydrophilicity of the substrates. The light to electricity conversion efficiency of 2.5 % could be achieved by using vertically grown titania NRs on FTO as the photoanode in DSSC.

### 2.1 Introduction

Despite the existence of rich literature on various synthesis methods, the customized growth of TiO<sub>2</sub> nanostructures with control over size, shape, crystallinity still remains an open challenge due to complex nature of surface chemistry and difficulties in fine-tuning the nucleation and growth parameters. The growing interest in the need to explore the ways to achieve better control, is further fuelled by the challenges posed from various applications in physics, chemistry, material science, biomedical science, environmental science *etc.* However, it remains non-trivial to fine-tune the synthesis parameter to suit these customized needs without the proper study on growth mechanism and its dependence on the substrate crystallinity. Even, the controlled imperfections in the semiconductor lattice, in the form of lattice defects and cation doping has brought a lot of interest in the people working in the dilute magnetic semiconductors and spintronics areas.<sup>1-3</sup> The use of titania in the photoelectrochemical cell, photoelectrochemical dissociation of organic pollutants, photocatalytic water splitting, electrochromic devices, hydrogen storage, pigment, paint, sunscreen, plant and human pathogen management (due to its antimicrobial activities) *etc.* are now well established.<sup>4-12</sup> It is also demonstrated that most of these properties are heavily dependent on the electronic structure of the material which can be tuned by the size and shape. For instance, it was found that titania NRs showed enhanced photocatalytic activity in compare with Degussa P-25.<sup>13</sup> Moreover, even within a single TiO<sub>2</sub> nanoparticle, these properties often vary significantly for different crystalline facets due to varying amount of surface energy, thereby further posing challenges in front of chemists to develop the synthesis methods for the preferentially growth of desired crystalline facets by using tailored kinetic control of the reactions.

Among different types of nanostructures, 1D rods or wires of titania are extremely important due to their unique optoelectronic properties which arise due to their anisotropic shape. However, reaching the desired level of perfection (especially the growth of desired facet) remains still quite challenging and non-trivial. At present, several chemical methods are employed for preparing titania NRs/NWs. Among them, some well-known procedures include the direct oxidation of Ti substrate, electrochemical anodization of titanium, template assistant approaches, metal-organic chemical vapor deposition, hydrothermal method, sol-gel method *etc.*<sup>14-19</sup> Nevertheless, several of these methods are still filled with issues to be addressed in coming years. The crystalline, oriented NRs/NWs are finding a lot of interest in the area of solar photovoltaics. It is found that the polycrystalline titania NT arrays exhibit lower recombination of electrons and holes and therefore, it is used in the DSSCs.<sup>20-22</sup> However, if these 1D titania nanostructures are single crystalline, then they have added advantage of faster electron transport due to the absence of grain-boundaries and reduced electron trap sites.<sup>23-25</sup> Growth of the oriented rods on the TCO substrates show faster charge transport rates and electron diffusion at electrolyte semiconductor interface.<sup>26, 27</sup>

Among various wet-chemical methods explored in the literature for the growth of highly oriented, crystalline NRs, the hydrothermal or solvothermal methods are most useful as they require relatively lower synthesis temperature which does not harm the FTO coating on the glass substrates. The direct growth of single crystalline TiO<sub>2</sub> NRs on FTO coated glass by hydrothermal and solvothermal method was first reported a few years ago<sup>28, 29</sup> followed by a general method to synthesize TiO<sub>2</sub> rods on various substrates.<sup>30,31</sup> Despite the huge importance of this method in optoelectronic devices such as solar cells and in photocatalysis, the understanding on the growth mechanism of the NRs and role of substrates remain poorly explored.

We have studied the nucleation and growth mechanism of titania NRs on various substrates and the effect of reaction time on the enlargement of the NRs. To understand the role of substrate, we have synthesized TiO<sub>2</sub> NRs on two different substrates (1) FTO coated glass in crystalline form and (2) FTO coated glass in amorphous form which was termed as fluorine doped silicon oxide or FSO owing to the presence of very little amount of tin oxide. The results showed strong influence of the crystallinity of FTO layer on the crystallinity of the as-grown TiO<sub>2</sub> NRs. TiO<sub>2</sub> NRs can be fabricated in two different orientations by changing the substrates. Moreover, we also demonstrated the tunability of rod diameter by playing with the surface wettability of substrate by gold coating. Below, a detailed characterization of TiO<sub>2</sub> NRs using XRD, XPS, HRTEM, SEM, UV–vis absorption, and photoluminescence techniques has been done. The possible mechanism behind the interesting growth of particular lattice planes has been discussed.

## 2.2 Materials and method

### 2. 2.1 Synthesis of TiO<sub>2</sub> NRs on different substrates

To study the effect of substrates on the growth of TiO<sub>2</sub> NRs, the NRs were synthesized on polycrystalline FTO (sheet resistance = 8 ohm/square; Solaronix) and amorphous FSO, sheet resistance = 156 ohm/square) glass substrates respectively through solvothermal chemistry where Ti(OBu)<sub>4</sub> (purity ≥ 97%, Aldrich) was used as precursor. In a typical synthesis process, first the substrate was ultrasonically cleaned in a mixed solution of DI water, acetone and isopropanol and then dried in N<sub>2</sub> flow. Thirty mL H<sub>2</sub>O and thirty mL concentrated HCl (35 %) were stirred for 10 min in a 100 mL Teflon vessel followed by the drop-wise addition of 1 mL Ti(OBu)<sub>4</sub> and stirring for another 10 min at RT. The substrates were placed horizontally within the Teflon vessel and the vessel was loaded inside a 100 mL autoclave for the hydrothermal reaction at 150 °C for 20 h in a furnace. After synthesis, the

autoclave was cooled to room temperature and the substrates were washed vigorously with deionised water and then dried in air. Fig 2.1 showed the schematic of the growth process.

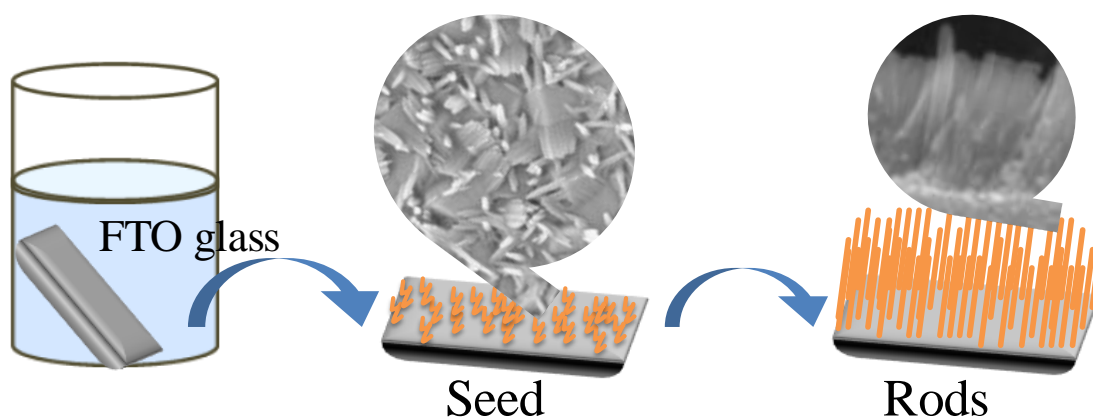


*Fig. 2.1: Schematic of the synthesis of oriented TiO<sub>2</sub> NRs on substrate.*

### 2.2.2 Fabrication of DSSC

To fabricate a solar cell at first the as-synthesized TiO<sub>2</sub> NRs on FTO substrate were annealed in air at 400 °C for 30 min. Then the as-synthesized TiO<sub>2</sub> NRs on FTO substrate were cooled to 80 °C and were immersed in a 0.5 mM ethanolic solution of N-719 dye (as received from Solaronix) for 24 h to facilitate sufficient adsorption of the dye which will act as the sensitizer in the presence of light. After completing the adsorption of the dye, the substrate was washed very carefully with ethanol and was dried for 1 h. After that a platinum coated FTO substrate, which will be used as the counter electrode, was placed above the dye-adsorbed FTO substrate and an electrolyte containing 0.6 M 1-hexyl-2-3-dimethylimidazolium iodide, 0.1 M LiI, 0.05 M I<sub>2</sub> and 0.5 M 4-tert-butylpyridine in methoxyacetonitrile was injected into the space between the anode and the cathode to complete the assemble of the DSSC.

### 2.2.3 Characterization techniques

In order to confirm the crystalline phase of TiO<sub>2</sub> NRs, powder XRD study was performed using a PANalytical X'PERT PRO instrument and the iron-filtered Cu-K<sub>α</sub> radiation ( $\lambda = 1.5406 \text{ \AA}$ ) in the  $2\theta$  range of  $10 - 80^\circ$  with a step size of  $0.02^\circ$ . XPS data was collected by using a VG Microtech, model ESCA 3000 equipped with ion gun (EX-05) for cleaning the surface. The binding energy resolution was 0.1 eV. To investigate the role of substrate chemistry on the morphology and single crystallinity of TiO<sub>2</sub> NRs, the as-synthesized NRs were characterized by environmental scanning electron microscopy (FEI Quanta 200 environmental scanning microscope). We also used FEI Tecnai F30 HRTEM equipped with a super-twin lens (s-twin) operated at 300 keV accelerating voltage with Schottky field emitter source with maximum beam current ( $> 100 \text{ nA}$ ) and small energy spread (0.8 eV or less). The point-to-point resolution of the microscope is 0.20 nm with a spherical aberration of 1.2 mm and chromatic aberration of 1.4 mm with 70  $\mu\text{m}$  objective aperture size. Optical properties of the as-synthesized TiO<sub>2</sub> NRs were investigated by a UV-visible spectrophotometer. UV-vis-NIR spectroscopy measurements were performed on a Jasco UV-vis-NIR (Model V570) dual beam spectrometer operated at a resolution of 2 nm. PL and PLE spectra were acquired using a Jobin Yvon Fluorolog-3 spectrofluorometer, equipped with a 400 W Xe lamp as an excitation source and a Hamamatsu R928 photomultiplier (PMT) tube as a detector. STM measurements were carried out at RT and ambient pressure using Veeco Multimode scanning probe microscope with NanoScope IV controller. STM tips were prepared from Pt-Ir (8:2) wire by the mechanical cutting method and used without any further treatment. STM images were taken with a bias voltage of 40 mV and 30 nA current and feedback was set to log. The system bias voltage was applied to the sample and tip was kept at ground. The scan rate was 1 Hz. Current-voltage

characteristics were calculated by irradiating the cell with  $100 \text{ mW/cm}^2$  (450 W xenon lamp, Oriel instrument), 1 sun AM 1.5 G filter was used to simulate the solar spectrum. The active area of the cell was  $0.5 \text{ cm}^2$ . The photocurrent was measured by using a Keithley 2400 source.

### 2.3 Results and Discussion

#### 2.3.1 XRD analysis

In Fig. 2.2(A), the XRD pattern of  $\text{TiO}_2$  NRs grown directly on FTO-coated glass substrate, FTO substrate without  $\text{TiO}_2$  NRs and PDF file # 21-1276 of rutile  $\text{TiO}_2$  have been compared. The XRD study confirmed that  $\text{TiO}_2$  NRs grown on different substrates are in rutile phase. It is cleared from the diffraction peaks that the NRs are highly oriented with respect to the substrate along the (310) plane. In Fig. 2.2(B), the XRD pattern of  $\text{TiO}_2$  NRs grown on FSO glass substrate, FSO glass substrate without  $\text{TiO}_2$  NRs and PDF file no-21-1276 have been compared to explore the role of substrate. It is cleared from the XRD data that, when FSO substrate was used for the growth of  $\text{TiO}_2$  NRs then the intensity of (110) diffraction peak was enhanced.

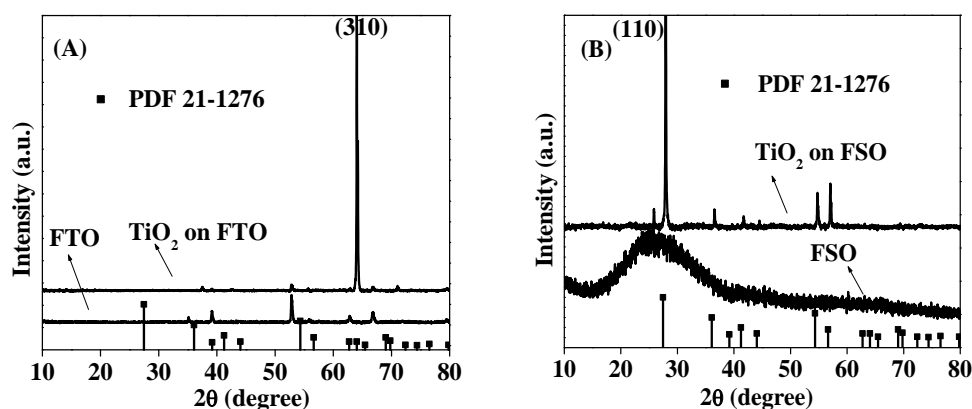


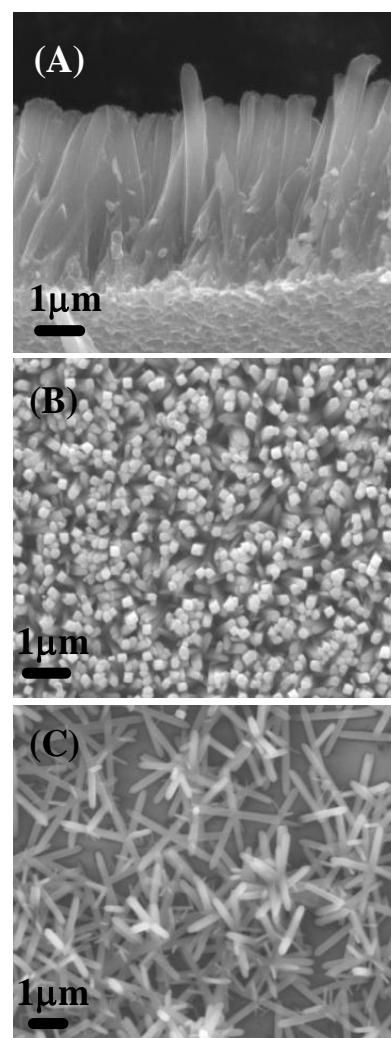
*Fig. 2.2: XRD pattern of rutile  $\text{TiO}_2$  NRs grown on (A) FTO (B) FSO coated glass substrate.*

### 2.3.2 Determination of shape and size

#### 2.3.2.1 SEM analysis

Fig.2.1.3 represents the SEM images of the NRs grown on FTO and FSO substrates. From the images it is confirmed that the NRs are densely packed and perfectly oriented with respect to FTO. But when FSO is used as substrates, then the NRs are not densely packed and also the orientation of the rods is not vertical with respect to the substrate. It is clear from the figure that the top facets of the rods are square shaped which also supports the expected growth habit of tetragonal crystal. The length and diameter of the rods are around 4.5  $\mu\text{m}$  and 200 nm respectively. Further, from EDX analysis the chemical stoichiometry of the  $\text{TiO}_2$  NRs was calculated and it was found that the atomic ratio of Ti to O is nearly about 1:2.

**Fig. 2.3:** SEM images of  $\text{TiO}_2$  NRs (A) grown on FTO coated glass substrate (cross-sectional view) (B) (top view), (C) FSO substrate.



## 2.3.2.2 TEM analysis

Fig. 2.4 showed the TEM and HRTEM images of individual  $\text{TiO}_2$  NRs grown on FTO and FSO substrates. In Figs. 2.4(B) and 4(E), lattice fringes, with interplanar spacing  $d_{101} = 0.24$  nm for FTO and  $d_{110} = 0.32$  nm for FSO corresponding to the rutile phase of  $\text{TiO}_2$ , can be identified clearly. The FFT pattern also confirms the single crystallinity of the NRs. Sharp SAED pattern for the  $\text{TiO}_2$  NRs grown on FTO substrate (Fig. 2.4(c)) was visualized nicely along  $[001]$  zone-axis which was the inveterate evidence of the single crystallinity of the NRs.

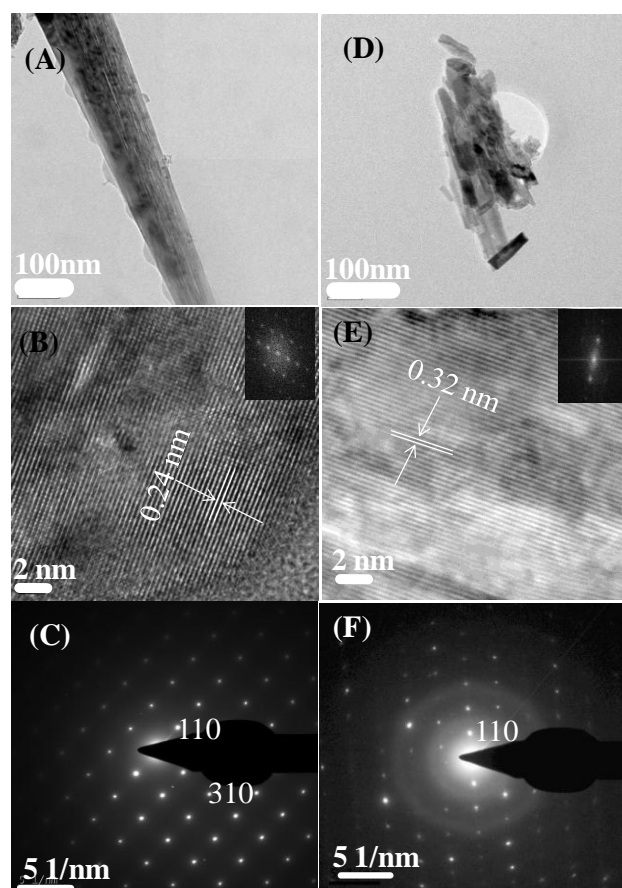


**Fig. 2.4:** (A) TEM image (B) HRTEM image with inset showing FFT pattern (C) selected area electron diffraction pattern of single  $\text{TiO}_2$  NR grown on FTO glass substrate. (D) TEM image (E) HRTEM image with inset showing FFT pattern (F) selected area electron diffraction pattern of single  $\text{TiO}_2$  NR grown on FSO substrate.

### 2.3.3 Growth mechanism

Earlier reports specify that when the NRs were synthesized on plain glass or tin-doped indium oxide (ITO) coated glass substrates, the rods were polycrystalline in nature.<sup>30</sup> Moreover, in those cases, the as-grown TiO<sub>2</sub> rods were randomly oriented with respect to the substrate.<sup>30</sup> It is known that during the aggregation of TiO<sub>2</sub> nanoparticles, the “oriented attachment growth mechanism” is followed.<sup>32</sup> In the case of oriented attachment, the adjacent particles are self-attached instantly to share a common crystallographic orientation. After that these particles are connected at a planar interface. This mechanism is also applicable for the particles which nucleate on a substrate and coalesce during growth.<sup>32</sup> As usual, in order to reduce the surface energy by eliminating high energy facets, attachment always take place at the high energy surfaces. During the growth of TiO<sub>2</sub> NRs on FTO substrate, SnO<sub>2</sub> can effectively acts as a nucleation layer.<sup>31</sup> As both the rutile titania and stannic oxide have tetragonal structure where the surface energy of (310) plane is much higher than (110) plane, growth of titania crystal occurs instantly along the (310) direction to minimize the surface energy. In the case of FSO, it was found from the EDX analysis that the atomic percentage of Sn is only 0.45. Moreover, the XRD pattern showed that FSO substrate is amorphous in nature. Therefore, it can be assumed that in contrast to the FTO substrate, similar nucleation sites are not present on the FSO coated glass substrate and so the probability of the growth of (310) plane is reduced. In acidic solution, the nucleation and growth of rutile TiO<sub>2</sub> is thermodynamically and kinetically controlled by the enhanced corner shared bonding of [TiO(OH<sub>2</sub>)<sub>5</sub>]<sup>2+</sup> nuclei. The surface energy of the (110) plane of the rutile TiO<sub>2</sub> is the lowest compared to other planes. Moreover, the presence of large number of five-fold co-ordinated Ti<sup>4+</sup> atoms, two-fold co-ordinated O<sup>2-</sup> atoms and oxygen vacancies favour the selective adsorption of anions on (110) surface and thus a ‘screening layer’ is formed on surface which restrict further oxolation of [TiO(OH<sub>2</sub>)<sub>5</sub>]<sup>2+</sup> complex on (110) surface. On the contrary,

the two cusps of rod consist of other higher energy surface can adsorb more  $[\text{TiO}(\text{OH}_2)_5]^{2+}$  complex to decrease the surface energy. Thus the NRs grow anisotropically along the (110) surface on FSO coated substrates.

### 2.3.3.1 XPS analysis

To further explain the growth pattern, the XPS spectra of oxygen for the growth of  $\text{TiO}_2$  NRs on FTO and FSO glass substrates have been shown in Fig.2.5. Shirley algorithm was used for background correction and chemically distinct species were resolved using a nonlinear least-square fitting procedure. The core level binding energy was aligned with the carbon binding energy of 285 eV. The fitting of O 1s peak in Fig. 2.5(A) indicated three components which are characteristic of  $\text{TiO}_2$ , Ti–OH and Ti–OH<sub>2</sub>, successively with increasing binding energies at ~530, ~532, ~533 eV respectively. As XPS is a surface sensitive technique so any change in the surface such as reduced coordination number or surface disorder will change the spectra. It has been suggested that the surface hydroxide ions contribute to the 1D growth of single crystalline  $\text{TiO}_2$  NRs on FTO substrate. In Fig. 2.5 (B), the maximum intense peak of O 1s spectra for  $\text{TiO}_2$  NRs grown on FSO substrate shifts towards higher binding energy (from ~530 eV to ~532 eV), which confirms that on the surface of  $\text{TiO}_2$  NRs, most of the oxygen contribution originates from OH and OH<sub>2</sub> groups. The results confirm that other plane of  $\text{TiO}_2$  can adsorb larger amount of  $[\text{TiO}(\text{OH}_2)_5]^{2+}$  than (110) plane thereby blocking the growth of planes other than (110) and thus the NRs grow anisotropically along the (110) surface. In Fig.2.5 (A), the maximum intense peak in O 1s core level spectra for  $\text{TiO}_2$  NRs growth on FTO comes around 530 eV which corresponds to the oxygen which comes from  $\text{TiO}_2$  species and the peak at higher binding side corresponds to the hydroxyl groups adsorbed at the surface of  $\text{TiO}_2$  NRs formed at the surface due to broken and dangling bonds from the oxygen that have to be terminated. In addition, a small amount of bound surface water is often detected, even in ultrahigh vacuum conditions.

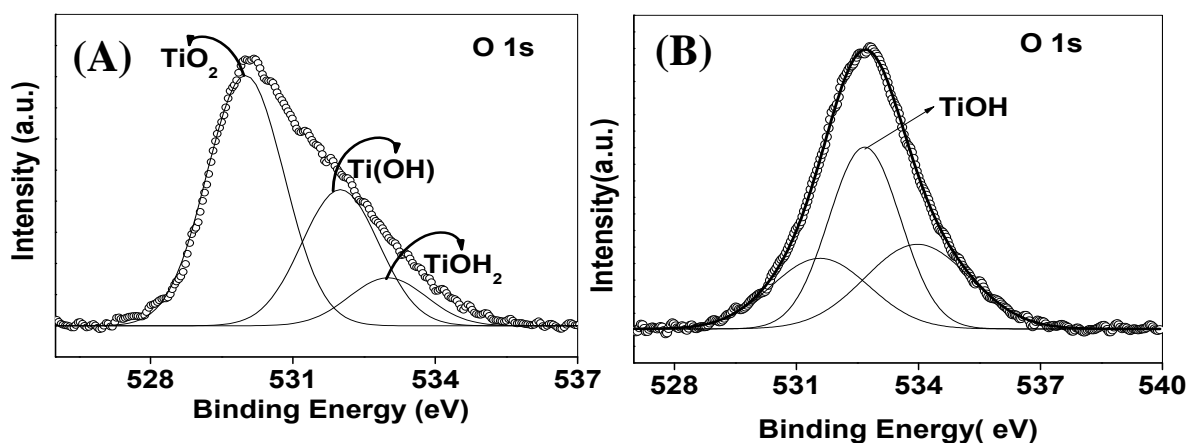


*Fig. 2.5: XPS spectra of O 1s core level for TiO<sub>2</sub> NRs grown on (A) FTO (B) FSO glass substrates.*

The surface energy of (310) plane is much higher than (110) plane. According to Donnay-Harker rule, the surface free energy of the {001} faces is about 1.4 times larger than {110} faces. Surfaces with higher energy usually diminish very fast during crystal growth.<sup>34</sup> <sup>35</sup> In the case of FTO, it was found that SnO<sub>2</sub> layer of the FTO substrates efficiently provides nucleation sites during the growth of TiO<sub>2</sub> NRs.<sup>31</sup> The thermodynamically stable crystal structure of Sn(IV) dioxide or stannic oxide is rutile. In the rutile phase of stannic oxide, the surface energy of (310) plane is much higher than (110) plane which results growth of (310) plane on the FTO substrate.

From the comparative study of O 1s core level XPS spectra, it can be assumed that there is a role of OH<sup>-</sup> and water groups which are responsible for the growth of less energetic plane (110). Earlier, people have reported the growth of TiO<sub>2</sub> NRs along (002) plane on the FTO substrate through solvothermal method.<sup>28-29</sup> The anisotropic growth of the NRs along (002) plane can be explained by the shape controlled chemistry where Cl<sup>-</sup> ions are selectively adsorbed onto the (110) crystal plane of rutile TiO<sub>2</sub>, suppressing further growth of that plane

resulting the formation of NRs.<sup>28</sup> The very small lattice mismatch of rutile  $\text{TiO}_2$  and FTO substrate is the driving force for the epitaxial growth of  $\text{TiO}_2$  NRs on FTO substrate.<sup>29</sup>

### 2.3.4 Optical properties

#### 2.3.4.1 UV-vis analysis

Fig. 2.6 showed the UV-visible absorption measurements of the  $\text{TiO}_2$  NRs grown on FTO and FSO substrate. It is cleared from the absorption spectra that the  $\text{TiO}_2$  NRs are transparent in the visible region which is the characteristic of  $\text{TiO}_2$ . The absorption edge is at 420 nm for both type of  $\text{TiO}_2$  NRs grown on FTO and FSO substrate. Assuming that the rutile  $\text{TiO}_2$  NRs possess a direct transition the band edge energy of the as synthesized NRs are calculated by plotting  $(\alpha h\nu)^2$  against  $h\nu$  (where  $\alpha$  is absorption coefficient and  $h\nu$  is photon energy).<sup>36</sup> From the intercepts (shown in the insets of Fig. 2.6) the band gap energy of the  $\text{TiO}_2$  NRs grown on FTO and FSO is found to be 2.9 and 3 eV respectively.

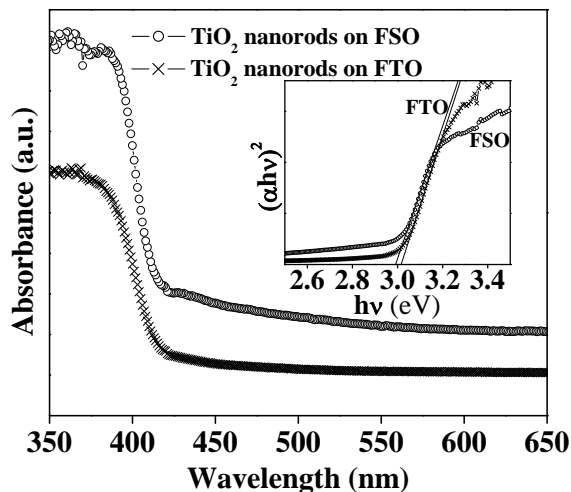


*Fig. 2.6: UV-visible absorption spectra of  $\text{TiO}_2$  NRs grown on FTO and FSO glass substrates. The inset shows the dependence of the absorption coefficient as a function of  $h\nu$  for the  $\text{TiO}_2$  NRs.*

### 2.3.4.2 PL analysis

Fig. 2.7 compared the photoluminescence of the  $\text{TiO}_2$  NRs grown on FTO and FSO. The spectra showed an emission peak at 445 nm at excitation wavelength of 410 nm. Corresponding PLE spectra exhibit absorption at  $\sim 410$  nm. It is reported that the luminescence behavior, of the single crystal rutile NRs, is due to the emission of excitons.<sup>37</sup> Moreover, the emission of free excitons also take place if the crystal is sufficiently pure or in a way if it is a defect free crystal. The very weak green band emission can be ignored which implies a very low concentration of oxygen defect.

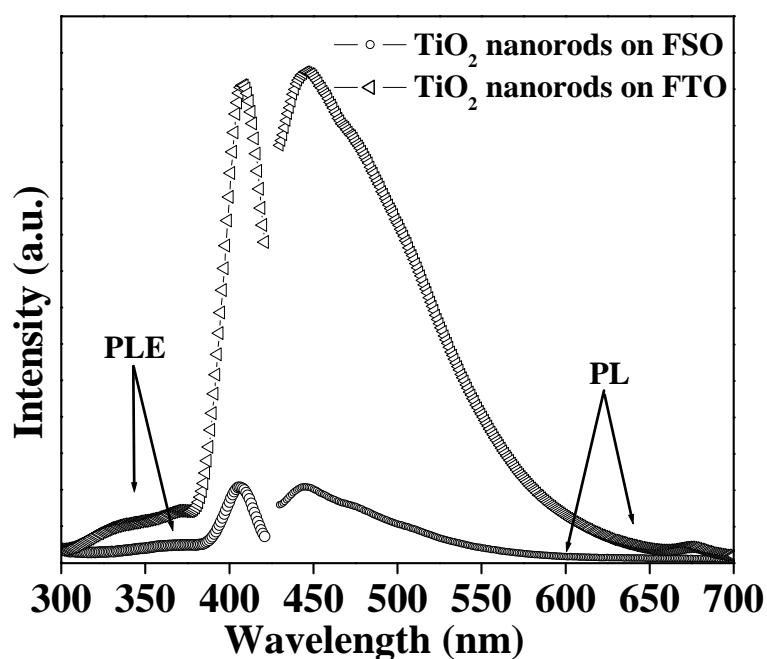


*Fig. 2.7: PLE and photoluminescence (PL) of  $\text{TiO}_2$  NRs grown on FTO and FSO glass substrates.*

### 2.3.5 Growth of TiO<sub>2</sub> NRs on Au-coated FTO substrate

To further explore the relation between surface chemistry of substrates and growth orientation and morphology of TiO<sub>2</sub> NRs, the surface of the substrate was modified by sputter-coating the FTO substrate with ~10 nm gold layer and this Au-coated FTO substrate was used to grow TiO<sub>2</sub> NRs following the same method as mentioned above while keeping all other parameters same.

#### 2.3.5.1 SEM analysis

The SEM images of a FTO substrate and ~10 nm Au-coated FTO substrate are shown in Fig.2.8. From the SEM images, it was quite difficult to conclude about the morphology and wettability of gold on FTO surface.

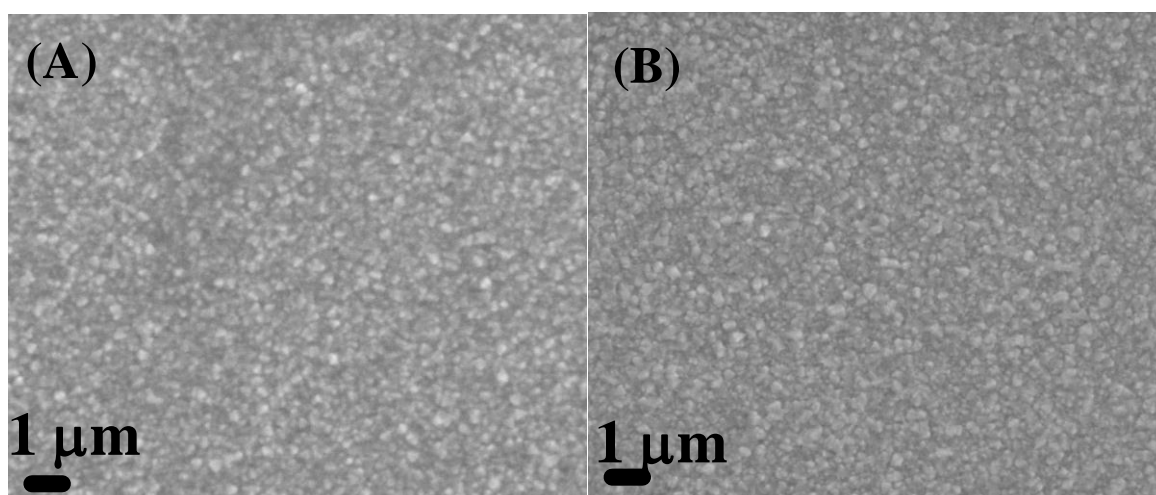


*Fig. 2.8: SEM images of (A) FTO substrate and (B) 10 nm Au coated FTO substrate.*

#### 2.3.5.2 STM analysis

So to further probe the Au-coating on FTO substrates, we performed STM measurements at room temperature and ambient pressure. The height image comparison for both the uncoated

and 10 nm gold coated substrates respectively along with the line scan analysis are shown in Fig.2.9 and Fig.2.10 respectively. It appeared from ‘height-profile STM’ images that there is a visible reduction in surface roughness however we do not expect a significant change in the FTO roughness from 10 nm Au film.

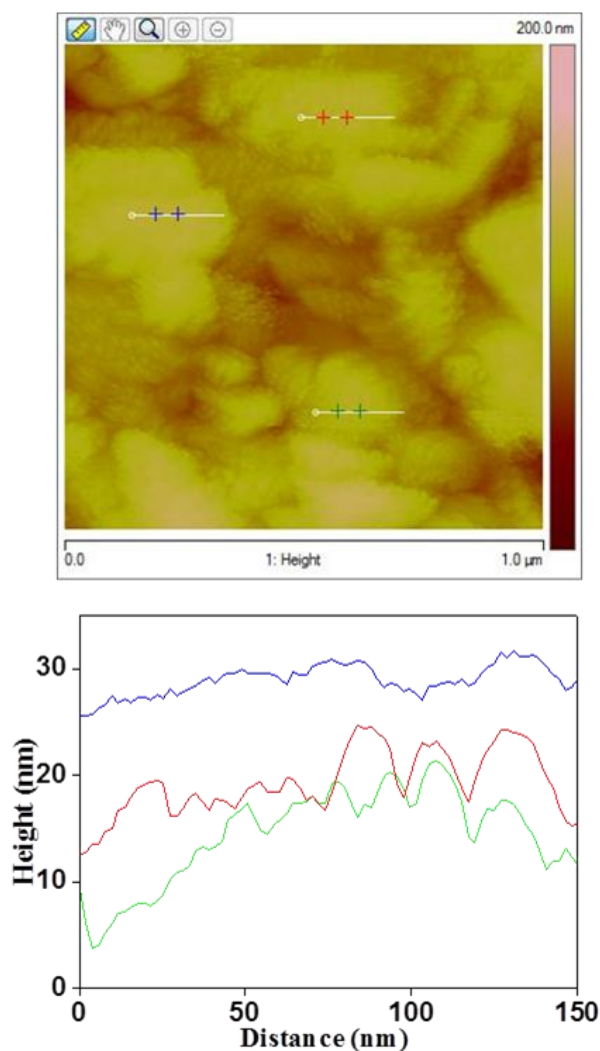


*Fig. 2.9: The top panel shows the STM height image on FTO substrate and the bottom panel shows the line scan analysis on the lines show in the top image. The respective line colors represent the marks in the top image where the analysis was done in top image.*

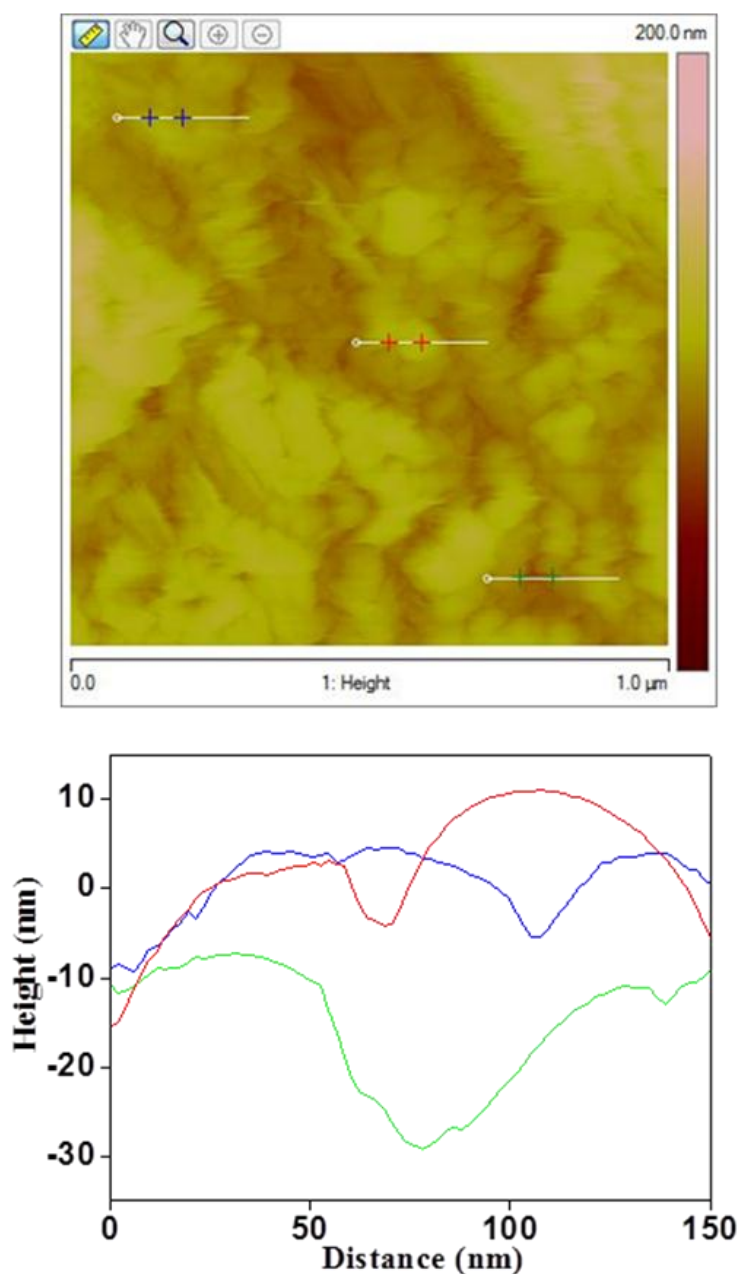


*Fig. 2.10: The top panel shows the STM height image on 10 nm Au-coated FTO substrate and the bottom panel shows the line scan analysis on the lines show in the top image. The respective line colors represent the marks in the top image where the analysis was done in top image.*

### 2.3.5.3 XRD analysis

Fig.2.11 showed the XRD image of the as synthesized TiO<sub>2</sub> NRs. From the XRD data, it is found that here too the (310) peak is the most intense peak with intensity much higher than usual reported value. The intensity of the peak is increased almost 10 times from 10 % to 100 %.

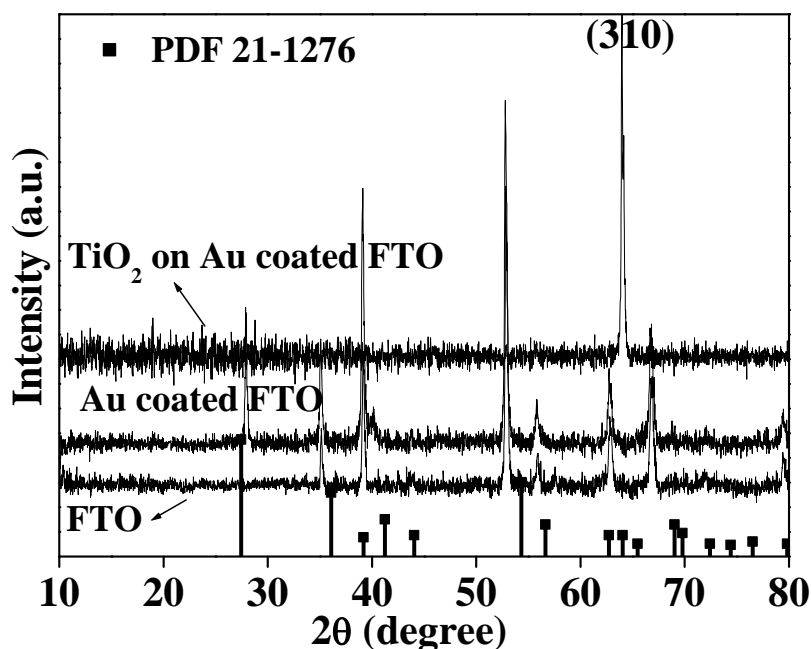


*Fig. 2.11: XRD pattern of TiO<sub>2</sub> NRs grown on 10 nm gold coated FTO substrate.*

### 2.3.5.4 SEM analysis

Fig. 2.12 showed the morphology of TiO<sub>2</sub> NRs by SEM images which revealed that, the TiO<sub>2</sub> NRs grown on Au-coated FTO substrate are relatively densely packed and they are highly oriented with respect to the substrate. In addition, it is observed that the diameter of the as-synthesized rods are quite bigger (~ 400 nm) in comparison to the rods grown on FTO coated substrate (~ 200 nm).

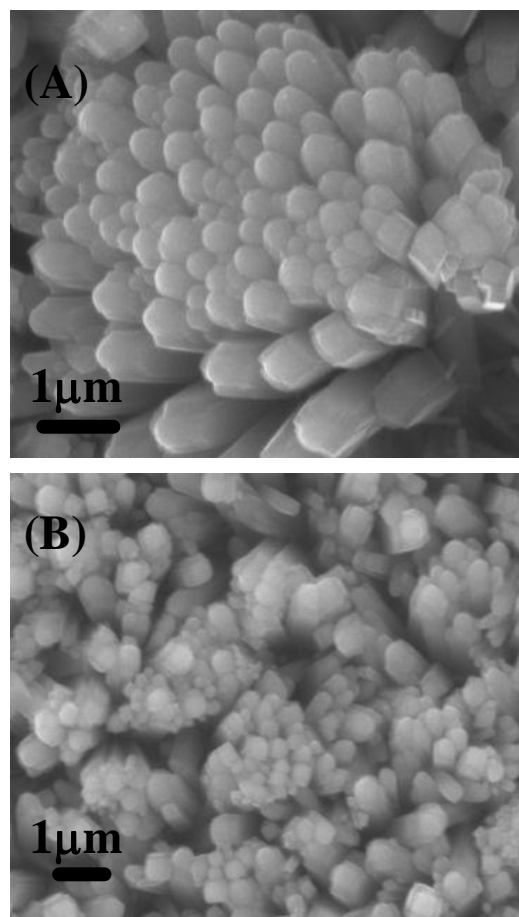


*Fig. 2.12: SEM images of TiO<sub>2</sub> NRs grown on 10 nm gold coated FTO substrate.*

### 2.3.5.5 Contact angle measurement

To investigate the probable reason behind this, wettability test was performed following the measurement of contact angles (Fig. 2.13) of FTO coated glass and ~ 10 nm gold coated FTO glass. It was found that the water contact angle of the gold coated FTO glass is 12° whereas for FTO substrate it is 36° which hints the increase in the hydrophilicity of the FTO substrate after coating it with gold might be one of the main reasons for the larger diameter of the titania NRs.

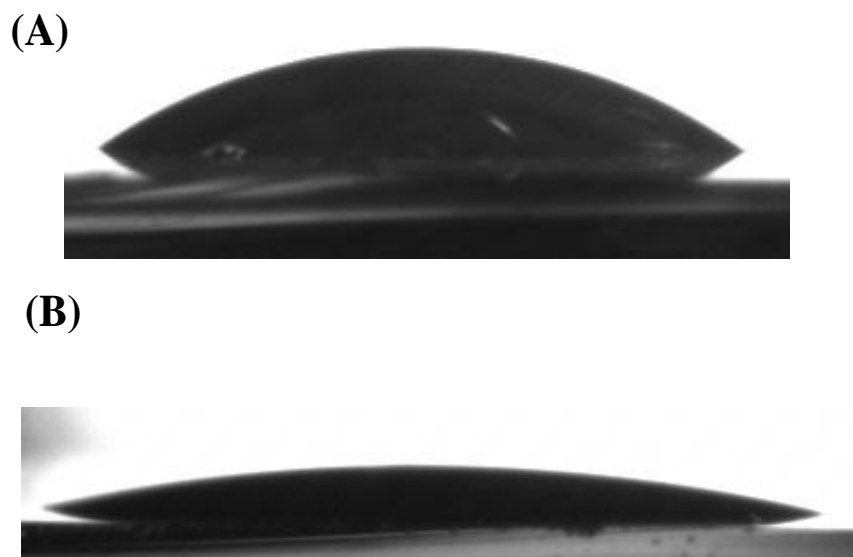


*Fig. 2.13: Water contact angle measurement of (A) FTO glass substrate (B) 10 nm gold coated FTO glass substrate.*

### 2.3.6 Photovoltaic properties

The as-synthesized single crystalline TiO<sub>2</sub> NR arrays, which are also directly grown on conducting FTO covered glass substrate, have huge application in DSSC. These single-crystalline oriented NRs grown on FTO substrate can effectively act as photoanode in DSSC. Due to the single crystalline structures of these NRs, rapid and efficient transfer of electrons takes place from the sensitizer to collecting conducting substrate. Moreover, as the NRs are directly synthesized on the transparent substrate, therefore more incident light can be passed through the backside of the photoelectrode and hence more photoelectrons are generated. Fig. 2.14 showed the J-V characteristic of the assembled solar cell under 100 mW/cm<sup>2</sup> illumination. The cell produced short-circuit current density of 8.01 mA/cm<sup>2</sup> and an open circuit potential of 0.66 V respectively. The fill factor and overall light to electricity conversion efficiency of the above-mentioned DSSC was 0.47 and 2.5% respectively. The

efficiency of the cells can be improved further by treating the cells with either  $\text{TiCl}_4$  or  $\text{NbCl}_5$ . The value of the power conversion efficiency of as prepared  $\text{TiO}_2$  NRs arrays based DSSC, without any treatment, compares well with the earlier reported efficiency value.<sup>28-31</sup>

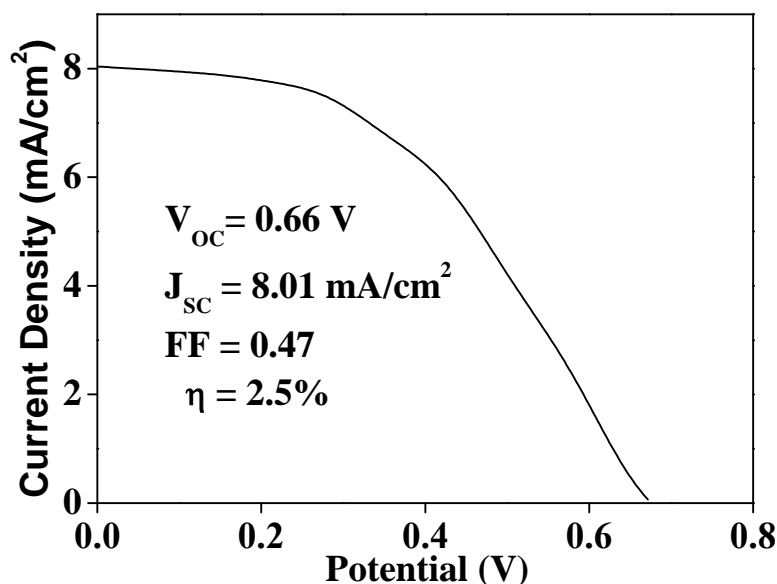


*Fig. 2.14: Current density vs. potential curves for dye sensitized solar cell fabricated from  $\text{TiO}_2$  NRs grown on FTO glass substrate.*

## 2.4 Conclusion

In summary, this paper deals with the growth mechanism and dependence of morphology of titania NRs on the surface chemistry of substrate. The  $\text{TiO}_2$  NRs were synthesized on different types of substrates and we found that  $\text{TiO}_2$  NRs can be grown on different planes if the material property of the substrate can be changed from crystalline to amorphous. We attempted to understand the reasons behind the growth of NRs in different plane and variation of diameter of the rods through various experiments such as XPS and contact angle measurement. The kinetically-controlled growth of (310) facet of  $\text{TiO}_2$  NRs on FTO-coated glass substrate were synthesized which is in contrast to the previously reported

(002) faceted TiO<sub>2</sub> NRs. Further, the growth of (110) facet TiO<sub>2</sub> NRs, using amorphous FSO as a substrate, was also demonstrated. It is also possible to tune the diameter of the NRs by playing with the surface chemistry of the substrate which can further be used for tuning the morphology of various 1D structures. Finally, power conversion efficiency of 2.5 % was achieved from the DSSC assembled with TiO<sub>2</sub> NRs grown on FTO substrate. It was understood that the 'light to electricity conversion efficiency' can be improved further by fine-tuning the length and diameter of the as-grown TiO<sub>2</sub> NR arrays. Thus, the proposed method can be used for the synthesis of various shapes and facet-controlled 1D-nanostructures.

### 2.5 References

1. M. V. Limaye, S. B. Singh, R. Das, P. Poddar and S. K. Kulkarni, *Journal of Solid State Chemistry*, 2011, **184**, 391-400
2. P. Poddar, Y. Sahoo, H. Srikanth and P. N. Prasad, *Applied Physics Letters*, 2005, **87**, 062506-1-3.
3. Y. Sahoo, P. Poddar, H. Srikanth, D. W. Lucey and P. N. Prasad, *Journal of Physical Chemistry B*, 2005, **109**, 15221-15225.
4. A. Fujishima and K. Honda, *Nature*, 1972, **238**, 37.
5. A. R. Armstrong, G. Armstrong, J. Canales, R. Garcia and P. G. Bruce, *Advanced Materials*, 2005, **17**, 862-865.
6. J. H. Braun, A. Baidins and R. E. Marganski, *Progress in Organic Coatings*, 1992, **20**, 105-138.
7. G. Pfaff and P. Reynders, *Chemical Reviews*, 1999, **99**, 1963-1981.
8. R. Zallen and M. P. Moret, *Solid State Communications*, 2006, **137**, 154-157.
9. Z. B. Zhang, C. C. Wang, R. Zakaria and J. Y. Ying, *Journal of Physical Chemistry B*, 1998, **102**, 10871-10878.
10. B. Oregan and M. Gratzel, *Nature*, 1991, **353**, 737-740.
11. Y. Y. Zhang, X. Y. Ma, P. L. Chen, D. S. Li and D. R. Yang, *Applied Physics Letters*, 2009, **94**, 1125-1127
12. K. D. Benkstein and S. Semancik, *Sensors and Actuators B-Chemical*, 2006, **113**, 445-453.
13. J. Joo, S. G. Kwon, T. Yu, M. Cho, J. Lee, J. Yoon and T. Hyeon, *Journal of Physical Chemistry B*, 2005, **109**, 15297-15302.

14. Y. Lei, L. D. Zhang, G. W. Meng, G. H. Li, X. Y. Zhang, C. H. Liang, W. Chen and S. X. Wang, *Applied Physics Letters*, 2001, **78**, 1125-1127.
15. C. T. Dinh, T. D. Nguyen, F. Kleitz and T. O. Do, *Acs Nano*, 2009, **3**, 3737-3743.
16. G. K. Mor, O. K. Varghese, M. Paulose and C. A. Grimes, *Advanced Functional Materials*, 2005, **15**, 1291-1296.
17. J. C. Lee, T. G. Kim, H. J. Choi and Y. M. Sung, *Crystal Growth & Design*, 2007, **7**, 2588-2593.
18. J. C. Lee, K. S. Park, T. G. Kim, H. J. Choi and Y. M. Sung, *Nanotechnology*, 2006, **17**, 4317-4321.
19. H. E. Prakasam, K. Shankar, M. Paulose, O. K. Varghese and C. A. Grimes, *Journal of Physical Chemistry C*, 2007, **111**, 7235-7241.
20. G. K. Mor, K. Shankar, M. Paulose, O. K. Varghese and C. A. Grimes, *Nano Letters*, 2005, **5**, 191-195.
21. G. K. Mor, K. Shankar, M. Paulose, O. K. Varghese and C. A. Grimes, *Applied Physics Letters*, 2007, **91**, 15211-1-3.
22. K. Zhu, N. R. Neale, A. Miedaner and A. J. Frank, *Nano Letters*, 2007, **7**, 69-74.
23. A. Solbrand, H. Lindstrom, H. Rensmo, A. Hagfeldt, S. E. Lindquist and S. Sodergren, *Journal of Physical Chemistry B*, 1997, **101**, 2514-2518.
24. A. C. Fisher, L. M. Peter, E. A. Ponomarev, A. B. Walker and K. G. U. Wijayantha, *Journal of Physical Chemistry B*, 2000, **104**, 949-958.
25. J. van de Lagemaat, N. G. Park and A. J. Frank, *Journal of Physical Chemistry B*, 2000, **104**, 2044-2052.
26. M. Law, L. E. Greene, J. C. Johnson, R. Saykally and P. D. Yang, *Nature Materials*, 2005, **4**, 455-459.
27. J. B. Baxter and E. S. Aydil, *Applied Physics Letters*, 2005, **86**, 053114-1-3.

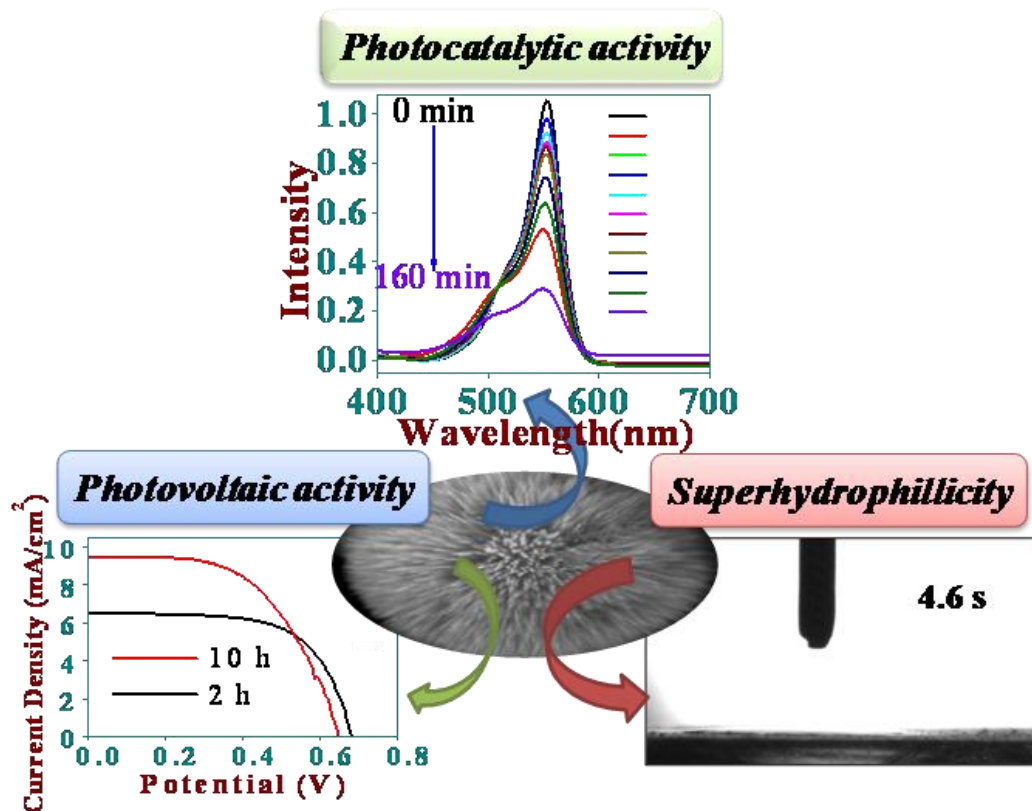
## Chapter 2

---

28. X. J. Feng, K. Shankar, O. K. Varghese, M. Paulose, T. J. Latempa and C. A. Grimes, *Nano Letters*, 2008, **8**, 3781-3786.
29. B. Liu and E. S. Aydil, *Journal of the American Chemical Society*, 2009, **131**, 3985-3990.
30. A. Kumar, A. R. Madaria and C. W. Zhou, *Journal of Physical Chemistry C*, 2010, **114**, 7787-7792.
31. H. E. Wang, Z. H. Chen, Y. H. Leung, C. Y. Luan, C. P. Liu, Y. B. Tang, C. Yan, W. J. Zhang, J. A. Zapien, I. Bello and S. T. Lee, *Applied Physics Letters*, 2010, **96**, 263104-1-3.
32. R. L. Penn and J. F. Banfield, *Science*, 1998, **281**, 969-971.
33. Q. Huang and L. Gao, *Chemistry Letters*, 2003, **32**, 638-639.
34. P. D. Cozzoli, A. Kornowski and H. Weller, *Journal of the American Chemical Society*, 2003, **125**, 14539-14548.
35. Y. W. Jun, M. F. Casula, J. H. Sim, S. Y. Kim, J. Cheon and A. P. Alivisatos, *Journal of the American Chemical Society*, 2003, **125**, 15981-15985.
36. J. J. Wu and C. C. Yu, *Journal of Physical Chemistry B*, 2004, **108**, 3377-3379.
37. J. M. Wu, H. C. Shih and W. T. Wu, *Nanotechnology*, 2006, **17**, 105-109.

## Chapter III

**Growth of surfactant free 3D TiO<sub>2</sub> microsphere assembly on transparent conducting oxide substrate for photovoltaic and photocatalytic applications**



### Outline

---

Owing to the combination of micro and nanometer scaled building blocks, 3D structures composed of several 1D units, show unique physicochemical properties, compared to only 1D structures. Intermingling of micro and nanostructures provide larger surface to volume ratio which aids to improve the performance of various optoelectronic devices. We have synthesized surfactant-free, radially-assembled, 3D-titania microsphere arrays (TMSAs) composed of bundles of single-crystalline NWs with tunable architecture, directly on FTO substrates. The effects of reaction time and titania precursor on the formation morphology of the microspheres have been studied thoroughly. The as-grown microsphere film showed superhydrophilicity without prior UV irradiation. The parallel alignment NWs in microspheres led to micro-capacitors like feature which showed a stable dielectric performance. The photocatalytic and photon to electron conversion efficiencies of the self-assembled titania microspheres, using as an anode in DSSC, were also measured. The as-synthesized microspheres on FTO for 10 h showed significant improvement of photo conversion efficiency (45 %) due to the synergistic effect of larger surface area and an increase in the photon scattering layer compare to 2 h growth.

---

### 3.1 Introduction

Among transition metal oxide semiconductors, designing and growth of TiO<sub>2</sub> nanostructures has been extensively studied for several decades owing to its interesting optical, dielectric and catalytic properties.<sup>1</sup> These promising physicochemical properties of titania led to a wide range of applications in solar photovoltaics, photoelectrochemical water splitting, fuel-cells, pigment, paint, sunscreen, super hydrophobic and hydrophilic materials *etc.*<sup>2-15</sup> To date, among all the photocatalysts, titania is the most apposite one, due to its role as an oxidizer, chemical and biologically inertness, low-cost and long term stability.<sup>16</sup>

Crystalline TiO<sub>2</sub> exhibits three different types of polymorphs i.e. rutile, anatase and brookite. Among these polymorphs, rutile is thermodynamically more stable, inert, and possesses a larger refractive index (2.6), opacity, scattering-efficiency and is known for its photocatalytic properties.<sup>1</sup> The (110) surface of rutile TiO<sub>2</sub> has been extensively studied for photocatalytic activity and also to simulate photocatalytic properties under high vacuum conditions.<sup>17</sup> Generally, the rutile -TiO<sub>2</sub> is obtained by the calcinations of anatase phase at high temperature. One step synthesis of template-free, rutile TiO<sub>2</sub> at low temperature, through the simple chemical method, with specific morphology and size, is still a challenging task which is due to the complex chemistry of titania surface. Geometrical shape of TiO<sub>2</sub> plays an important role in dictating its physical properties. In 1D structures charge transport is highly favored due to the reduction in grain boundaries and lattice imperfections.<sup>18,19</sup>

One dimensional nanostructures are known for slow recombination rate and fast electron transport, where as 3D nanostructures provide effective surface area for dye-adsorption and excellent photon scattering.<sup>20</sup> Due to the combination of micro and nanometer scaled building-blocks, 3D structures composed of several 1D units show unique properties

compared to only 1D structures. Intermingle of micro and nanostructures provide larger surface to volume ratio which aid to improve the performance for various optoelectronic applications. Immobilization of 1D or 3D structures on solid substrate is required for device fabrication and various other applications. Direct hydrothermal growth of titania 3D structures on solid surface eradicate the need of post- synthesis fixation of the material for further use.

We have synthesized surfactant free radially assembled 3D-TMSAs composed of number of single-crystalline NWs with tunable architecture directly on FTO substrates by a facile low temperature hydrothermal method which is especially suitable for photoelectrochemical and photocatalytical applications. The morphology of the 3D-TMSAs can be tuned by varying the growth time. Due to comparatively large surface area of these hierarchical structures and superior light scattering ability, these structures are preferred for solar cell applications.<sup>21</sup> The sub-micron area of the 3D-TMSAs is composed of numerous NWs, are proved to generate effective light scattering due to their size compatibility to the wavelength of visible light spectrum.<sup>20</sup> The titania precursor plays an important role in directing and controlling the surface topography of the microspheres which is also studied in this work. The as-grown 3D-TMSAs film on FTO substrates possesses superhydrophilic properties without any UV irradiation treatment attributed to the presence of layered and rough surface. These self-assembled 3D-TMSAs also show superior dielectric behaviour as they are consisted of bunches of NWs, accompanied with nanoscale boundary cavities, which can produce large polarization.<sup>22</sup> The photon to electron conversion efficiency of the DSSC fabricated from 3D-TMSAs has also been measured, where the dye-adsorbed 3D-TMSAs were used as photoanode. The photocatalytic activity of the as-grown microspheres has also

been explored and it was found that the activity remained almost unchanged upto three consecutive cycles.

## 3.2 Materials and method

### 3.2.1 Materials

All chemicals were of analytical grade and used as-received without any further purification, unless otherwise described.  $\text{Ti}(\text{OBU})_4$  (purity  $\geq 97\%$ ), titanium  $\text{TiCl}_4$  (purity  $\geq 98\%$ ) and 1,4-dioxane were purchased from Sigma-Aldrich Inc. FTO coated glass (sheet resistance = 8 ohm/square) substrate and N-719 dye were received from Solaronix SA Switzerland.

### 3.2.2 Synthesis of 3D-TMSAs on FTO substrates

Hierarchical 3D-TMSAs, in which,  $\text{TiO}_2$  NWs were assembled as nanoflowers, were synthesized through a simple hydrothermal method. First, the substrates were ultrasonically cleaned in a mixed solution of deionised water, acetone and isopropanol and then dried in  $\text{N}_2$  flow. A mix of 10 mL di-oxane and 1 mL concentrated HCl (35 %) was stirred for 10 min in a beaker followed by the addition of 1 mL  $\text{Ti}(\text{OBU})_4$  and 1 mL  $\text{TiCl}_4$ . The solution was then stirred for 10 min for proper mixing and then transferred into a 25 mL Teflon vessel and the substrates were placed horizontally within the Teflon vessel. Then the vessel was loaded inside an autoclave and was heated at 180 °C for (2-12 h) for hydrothermal reactions. After synthesis, the substrates were washed with DI water and then dried in air. To study the effect of precursors, only 2 mL  $\text{Ti}(\text{OBU})_4$  and 2 mL  $\text{TiCl}_4$  were added individually in two separate reactions. Earlier toluene was used as non-polar solvent to synthesize titania nanorods.<sup>18</sup> But in this method 1-4-dioxane is used as nonpolar solvent as according to Hansen solubility

parameter values hydrogen bonding values of 1-4-dioxane is much greater than toluene where as the value of other parameters like polar and dispersion bond remain almost similar.

### 3.2.3 Fabrication of DSSC

To fabricate a solar cell, at first, the as-synthesized nanoflower on FTO substrate was annealed in air at 400 °C for 30 min, followed by cooling the substrate to 80 °C and was immersed in a 0.5 mM ethanolic solution of N-719 dye for 24 h in order to enable sufficient adsorption of dye which acts as the sensitizer in the presence of light. After complete dye adsorption, the substrate was washed very carefully with ethanol and dried for 1 h. After that, a platinum coated FTO substrate, used as the counter-electrode, was placed above the dye adsorbed FTO substrate and an electrolyte containing 0.6 M 1-hexyl-2-3-dimethylimidazolium iodide, 0.1 M LiI, 0.05 M I<sub>2</sub> and 0.5 M 4-tert-butylpyridine in methoxyacetonitrile was injected into the space between the anode and the cathode to complete the assembly of the DSSC.

### 3.2.4 Characterization techniques

In order to confirm the crystalline phase of TiO<sub>2</sub> NWs, XRD study was carried out using a PANalytical X'PERT PRO instrument and the iron-filtered Cu-K<sub>α</sub> radiation ( $\lambda = 1.5406 \text{ \AA}$ ) in the  $2\theta$  range of 10-80° with a step size of 0.02°. To analyze the shape and size of the 3D-TMSAs scanning electron microscopy (FEI Quanta 200 environmental scanning microscope) was done. The specific structure details and morphology of the 3D-TMSAs were obtained by using FEI Tecnai F30 HRTEM equipped with a super-twin lens (s-twin) operated at 300 keV accelerating voltage with Schottky field emitter source with maximum beam current (> 100 nA) and small energy spread (0.8 eV or less). The point-to-point resolution of the microscope is 0.20 nm and line resolution of 0.102 nm with a spherical aberration of 1.2 mm and chromatic aberration of 1.4 mm with 70  $\mu\text{m}$  objective aperture size.

The powders obtained were dispersed in acetone and then drop-casted on carbon-coated copper TEM grid with 200 mesh and loaded to a single tilt sample holder. To further confirm the crystalline phase, Raman spectroscopy measurements were recorded at room temperature on an HR 800 Raman spectrophotometer (Jobin Yvon, Horiba, France) using monochromatic radiation (achromatic Czerny-Turner type monochromator with silver treated mirrors) emitted by a He-Ne laser (633 nm), operating at 20 mW and with accuracy in the range between 450 nm and 850 nm  $\pm 1$  cm<sup>-1</sup>, equipped with thermoelectrically cooled (with Peltier junctions), multi-channel, spectroscopic grade charge coupled detector (1024×256 pixels of 26 microns) with dark current lower than 0.002 electrons pixel<sup>-1</sup> s<sup>-1</sup>. An objective of 50 X LD magnification was used both to focus and collect the signal from the samples. UV-vis spectroscopy measurements were performed on a Jasco UV-vis-NIR (Model V570) dual beam spectrometer operated at a resolution of 2 nm. PL spectra were acquired using a Fluorolog Horiba Jobin Yvon fluorescence spectrophotometer, equipped with a 400 W Xe lamp as an excitation source and a Hamamatsu R928 photomultiplier tube (PMT) as a detector. Current-voltage characteristics were calculated by irradiated the cell with 100 mW/cm<sup>2</sup> (450 W xenon lamp, Oriel instrument), 1 sun AM 1.5 G filter was used to simulate the solar spectrum. The active area of the cell was 0.5 cm<sup>2</sup>. The photocurrent was measured by using a Series 2400 Source Measure Unit from Keithley Instruments, Inc., Cleveland, Ohio.

The photocatalytic activity of 3D-TMSAS on FTO substrate after 10 h of hydrothermal reaction was evaluated by the degradation of rhodamine blue dye (RhB) in sunlight. The FTO substrate covered with TiO<sub>2</sub> microsphere was kept in 30 mL of 10<sup>-5</sup> M RhB solution in dark for 1 h to attain the adsorption-desorption equilibrium. After that, the solution was

irradiated in sunlight and at a given time interval 2 mL of the solution was withdrawn and UV–vis absorption spectra of RhB were recorded.

For dielectric measurement, the 3D-TMSAs grown on FTO substrate for 10 h were pressed into 13 mm circular pellet and to probe the dielectric response, impedance spectroscopy was carried out in room temperature using Novacontrol Beta NB Impedance Analyser with home built sample holder coupled with Janis cryostat. The data were recorded in a frequency range 1 to  $10^6$  Hz at 1 V (rms).

### 3.3 Results and Discussion

#### 3.3.1 X-Ray diffraction study

XRD study was carried out to confirm the crystallinity and phase purity of the 3D-TMSAs. All the distinct diffraction peaks matches well with the tetragonal rutile phase of  $\text{TiO}_2$  and no additional phases were observed. Fig. 3.1 compares the XRD patterns of 3D-TMSAs grown on FTO substrate after hydrothermal synthesis, for varying time from 2 h to 12 h, only FTO coated glass substrate, and PDF file # 21-1276.

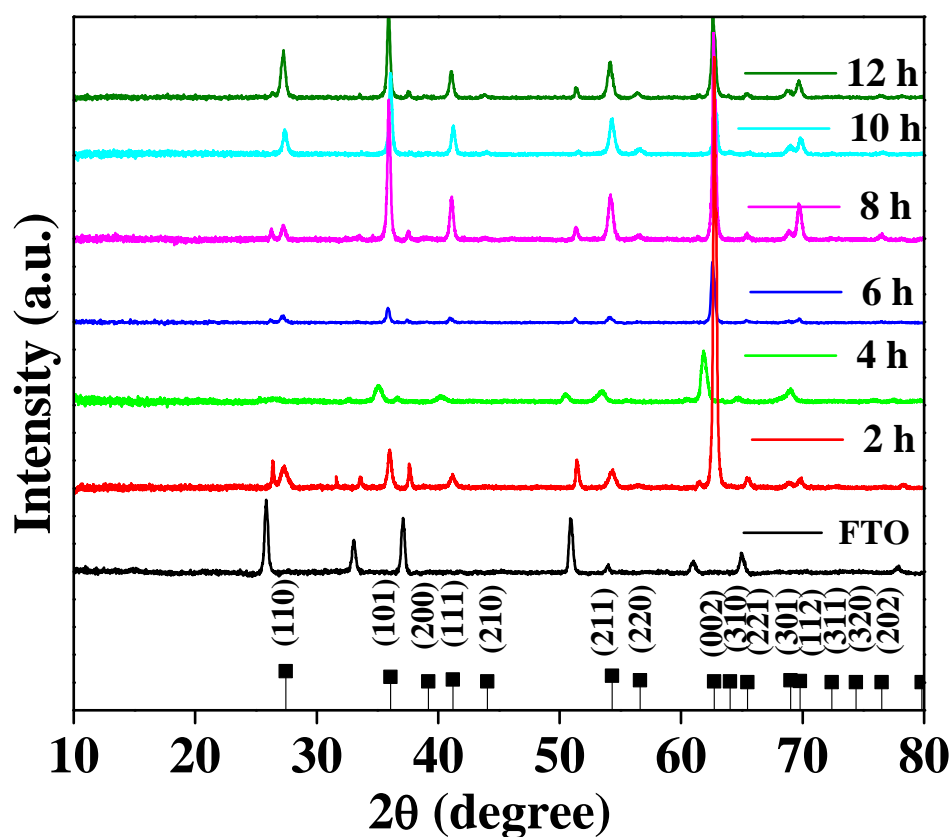


*Fig. 3.1: XRD patterns of 3D rutile TiO<sub>2</sub> microspheres directly grown on FTO substrate with different reaction time.*

The characteristic peaks of SnO<sub>2</sub> were observed in all the samples, proving that the 3D-TMSAs were directly grown on FTO substrates. The intensity of the diffraction peaks increased with prolonging reaction time, indicating highly crystalline structure. Moreover, after analyzing the diffraction patterns it was found that the intensity of the (002) peak was enhanced almost three times from 10 % to 30 % compared to the standard data file (PDF data file # 21-1276) which confirmed that the 3D-TMSAs were clustered by bunches of 1D NWs.

### 3.3.2 Determination of shape and size

#### 3.3.2.1 SEM analysis

The morphology of the as-synthesized 3D-TMSAS was studied through SEM. Fig. 3.2 showed the SEM images of the 3D-TMSAS at different magnifications. It was cleared from the images that the entire substrate was uniformly covered by titania microspheres, 3D-TMSAS indicating a continuous growth. From the high magnification images it was confirmed that the bunch of wires constitutes the microspheres. The NWs were found to arrange densely on the surface having diameter 5  $\mu\text{m}$  with no irregular aggregation. The films were homogeneous, continuous and strongly adhered and no cracks were seen on the surface. The 3D-TMSAS were assembled by single-crystalline rutile NWs radiate outward direction from the centre of the sphere. From the EDX data the atomic ratio of Ti to O is found to be 1: 2. The image obtained confirms that each microsphere is consisted of with bunch of NWs (diameter  $\sim$  10 nm).

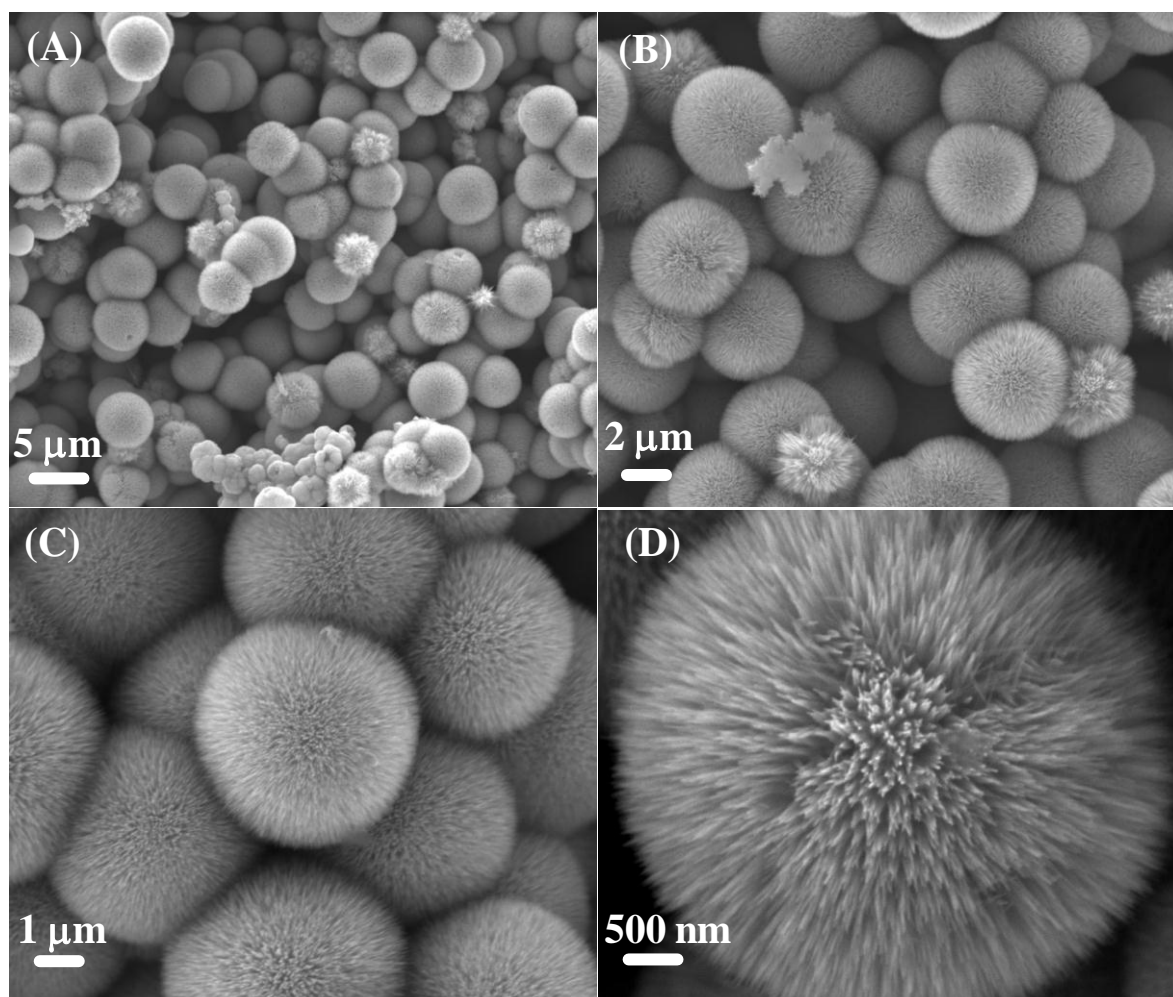


*Fig. 3.2: (A)–(D) SEM images of 3D rutile  $\text{TiO}_2$  microspheres grown on FTO substrate after 8 h of hydrothermal reaction with different magnifications.*

### 3.3.2.2 TEM analysis

The TEM images also revealed that the microspheres were made up with loosely packed bunch of thin rods (Fig. 2.3(A)-(D)). To further get acquainted with the microstructure, TEM study of a single thin rod was done (Fig. 3.4). The observed lattice fringes and FFT pattern (Fig. 3.4 (C) & (D)) confirmed that each rod is single-crystalline along their entire length. The interplanar distance of 0.14 nm corresponds well with the rutile phase of titania.

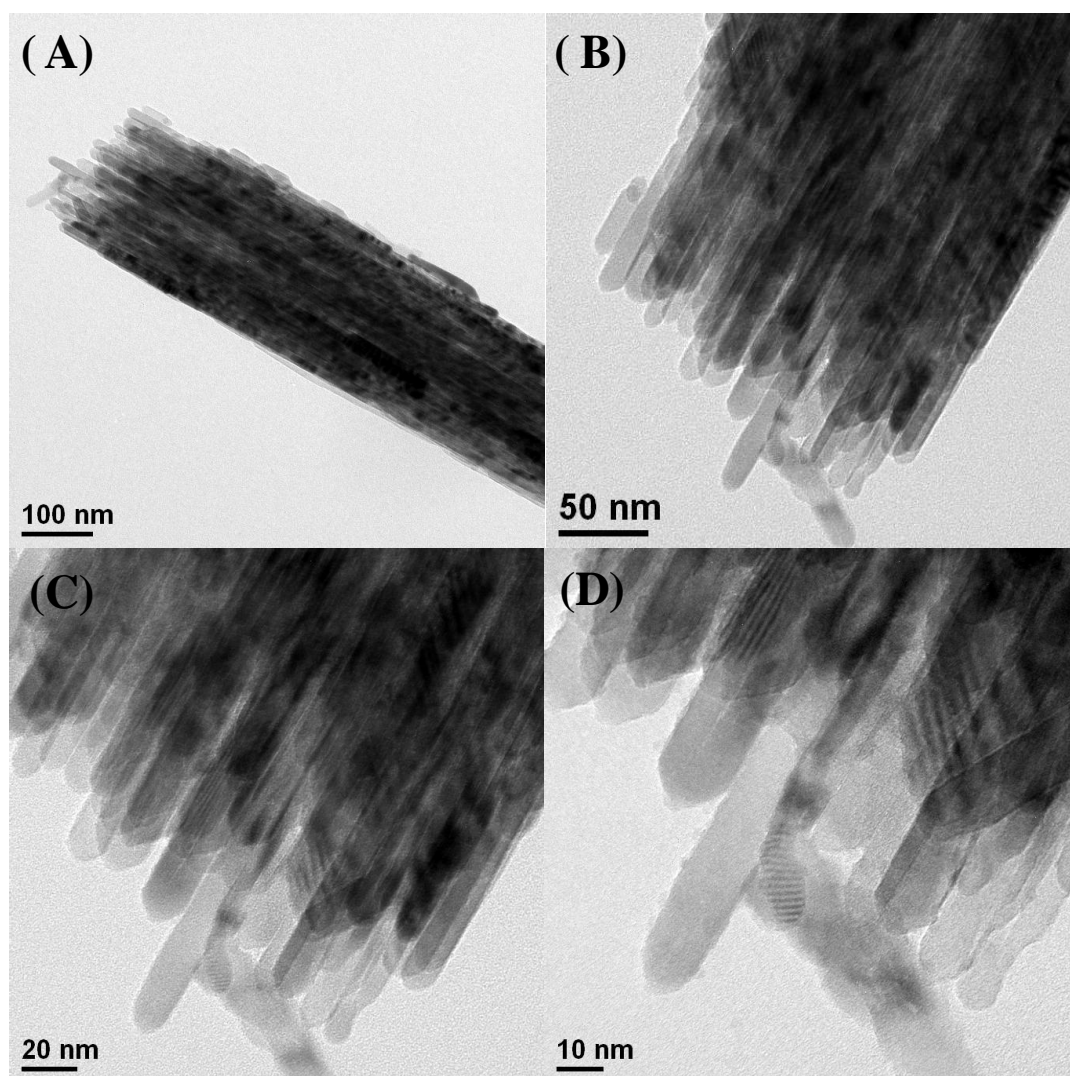


*Fig. 3.3: (A)–(D) TEM micrograph of TiO<sub>2</sub> NWs of a microsphere with different magnifications.*

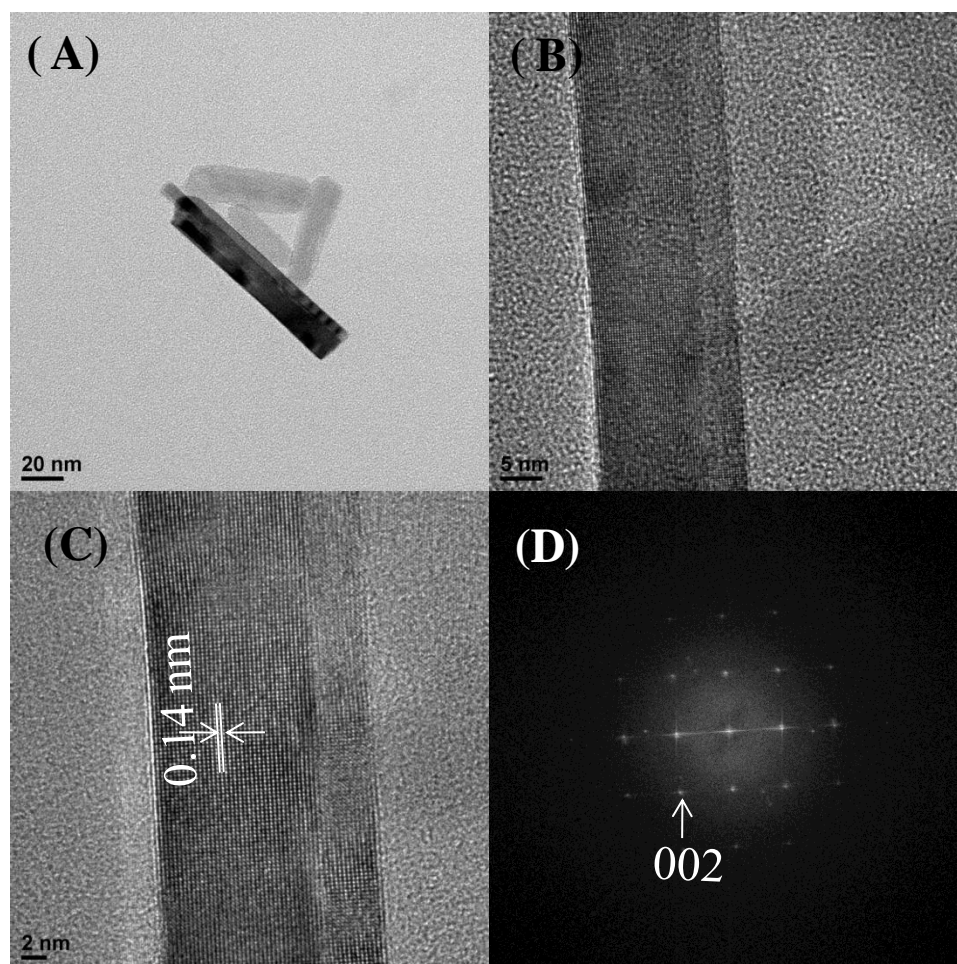


*Fig. 3.4: (A)–(C) TEM images of single TiO<sub>2</sub> NWs with different magnifications.*

*(D) FFT pattern of the NW.*

### 3.3.3 Growth mechanism

#### 3.3.3.1 Effect of time

In order to know more niceties of the formation morphology of the 3D-TMSAs and to get acquainted with the plausible growth mechanism, a series of time dependent growth of the microspheres have been studied thoroughly. From the SEM images, it was found that after 2 h reaction time, a seed layer started to grow and the surface coarsen. It is assumed, that at an early stage homogeneous nucleation of TiO<sub>2</sub> is favoured as the reaction solution become supersaturated and thus, TiO<sub>2</sub> seed layer formed on FTO surface (Fig. 3.5(A)). The

formation of these microspheres is very similar to the blooming of flower. After 6 h reaction, ordered NW based flower like microspheres with uniform morphology started to blossom (Fig. 3.5(C)). With prolonging reaction time, the density of the wires in the bunch of a microsphere started to increase and when the growth time was 8 h, formation of a double layer initiated lead to decrease the size of the solid core. (Fig. 3.5(D)). As the reaction progress, the architecture of the microsphere turned from spherical to quasispherical. Finally, hierarchical sea-urchin like structure having average diameter  $\sim 4 \mu\text{m}$  formed (Fig. 3.5(E)). After 12 h of hydrothermal growth, the NWs adhered with each other and produced a textured film (Fig. 3.5(F)).

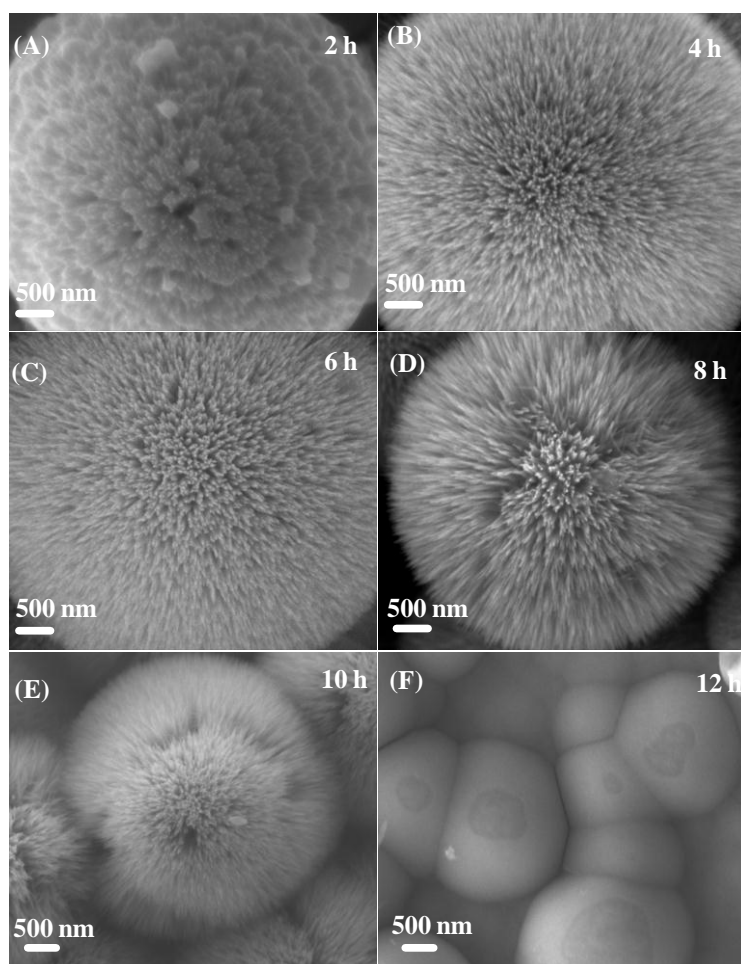
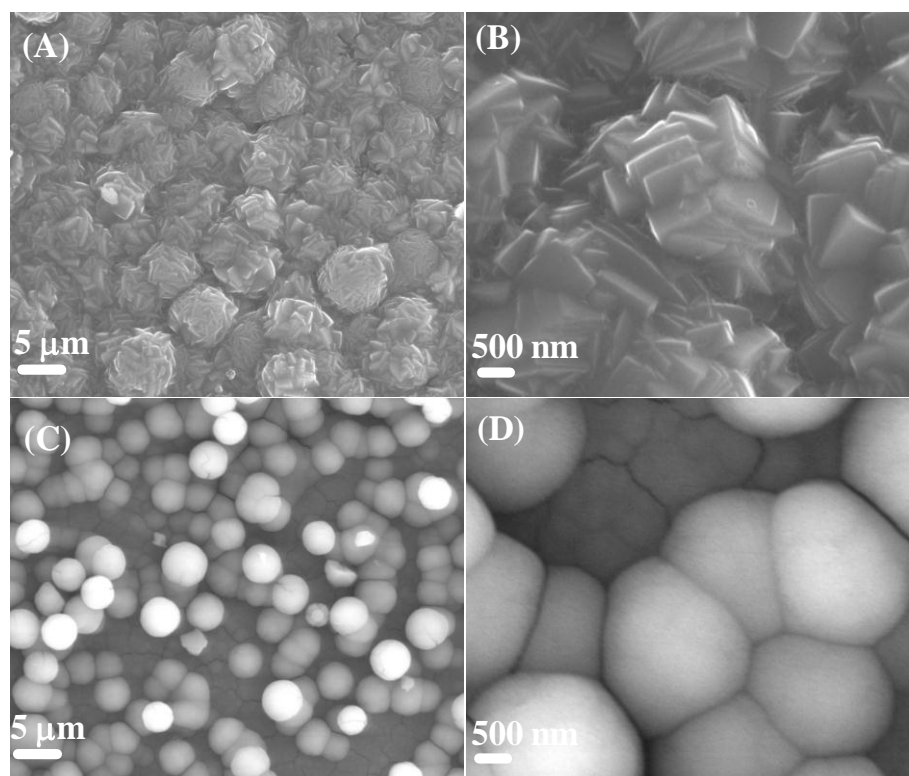


**Fig. 3.5:** (A)–(F) SEM images of 3D rutile  $\text{TiO}_2$  microspheres grown on FTO substrates with varying reaction time.

### 3.3.3.2 Effect of precursor

To further probe the effect of precursor on the synthesis of  $\text{TiO}_2$  microspheres, titania nanoparticles were synthesized on FTO substrates, by hydrothermal reaction for 4 h using only  $\text{Ti}(\text{OBU})_4$  and  $\text{TiCl}_4$  as precursor respectively. It was seen from the images, that when only  $\text{TiCl}_4$  is used as precursor faceted truncated bipyramidal nanocrystals are formed (Fig. 3.6(A), (B)), whereas an agglomerated film was formed when only  $\text{Ti}(\text{OBU})_4$  was used (Fig. 3.6(C), (D)). It is known that the rate of hydrolysis of  $\text{TiCl}_4$  is very fast and thus generate *in situ* HCl, which capped {001} surface and reduced the surface energy. As a consequence, the growth of (001) surface with respect to other plane decelerated and  $\text{TiO}_2$  crystals continued to grow along [100] and [010] direction and {001} faceted growth of rectangular parallelepiped is favoured.<sup>23</sup>

**Fig. 3.6:** (A)–(F) SEM images of rutile  $\text{TiO}_2$  grown on FTO substrate using different precursors (A, B)  $\text{TiCl}_4$ , (C, D)  $\text{Ti}(\text{OBU})_4$ .



### 3.3.4 Optical properties

#### 3.3.4.1 Photoluminescence study

The optical properties of the as-synthesized 3D-TMSAs were studied through photoluminescence and Raman spectroscopy. Fig.3.7 showed the room temperature photoluminescence property of the as-synthesized 3D-TMSAs grown on FTO for 2 and 10 h of hydrothermal reaction respectively. The microspheres showed strong and wide PL signal, attributed to binding excitons at a range from 400 to 600 nm at 380 nm excitation wavelength.<sup>24-26</sup> Corresponding PLE spectra exhibited absorption at 410 nm (Fig.3.7). It is known from literature that rutile TiO<sub>2</sub> NWs emit free excitons as the coordination number is the largest of all.<sup>27</sup> The peak around 415 nm (~ 2.98 eV) is due to interband electron transition in rutile TiO<sub>2</sub> NWs, from conduction band to valence band.<sup>25</sup> The characteristic peak of rutile TiO<sub>2</sub> at 464 nm correspond to metal ligand charge transfer.<sup>1</sup> The PL emission intensity can be associated to the recombination dynamics of the excited excitons.<sup>28</sup> The enhanced intensity of the PL peaks for microspheres grown on FTO substrates for 10 h attributed to the change in surface structure of the material, which results into change in oxygen vacancies and effective surface area for photon absorption.

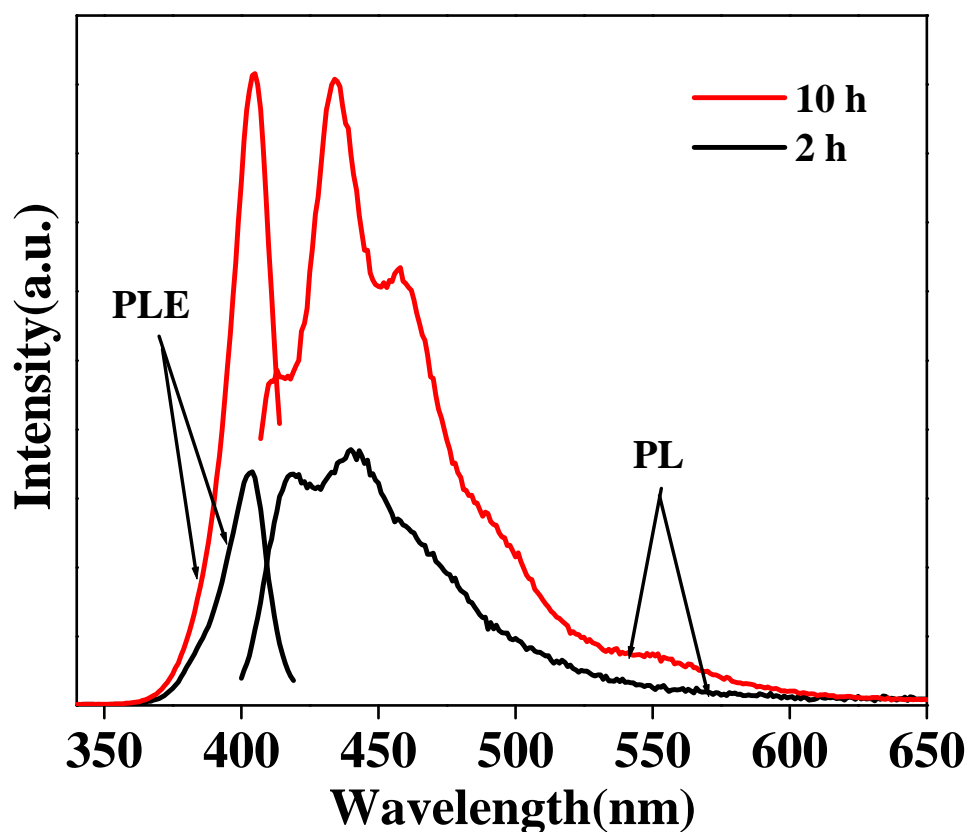


*Fig. 3.7: PLE and PL spectra of TiO<sub>2</sub> microspheres grown on FTO substrate after 2 and 10 h of hydrothermal reaction.*

#### 3.3.4.2 Raman study

Room temperature Raman spectroscopy was performed to identify the vibrational properties and phase purity of the as-synthesized 3D-TMSAs, grown on FTO substrate after 2 and 10 h of hydrothermal reaction respectively. The two Raman active fundamental vibration modes,  $E_g$  ( $\sim 444\text{ cm}^{-1}$ ) and  $A_{1g}$  ( $\sim 610\text{ cm}^{-1}$ ) and the second order effect at  $\sim 244\text{ cm}^{-1}$ , caused by multiple phonon vibration of  $B_{1g}$  mode, can be clearly spotted in both the samples (Fig.3.8). These Raman active fundamental modes are attributed to the motions of  $O^{2-}$  anions with respect to stationary central  $Ti^{4+}$  cation either perpendicular ( $B_{1g}$ ,  $A_{1g}$ ) or along ( $E_g$ ) the  $c$

axis.<sup>29</sup> The  $E_g$  and  $A_{1g}$  modes are regarded as the asymmetric bending and symmetric stretching of O-Ti-O bonds in the  $\{001\}$  and  $\{110\}$  plane respectively due to the opposite moving of O atoms across O-Ti-O bond. Besides, an increase in intensity, the peak height to half-width ratio also gets enhanced for  $TiO_2$  microspheres grown on FTO substrate for 10 h. This outcome, might be considered as an effect of grain size and crystalline properties attributable to phonon confinement behaviour.<sup>30-31</sup>

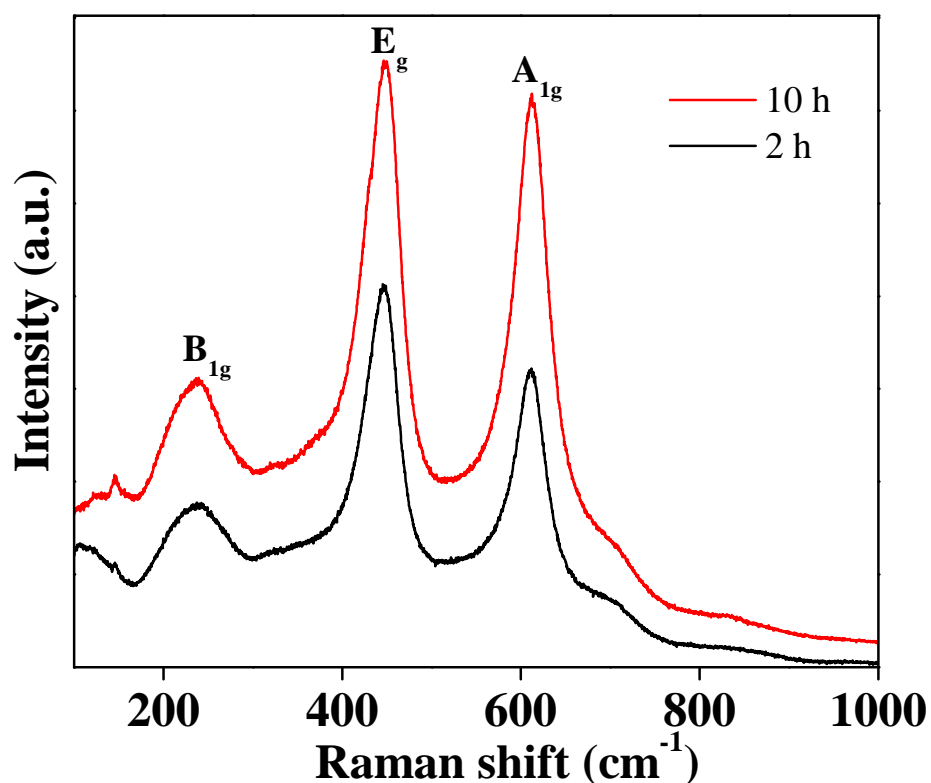
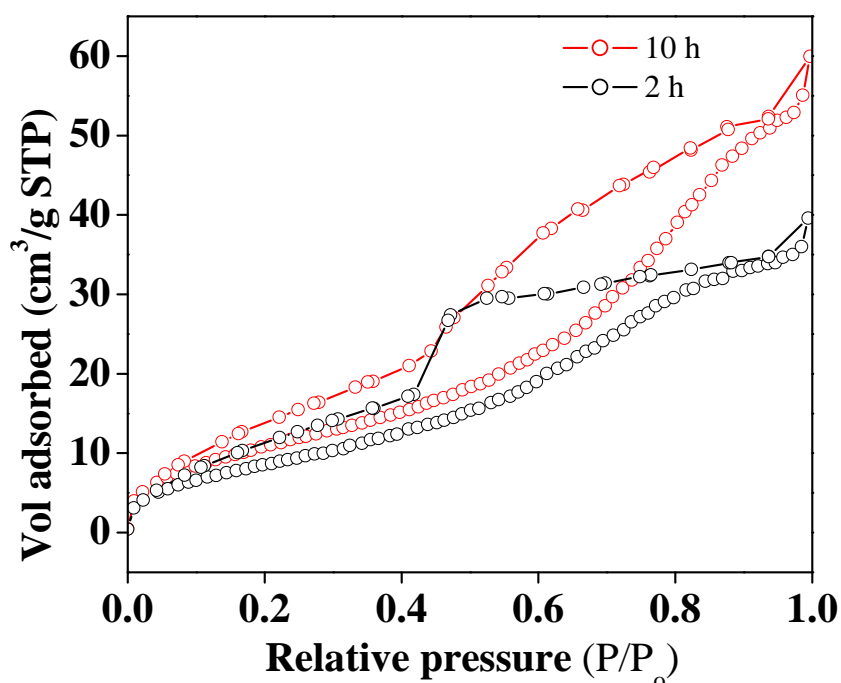


**Fig. 3.8:** Raman spectra for  $TiO_2$  grown on FTO substrate for 2 and 10 h of hydrothermal reaction.

### 3.3.5 BET study

Materials possessing larger specific surface area are ideal to facilitate light scattering. The surface area of the microspheres was measured through Brunauer–Emmett–Teller (BET) adsorption analysis. The presence of more surface active sites enhances the adsorption capacity of the dye as well as the light harvesting and scattering probability. According to Brunauer–Demming–Demming–Teller (BDDT) classification, the  $N_2$  adsorption-desorption isotherms (Fig.3.9) of the 3D-TMSAs showed type IV isotherms with  $H_2$  type hysteresis loop, signifying the presence of mesopores.<sup>32-33</sup> Using BET multipoint method, the specific surface area of the microsphere grown on substrate for 2 h and 10 h were found to be 33 and 46  $m^2/g$ , respectively. It was observed that for the double layer titania microsphere, the



surface area increases which also favor the rapid diffusion of charges.

**Fig. 3.9:**  $N_2$  adsorption and desorption isotherm of  $TiO_2$  grown on FTO substrate for 2 and 10 h of hydrothermal reaction.

### 3.3.6 Photovoltaic property

The as-synthesized 3D-TMSAs, directly grown on conducting FTO substrates have huge application as photoanode, in sensitized solar cells. As the microspheres are consisting of bunches of single-crystalline NWs, rapid and efficient transfer of electrons take place from the sensitizer to collecting conducting substrate through these NWs. In addition to that, the microspheres are directly grown on FTO substrates which will effectively pass and scatter the incident light through the backside of the photoelectrode and thus, able to generate more photoelectrons. The UV-vis absorption spectra of the dye molecule adsorbed on the microsphere surface (Fig.3.10) showed an absorption peak around 515 nm. The most intense absorption peak was found for microspheres grown on FTO substrate for 10 h compare to 2 h of growth. The microspheres having double layer of titania nanowires, having outward growth, exhibited strong absorption peak, implying the most successful consumption and effective trapping of incident photon inside the film, to increase the absorption. Consequently, a huge portion of the incoming photon will be back to the film and the light harvesting property of the photoanode is improved. The roughness and effective surface area of the microspheres increased with increase in reaction time and thus amount of dye adsorption is also enhanced which can also be confirmed from BET data.

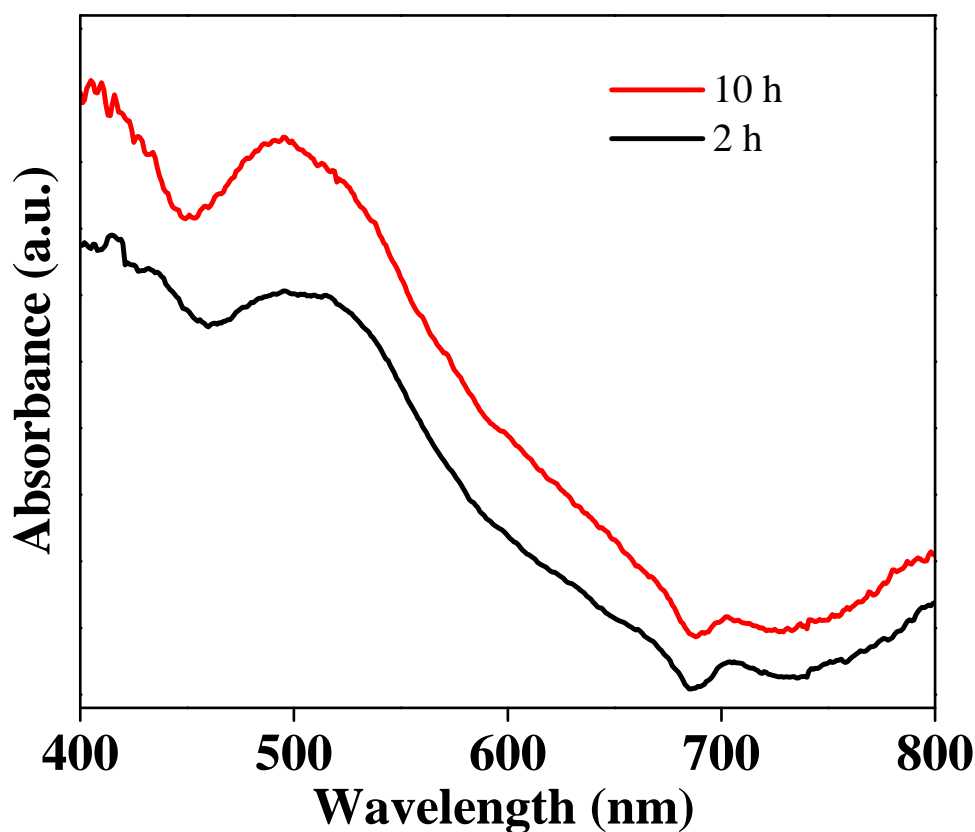


*Fig. 3.10: UV-vis absorption spectra for the dye adsorbed TiO<sub>2</sub> photoanode grown on FTO substrate for 2 and 10 h of hydrothermal reaction.*

The photocurrent density ( $J_{SC}$ ) of the double layer titania NWs grown on FTO after 10 h reaction increased from 5.39 to 7.85 mA cm<sup>-2</sup> compare to 2 h of growth, whereas, there was a very small change in the open-circuit voltage ( $V_{OC}$ ) from 0.68 to 0.64V, as the conduction band edge position will remain unaltered (Fig.3.11) . The fill factor and the photon to electron conversion efficiency of the 10 h sample were increased from 0.53 to 0.65 and from 2.3 to 2.9%, respectively. The enhanced photon conversion efficiency of the 3D-TMSAs grown on FTO substrate for 10 h is due to the increase in photocurrent density, attributed to the

augment in surface, are leading to more dye adsorption. The efficiency of the cells can be improved further, by treating the cells either with  $\text{TiCl}_4$  or  $\text{NbCl}_5$ .

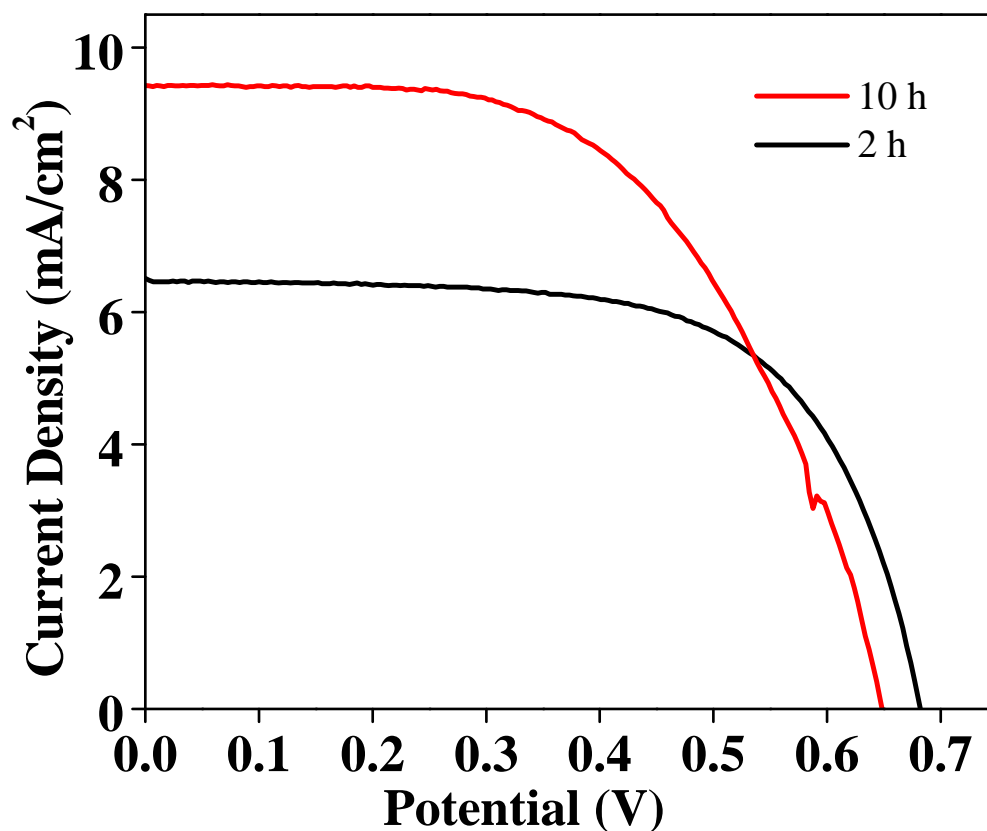


*Fig. 3.11: Current density vs. potential curves for dye sensitized solar cell fabricated from  $\text{TiO}_2$  grown on FTO substrate for 2 and 10 h of hydrothermal reaction.*

### 3.3.7 Photocatalytic property

Titania is an excellent photocatalyst and so, the photocatalytic activity of as-synthesized  $\text{TiO}_2$  was evaluated by measuring the degradation of RhB aqueous solution in sunlight. The sequential degradation of the dye, in presence of  $\text{TiO}_2$  and the change in concentration as a function of irradiation time upto three cycles is represented in Fig. 3.12 (A) and (B) respectively, which showed that without catalyst the concentration of RhB does

not exhibit any significant change for every measurement. From the time-dependent UV–vis spectra it was found that, after 160 min, 74 % of the RhB got degraded. The photocatalyst experiment was performed up to three cycles, to verify the sustainability of the as-grown titania microspheres on FTO. A 4 nm shift of the maximum absorption peak towards lower wavelength from 552 nm to 548 nm was observed due to step by step degradation of RhB. It was found that even in third cycle too, the degradation capability of the catalyst was almost similar of the first cycle (Fig. 3.12 (C)), which proved the reproducibility of the catalytic performance. It is known from literature that photodegradation of RhB follow pseudo first order kinetics according to Langmuir–Hinshelwood (L-H) model, which is well established for heterogenous photocatalyst at low dye concentration.<sup>34</sup> The relevant equation is

$$\ln(C_0/C) = kt$$

where  $C_0$  is the initial concentration of the dye,  $C$  is the concentration of the dye after illumination time  $t$  and  $k$  is the rate constant.<sup>35</sup> From the slope of the graph the  $k$  value for the as-synthesized titania microsphere grown on FTO was found to be .01 min<sup>-1</sup>.( Fig. 3.12 (D))

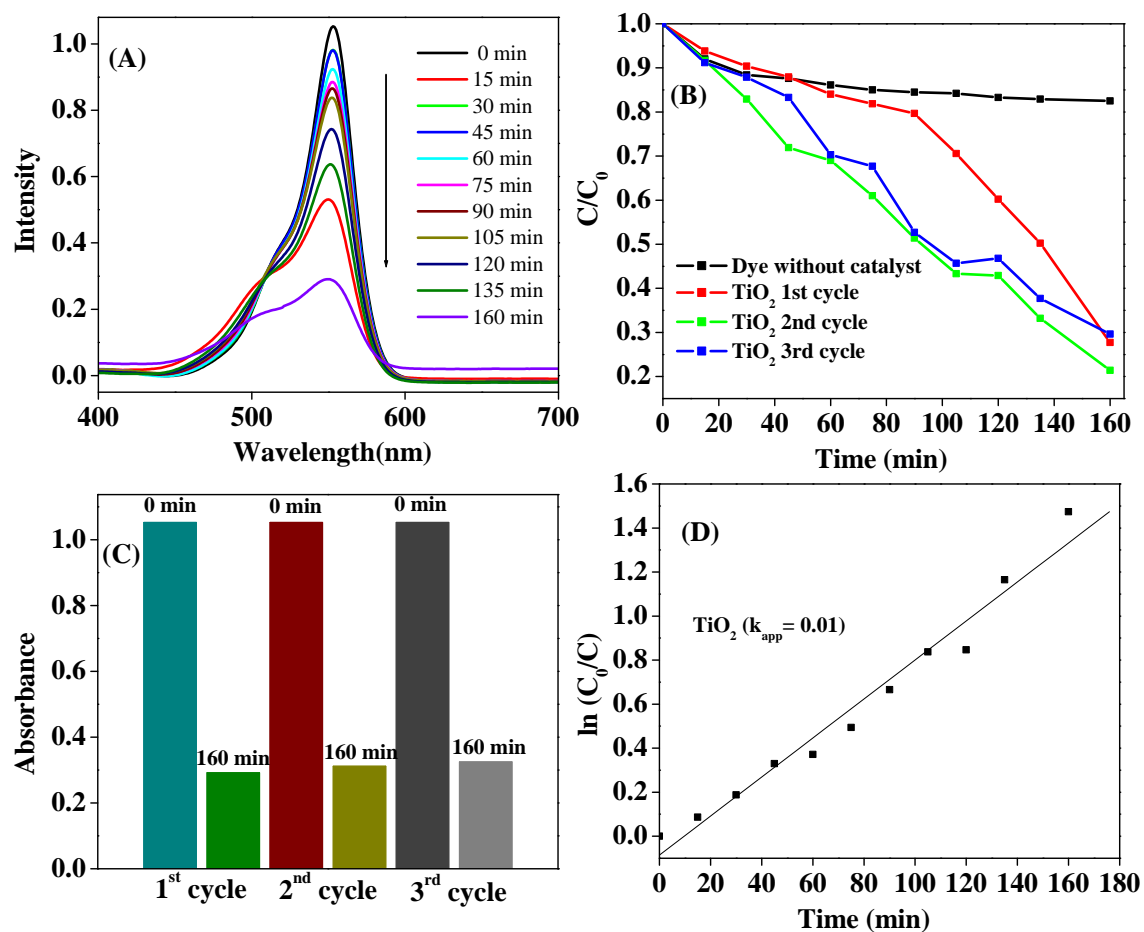


**Fig. 3.12:** (A) UV-vis absorption spectra, (B) photocatalysis degradation profiles of RhB as a function of time in sunlight, (C) Photocatalytic degradation of RhB dye up to three cycles and (D) kinetic plot of photocatalytic degradation.

**3.3.8 Wettability study**

To study the wettability of the as-synthesized film, the contact angle (CA) was measured. The as-grown 3D-TMSAs film on FTO substrate showed superhydrophilicity without UV-irradiation. The water CA of the film with in 2.5 s of dropping of water droplet is  $\sim 7^\circ$ . After that it was not possible to measure the CA as it was extremely small exhibiting superhydrophilic behaviour (Fig.3.13). The combinations of superhydrophilic surface with photocatalytic activity make the titania microsphere film a very good self-cleaning material. Superhydrophilic surfaces can also be used to fabricate antifogging material and in biomolecular immobilization, drag reduction etc.<sup>36</sup> Further, by changing the thickness of the film it can also be used in solar cell as antireflecting coating. The superhydrophilicity of the film without UV radiation, might be caused by the presence of dangling bonds and high concentration of oxygen vacancies.<sup>37</sup> The roughness of the films is also known to increase the wettability.

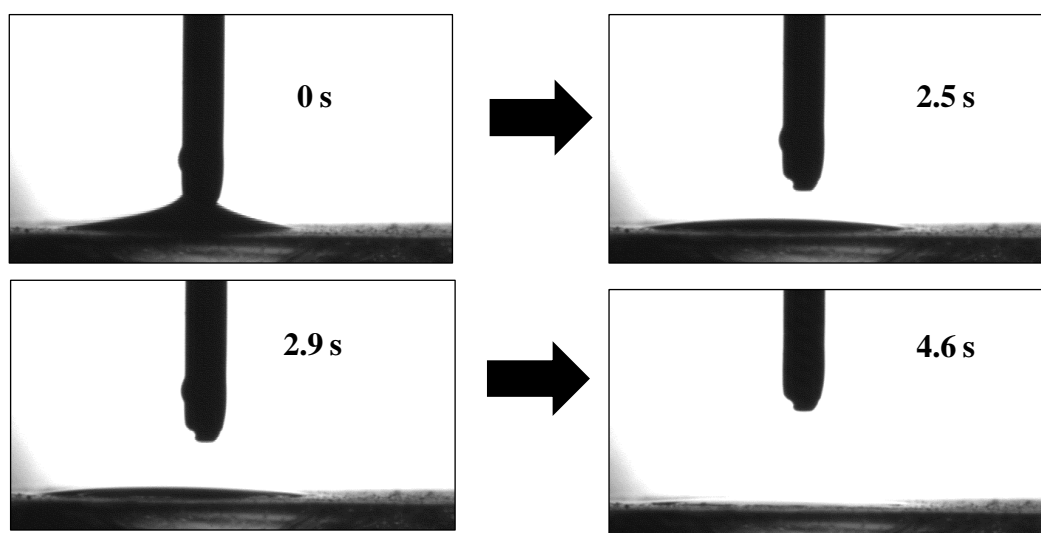


*Fig. 3.13: Water contact angle measurement of TiO<sub>2</sub> microspheres grown on FTO substrate after 10 h of hydrothermal reaction.*

### 3.3.9 Dielectric property

Among simple binary oxides, rutile phase  $\text{TiO}_2$  is massively used as gate insulator and capacitive energy storage, for its high permittivity among all simple oxides and low dielectric loss. The as-synthesized microsphere, consisted of bunches of aligned 1D NWs having boundary nanoscale cavities and surface defect dipoles, favours high dielectric properties. Fig.3.14 showed the room temperature dielectric permittivity and loss tangent of  $\text{TiO}_2$  microsphere grown on FTO substrates for 10 h as a function of frequency. These  $\text{TiO}_2$  nanoflowers show permittivity value of 80 at 10 Hz with a dissipation factor of  $\tan \delta = 0.4$ . These microspheres can be used to confine multiple polarons for designing and fabricating better storage device.<sup>38</sup>

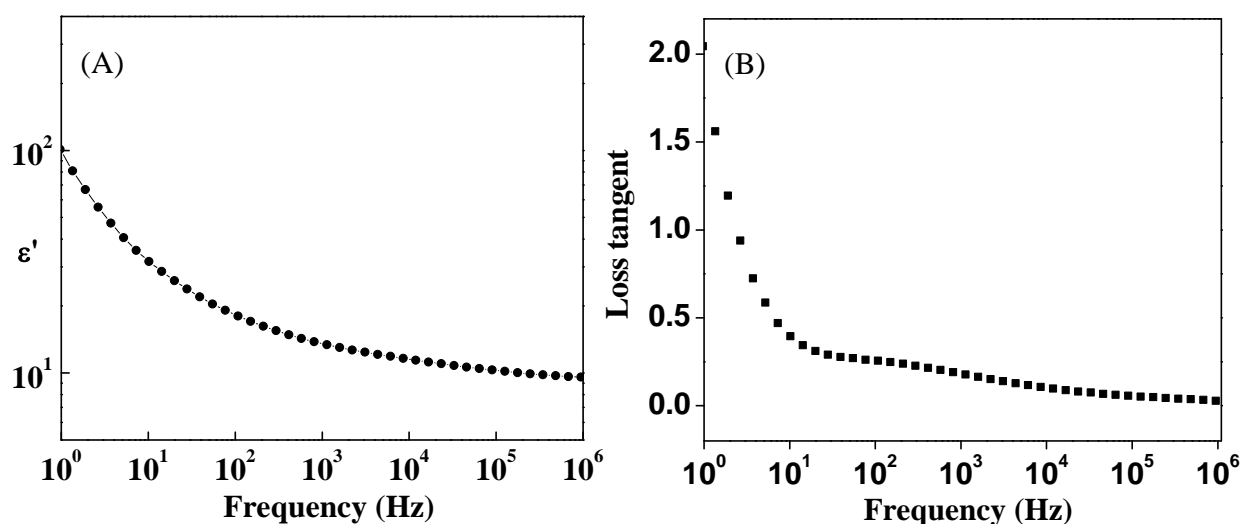


**Fig. 3.14:** Room temperature dielectric permittivity and (B) loss tangent as a function of frequency for as-prepared  $\text{TiO}_2$  microspheres grown on FTO substrate after 10 h of hydrothermal treatment.

### 3.4 Conclusion

In summary, we have grown superhydrophilic 3D rutile titania microspheres, assembling bunches of single-crystalline NWs directly on FTO substrates. To know the plausible growth mechanism, the effects of time and precursor on the formation of the microsphere have been studied thoroughly. After investigating the optical properties of the as-synthesized microspheres, it was found that the microspheres grown on FTO substrate after 10 h of hydrothermal reaction, showed better optical properties due to the presence of double layer of titania nanowires having outward growth which favor effective light scattering and harvesting of photon. This facile, one step, template free low temperature method for synthesis of rutile TiO<sub>2</sub> microspheres, have huge applications in photocatalyst as well as in photovoltaic solar cell. The microsphere film showed superhydrophilicity prior to any UV irradiation. The as-synthesized microsphere on FTO for 10 h showed significant improve of photo conversion efficiency (45 %) due to the synergistic effect of higher surface area and scattering layer compare to 2 h growth. This current one pot surfactant free, synthesis method can also be used for synthesis of various size and shaped metal oxide structure by controlling the various reaction parameters. Moreover, due to simple synthetic method, low cost industrial scale synthesis can also be achieved by following this elegant path to fabricate rutile TiO<sub>2</sub> microsphere. The as-synthesized microspheres have remarkable possibility for exploit not only in photovoltaics or photocatalysis but also in hydrogen storage, lithium ion batteries, photonic crystals, self-cleaning membranes and designing optoelectronics devices.

### 3.5 References

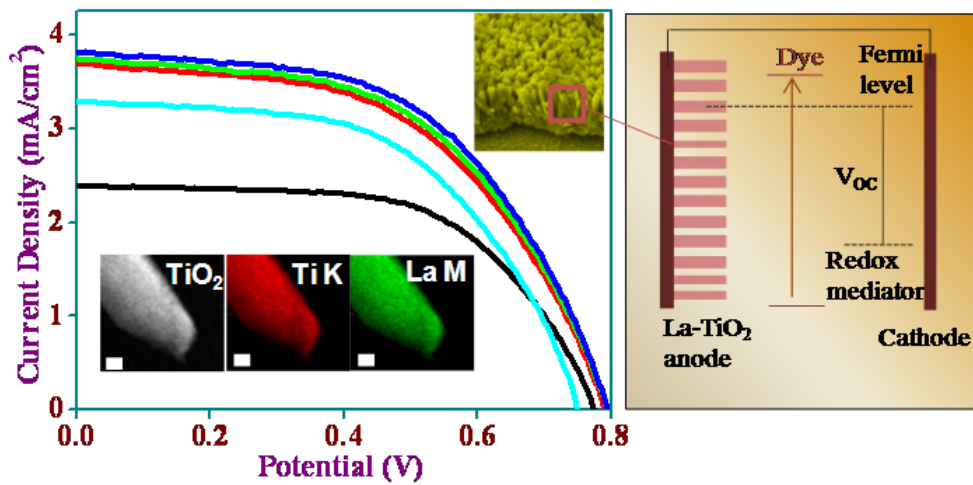
1. W. Zhou, X. Liu, J. Cui, D. Liu, J. Li, H. Jiang, J. Wang and H. Liu, *CrystEngComm*, 2011, **13**, 4557-4563.
2. A. Fujishima and K. Honda, *Nature*, 1972, **238**, 37-38.
3. A. R. Armstrong, G. Armstrong, J. Canales, R. Garcia and P. G. Bruce, *Adv.Mater.*, 2005, **17**, 862-865.
4. J. Bang and P. Kamat, *Adv. Funct. Mater.*, 2010, **20**, 1970–1976.
5. H. Wang, Y. Bai, H. Zhang, Z. Zhang, J. Li and L. Guo, *J. Phys. Chem. C*, 2010, **114**, 16451–16455.
6. S. Sadhu, A. Jaiswal, S. Adyanthaya and P. Poddar, *RSC Adv.* 2013, **3**, 1933-1940.
7. J. H. Braun, A. Baidins and R. E. Marganski, *Prog. Org. Coat.*, 1992, **20**, 105-138.
8. G. Pfaff and P. Reynders, *Chem. Rev.*, 1999, **99**, 1963-1981.
9. R. Zallen and M. P. Moret, *Solid State Commun.*, 2006, **137**, 154-157.
10. Z. B. Zhang, C. C. Wang, R. Zakaria and J. Y. Ying, *J. Phys. Chem. B*, 1998, **102**, 10871-10878.
11. B. Oregan and M. Gratzel, *Nature*, 1991, **353**, 737-740.
12. Y. Y. Zhang, X. Y. Ma, P. L. Chen, D. S. Li and D. R. Yang, *Appl.Phys. Lett.*, 2009, **94**, 1125-1127
13. K. D. Benkstein and S. Semancik, *Sens. Actuators, B, Chemical*, 2006, **113**, 445-453.
14. X. Zhang, H. Kono, Z. Liu, S. Nishimoto, D. A. Tryk, Taketoshi Murakami, H. Sakai, M. Abeb, and A. Fujishima, *Chem. Commun.*, 2007, 4949–4951.
15. E. Hosono, H. Matsuda, I. Honma, M. Ichihara, and H. Zhou, *Langmuir*, 2007, **23**, 7447-7450.

16. J. Yu, T. Ma, and S. Liu, *Phys. Chem. Chem. Phys.*, 2011, **13**, 3491-3501.
17. Y. Sang, B. Geng, and J. Yang, *Nanoscale*, 2010, **2**, 2109-2113.
18. X. J. Feng, K. Shankar, O. K. Varghese, M. Paulose, T. J. Latempa and C. A. Grimes, *Nano Letters*, 2008, **8**, 3781-3786;
19. B. Liu and E. S. Aydil, *J. Am. Chem. Soc.*, 2009, **131**, 3985-3990.
20. Z. Liu, X. Su, G. Hou, S. Bi, Z. Xiao, and H. Jia, *Nanoscale*, 2013, **5**, 8177-8183.
21. M. Ye, H. Liu, C. Lin, and Z. Lin, *Small*, 2013, **9**, 312-321
22. W. Hu, L. Li, W. Tong, and G. Li, *Chem. Commun.*, 2010, 46, 3113-3115
23. B. Liu and, E. S. Aydil, *Chem. Commun.* 2011, 47, 9507-9509.
24. J. Liquiang, S. Xiaojun, X. Baifu, W. Baiqi, C. Weimin and F. Honggang, *J. Solid State Chem.*, 2004, **177**, 3375-3382.
25. L. Yang, Y. Zhang, W. Ruan, B. Zhao, W. Xu and J. Lombardi, *J. Raman Spectrosc.*, 2010, **41**, 721-726.
26. S. Sadhu and P. Poddar, *RSC Adv.*, 2013, **3**, 10363-10369.
27. J. M. Wu, H. C. Shih and W. T. Wu, *Nanotechnology*, 2006, **17**, 105-109.
28. R. Naphade, M. Tathavadekar, J. Jog, S. Agarkar, and S. Ogale, *J. Mater. Chem. A*, 2014, **2**, 975-984.
29. Y. Zhang, C. X. Harris, P. Wallenmeyer, J. Murowchick, and X. Chen, *J. Phys. Chem. C*, 2013, **117**, 24015-24022.
30. S. Ameen, M. S. Akhtar, Y. S. Kim, and H. S. Shin, *RSC Adv.*, 2012, **2**, 4807-4813.
31. H. Cheng, J. Ma, Z. Zhao, and L. Qi, *Chem. Mater.*, 1995, **7**, 663-671.
32. J. Yu, J. Fan and B. Cheng, *J. of. power. Sources.*, 2011, **196**, 7891-7898.
33. S. Sadhu and P. Poddar, *J. Phys. Chem. C*, **DOI**: 10.1021/jp5023983.
34. D. Sarkar, C. K. Ghosh, S. Mukherjee, and K. K. Chattopadhyay *ACS Appl. Mater. Interfaces*, **2013**, *5* (2), pp 331-337.

35. C. Hazra, T. Samanta, A. V. Asaithambi and V. Mahalingam. *Dalton Trans.*, 2014, **43**, 6623–6630.
36. L. Zhang, N. Zhao , and J. Xu, *J. Adh. Sci. technol.*, 28: 8-9 769-790.
37. Y. Han, G. Wu, M. Wang, and H. Chen, *Nanotechnology*, 2009, **20**, 235605 (6pp).
38. W. Hu, L. Li, W. Tong, G. Li, and T. Wan, *J. Mater. Chem.*, 2010, **20**, 8659-8667.

## Chapter IV

**Study the growth mechanism and optoelectronic properties of La-doped TiO<sub>2</sub> nanorods for enhanced photoelectrochemical activity**



### Outline

-----

Fabrication of single crystalline, oriented 1D rods or wires of titania on TCO substrates have enormous significance in the area of photoelectrochemical research owing to their unique optoelectronic properties. It is possible to modify the electrical conductivity and optoelectronic properties of titania by intentionally inclusion of atomic impurity in the material. Here, we have doped lanthanum homogeneously in TiO<sub>2</sub> NR arrays. The homogeneous distribution of lanthanum in titania lattice is confirmed by STEM elemental mapping and line scanning analysis. After doping with lanthanum, there is a negative shift of the flat-band potential of the TiO<sub>2</sub> NRs and the charge carrier density of the NRs is also improved. The energy-conversion efficiency of a DSSC based on 4 mol% La-doped NRs is increased about 21 % compared with undoped one.

-----

### 4.1 Introduction

Oriented one dimensional metal oxide structures directly grown on substrates are of substantial interest due to their widespread application in fuel cell, Li-ion batteries, photoelectrochemical water splitting, solar cell etc.<sup>1-5</sup> These NRs or NTs based electrodes have been developed for various optoelectronic applications due to large aspect ratio and reduced grain boundary which favor efficient transport of charge carriers. By introducing doping impurities in the lattice structure, electrical and magnetic properties of these materials can be altered and manipulated. Doping is routinely performed in bulk semiconductors as well as nanoscale materials.<sup>6-7</sup> Due to typical electronic configuration of  $Ti^{4+}$  ions in  $TiO_2$ , it is possible to alter its optoelectronic properties by preferential doping with *s*, *p*, *d*, or *f* block elements. Thus, incorporation of atomic impurity in titania can tailor the band gap and electrical conductivity of the material.<sup>8</sup> Usually, 1D NRs are synthesized in non-equilibrium condition. Various high temperature methods are used for this purpose. But it is very difficult to homogeneously dope any 1D structure. At high growth temperature, homogeneous doping is really a hard job. In contrast, low temperature solvothermal method is useful for synthesis of doped nanostructures. The direct growth of single crystalline  $TiO_2$  NRs on FTO coated glass substrate by hydrothermal and solvothermal method was first reported a few years ago<sup>9-10</sup> followed by a general method to synthesize  $TiO_2$  rods on various substrates.<sup>5,11-12</sup> The growth mechanism and dependence of morphology of titania NRs on the surface chemistry of substrates have also been studied.<sup>5</sup> The same method is useful for direct synthesis of homogeneously doped NRs on substrates. Due to the low synthesis temperature, the physical properties of the substrates will also remain unaffected. It is reported that doping of lanthanum in titania lattice can increase the oxygen vacancies of titania surface.<sup>13</sup> In DSSC the carboxylic group of the dye molecule is attached with titanium ion. More oxygen vacancy

on the surface can lead to more dye adsorption which can enhance the photovoltaic performance of the cell. Here, we have doped various amount of lanthanum homogeneously in TiO<sub>2</sub> NR arrays directly grown on FTO substrates. The homogeneous distribution of lanthanum in titania lattice is confirmed by STEM elemental mapping and line scanning analysis. The optical characteristics of the as-synthesized NRs have been thoroughly studied through various experiments like UV–visible-DRS, photoluminescence and Raman spectroscopy. The change of flat-band potential ( $V_{FB}$ ) and carrier density of the NRNRs with doping has also been calculated through Mott-Schottky measurements. The photon to electron conversion efficiency of these La-doped TiO<sub>2</sub> NRs has also been measured after adsorbing the NRs in dye and fabricating DSSCs where these dye adsorbed NRs were used as photoanode.

## 4.2 Materials and method

### 4.2.1 Synthesis of TiO<sub>2</sub> and La-doped TiO<sub>2</sub> NRs on FTO substrates

La-doped and undoped TiO<sub>2</sub> NRNRs were synthesized on polycrystalline FTO (sheet resistance = 8 ohm/square) coated glass substrates through solvothermal chemistry. For doped one, Ti(OBu)<sub>4</sub> (purity ≥ 97%, Aldrich Co.) and lanthanum(III) nitrate hexahydrate (La(NO<sub>3</sub>)<sub>3</sub>·6H<sub>2</sub>O) (Purity 99.99% Aldrich Co.) were used as precursors. In a typical synthesis process, first the substrates were ultrasonically cleaned in a mixed solution of DI water, acetone and isopropanol and then dried in N<sub>2</sub> flow. 30 mL H<sub>2</sub>O and 30 mL concentrated HCl (35%) was stirred for 10 min in a 100 mL Teflon vessel followed by the drop-wise addition of 1 mL Ti(OBu)<sub>4</sub> and various amount of La(NO<sub>3</sub>)<sub>3</sub>·6H<sub>2</sub>O solution (1, 2, 3 and 4 mol% with respect to molar concentration of Ti(OBu)<sub>4</sub>) and stirring for another 10 min at RT. The substrates were placed horizontally within the Teflon vessel and the vessel was loaded inside a 100 mL autoclave for the hydrothermal reaction at 150 °C for 20 h in a furnace. After

synthesis, the autoclave was cooled to RT and the substrates were washed vigorously with deionised water and then dried in air.

### 4.2.2 Fabrication of DSSC

To fabricate a solar cell, at first, the as-synthesized doped and undoped TiO<sub>2</sub> NRs on FTO substrates were annealed in air at 400 °C for 30 min. Then it was cooled to 80 °C and was immersed in a 0.5 mM ethanolic solution of N-719 dye (as-received from Solaronix Co.) for 24 h in order to enable sufficient adsorption of the dye which will act as the sensitizer in the presence of light. After completing the adsorption of the dye the substrate was washed very carefully with ethanol and dried for 1 h. After that, a platinum coated FTO substrate which is used as the counter electrode was placed above the dye adsorbed FTO substrate and an electrolyte containing 0.6 M 1-hexyl-2-3-dimethylimidazolium iodide, 0.1 M LiI, 0.05 M I<sub>2</sub> and 0.5 M 4-tert-butylpyridine in methoxyacetonitrile was injected into the space between the anode and the cathode to complete the assembly of the DSSC.

### 4.2.3 Characterization techniques

In order to confirm the crystalline phase of TiO<sub>2</sub> NRs, XRD study was performed using a PANalytical X'PERT PRO instrument and the iron-filtered Cu-K<sub>α</sub> radiation ( $\lambda = 1.5406 \text{ \AA}$ ) in the  $2\theta$  range of 10 - 80° with a step size of 0.02°. To analyze the shape and size of the synthesized NRs scanning electron microscopy (FEI Quanta 200 environmental scanning microscope) and HRTEM were done. Optical properties of the as-synthesized TiO<sub>2</sub> NRs were investigated by UV-visible spectrophotometer. UV-vis-DRS spectroscopy measurements were performed on a Jasco UV-vis-NIR (Model V570) dual beam spectrometer operated at a resolution of 2 nm. PL spectra were acquired using a Fluorolog Horiba Jobin Yvon fluorescence spectrophotometer, equipped with a 400 W Xe lamp as an

excitation source and a Hamamatsu R928 photomultiplier tube (PMT) as a detector. Raman spectroscopy measurements were recorded at room temperature on an HR 800 Raman spectrophotometer (Jobin Yvon, Horiba, France) using monochromatic radiation emitted by a He-Ne laser (633 nm), operating at 20 mW. Mott- Schottky measurements were obtained in 3M KCl solution at 298 K at frequency 10 KHz using a Solartron S1287 Electrochemical Interface and 1255B Frequency Response Analyzer (Solartron Analytical, UK). Current-voltage characteristics were calculated by irradiated the cell with  $100 \text{ mW/cm}^2$  (450 W xenon lamp, Oriel instrument), 1 sun AM 1.5 G filter was used to simulate the solar spectrum. The active area of the cell was  $0.5 \text{ cm}^2$ . The photocurrent was measured by using a Keithley 2400 source.

### 4.3 Results and discussion

#### 4.3.1 X-Ray diffraction study

In order to confirm the crystalline phase of La-doped  $\text{TiO}_2$  NRs, XRD study was done. From the XRD, it is confirmed that the different mol% La-doped  $\text{TiO}_2$  NRs grown on FTO substrates are in rutile phase. In Fig.4.1, the XRD patterns of various amounts of La-doped and undoped  $\text{TiO}_2$  NRs synthesized on FTO coated glass substrates, FTO coated glass substrate and PDF file # 21-1276 have been compared.

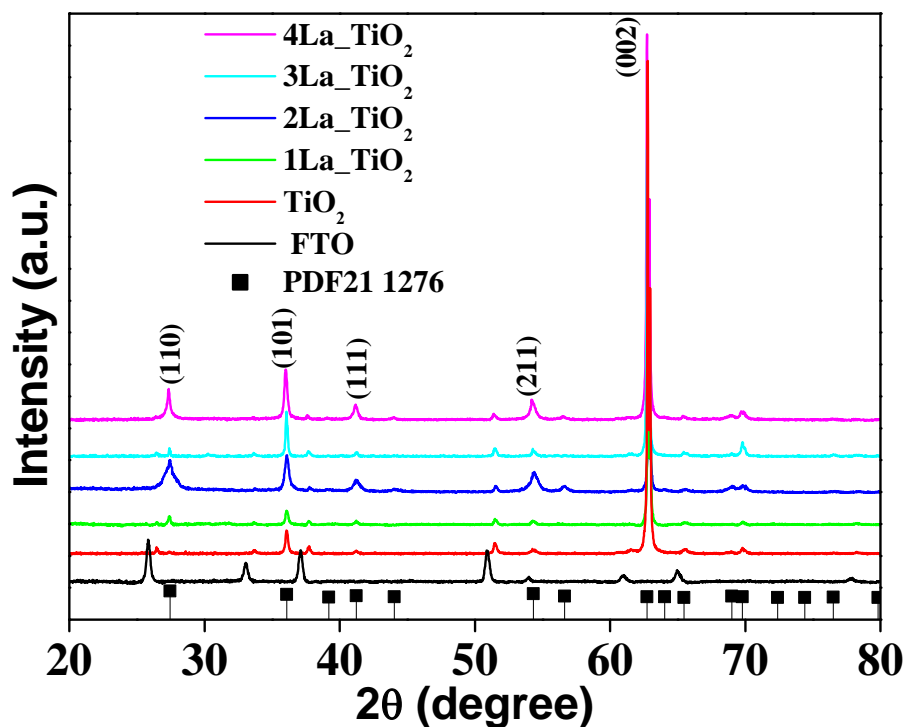


**Fig. 4.1:** XRD patterns of pure  $\text{TiO}_2$  and  $\text{La}$ -doped  $\text{TiO}_2$  NRs with various amounts of doping. 1La\_ $\text{TiO}_2$ , 2La\_ $\text{TiO}_2$ , 3La\_ $\text{TiO}_2$  and 4La\_ $\text{TiO}_2$  denote the samples where the added amount of  $\text{La}(\text{NO}_3)_3 \cdot 6\text{H}_2\text{O}$  was 1, 2, 3 and 4 mol% with respect to molar concentration of  $\text{Ti}(\text{OBU})_4$ .

It is clear from the diffraction peaks that the NRs are highly oriented with respect to the substrate along the (002) plane. If the intensity of the (002) peak is compared with the standard  $\text{TiO}_2$  data (PDF data file #21-1276), it is found that the relative intensity of (002) peak is increased  $\sim 10$  times from  $\sim 10\%$  to 100%. From XRD pattern, it is confirmed that almost no peak-shift takes place as the amount of doping is very little. Thus, the presence of impurity phases such as  $\text{La}_2\text{O}_3$  or  $\text{La}_2\text{Ti}_2\text{O}_7$  can be ruled-out which can be further proved from Raman and TEM analysis. As the size of  $\text{La}^{3+}$  (0.115 nm) ion is larger than  $\text{Ti}^{4+}$  (0.068 nm) ion so, it is quite difficult for  $\text{La}^{3+}$  ions to enter into the lattice structure of  $\text{TiO}_2$ . So, here the probability of formation of structural defect is less and for that reason lattice parameter of

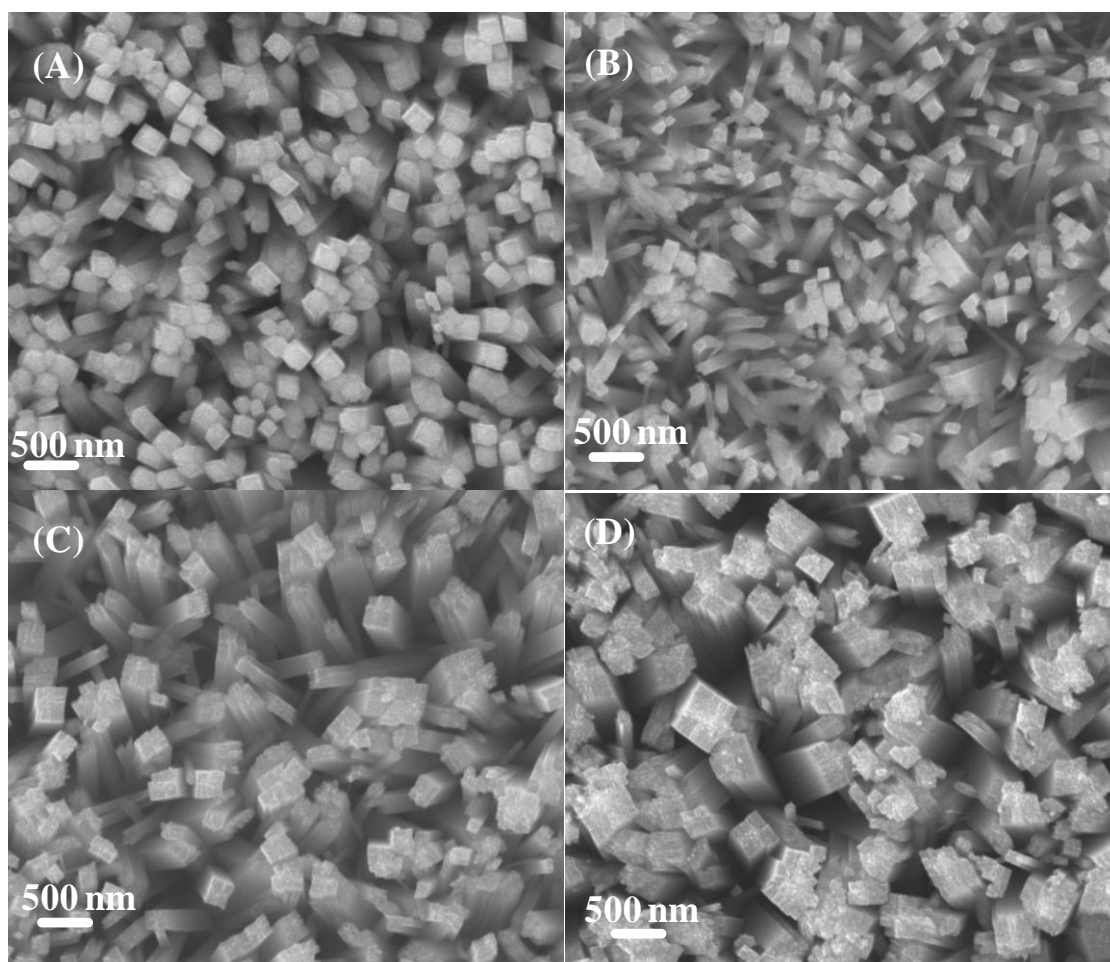
doped TiO<sub>2</sub> NRs will not change and almost no distortion will take place. So from the XRD pattern it can be confirmed that the lattice parameters of the TiO<sub>2</sub> NRs remain unchanged after doping with lanthanum due to mismatch of ionic radius.

### 4.3.2 Determination of shape and size

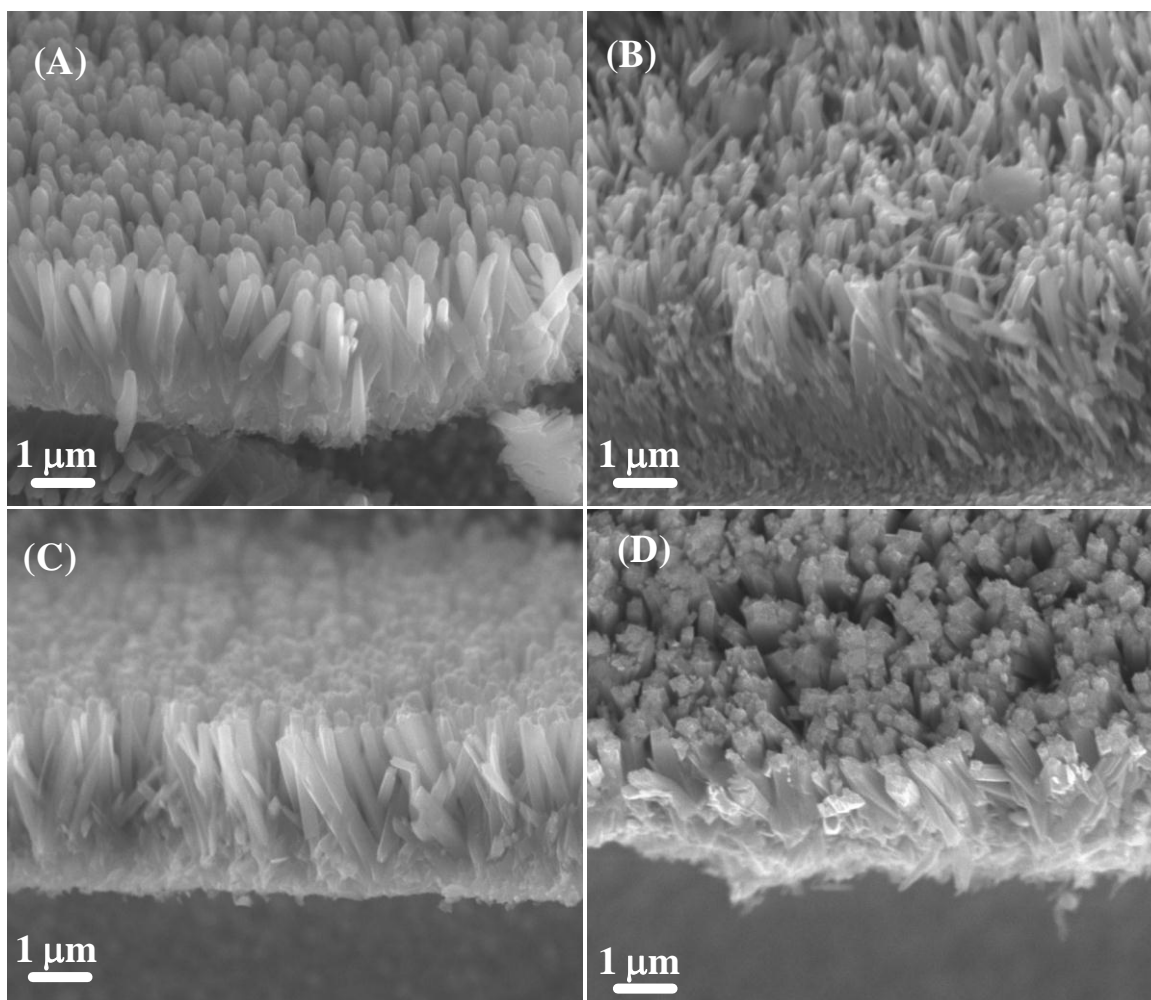
#### 4.3.2.1 SEM analysis

Fig.4.2 and Fig.4.3 represent the top and cross sectional view SEM images of various amounts of La-doped TiO<sub>2</sub> NRs grown on FTO substrates respectively. From the images it is confirmed that the NRs are densely packed and perfectly oriented in the out-of-plane direction with respect to FTO. The substrates are evenly covered by the NRs. It is cleared from the figure, that the top facets of the rods are square shaped which also supports the expected growth habit of tetragonal crystal. From the horizontal and cross sectional view of the images it is seen that the top surface of the as-synthesized rods are quite rough but the side walls of the NRs are relatively smooth. A closer look of the images also exposed that the NRs are consisted of a number of thinner nanowires. It is found that with increase in the amount of lanthanum dopant the density of the NR arrays decreased gradually.

The average diameter, length and density of the as-grown NR arrays have been determined from the SEM images. The results are summarized in Table 4.1. From earlier report it was found that La-dopant can inhibit the growth of TiO<sub>2</sub> nanocrystals.<sup>14</sup> So, it can be assumed that as the amount of dopant concentration is increased in the growth solution, the nucleation density of the seed layer is decreased slowly and thus the compactness of the rods, grown on FTO substrates was minimized. Further, from EDX analysis the chemical stoichiometry of the TiO<sub>2</sub> NRs was estimated and the calculated data is shown in Table 4.2.



*Fig. 4.2: SEM images of (A) 1 (B) 2 (C) 3 and 4 mol % (D) La-doped TiO<sub>2</sub> NRs grown on FTO coated glass substrates (top view).*



*Fig. 4.3: SEM images of (A) 1 (B) 2 (C) 3 and 4 mol % (D) La-doped TiO<sub>2</sub> NRs grown on FTO coated glass substrates (cross-sectional view).*

**Table 4.1.** Structural properties of La-doped TiO<sub>2</sub> NRs grown on FTO substrate

| <b>Samples</b>        | <b>NR average diameter (nm)</b> | <b>NR average length (nm)</b> | <b>NR average density (<math>\mu\text{m}^{-2}</math>)</b> |
|-----------------------|---------------------------------|-------------------------------|---|
| 1La -TiO <sub>2</sub> | 199                             | 2.2                           | 12  |
| 2La -TiO <sub>2</sub> | 131                             | 2.3                           | 9   |
| 3La -TiO <sub>2</sub> | 271                             | 2.4                           | 6   |
| 4La -TiO <sub>2</sub> | 400                             | 2.2                           | 2   |

**Table 4.2.** EDX Analysis

| <b>Samples</b>        | <b>Lanthanum content (atomic %)</b> |
|-----------------------|-------------------------------------|
| 1La -TiO <sub>2</sub> | 0.93                                |
| 2La -TiO <sub>2</sub> | 1.37                                |
| 3La -TiO <sub>2</sub> | 2.21                                |
| 4La -TiO <sub>2</sub> | 3.78                                |

### 4.3.2.2 TEM analysis

In order to study the formation and composition of the NRs in detail further, structural characterization was carried out through transmission electron microscope. Fig.4.4 shows the TEM and HRTEM images of an individual representative 2 mol% La-doped TiO<sub>2</sub> NR grown on FTO substrate. In Fig.4.4 (C) lattice fringes with interplanar spacing  $d_{101} = 0.24$  nm corresponding to the rutile phase of titania can be identified clearly. No core/shell type structure was seen. Sharp and clean selected area electron diffraction pattern (SAED) for the NR grown on FTO substrate (Fig.4.4 (B)) was visualized nicely along  $[1\bar{1}0]$  zone axis, which was the inveterate evidence of the single crystallinity of the NRs. The fast Fourier transform (FFT) pattern (Fig.4.4 (D)) of the high-resolution phase contrast image (Fig.4.4(C)) also confirms the single crystallinity of the NRs. In Fig.4.4 (E) the reciprocal lattice points not corresponding to the c-plane were removed to further analyze the lattice structure. The remaining lattice points and the inverse FFT (IFFT) image were shown in Fig.4.4 (E) and 4.4 (F) respectively. The IFFT image revealed a more clear structure with high crystallinity and minimal distortion.

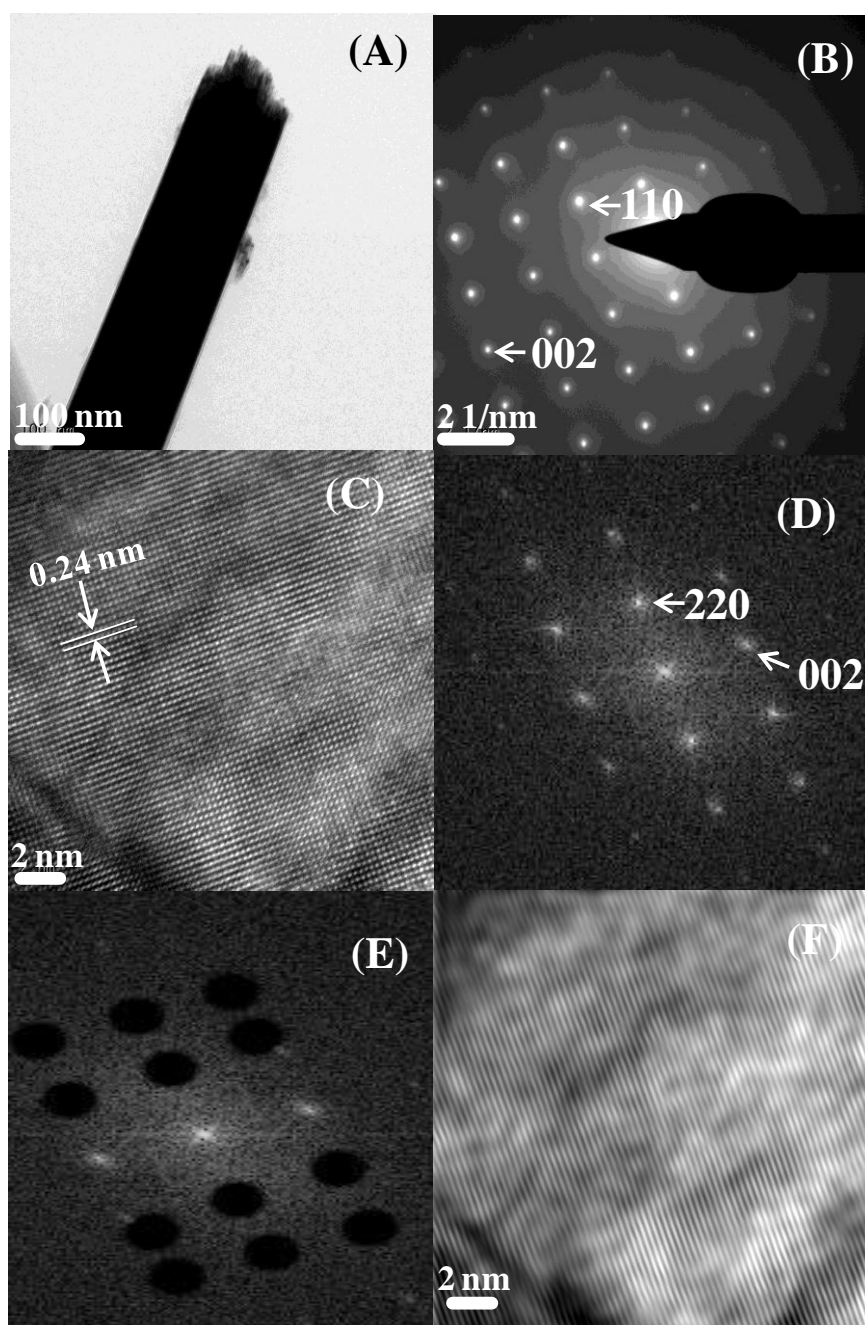


**Fig. 4.4:** (A) TEM image and (B) selected area electron diffraction pattern of 2 mol% La-doped single  $\text{TiO}_2$  NR grown on FTO coated glass substrate. (C) HRTEM image of the NR. (D) FFT pattern of the NR. (E) Reciprocal lattice points not corresponding to the  $c$ -plane has been removed. (F) Results of IFFT based on the lattice points shown in (E).

### 4.3.2.3 STEM analysis

STEM elemental mapping was done in order to inspect the distribution of lanthanum in the NRs. In this technique, a two dimensional map of the samples can be visualized nicely where the relative location of individual element of a particular material can be spotted. Here, through color intensity the relative amount of the element present can be judged. Fig.4.5 showed the STEM image of 2 mol% La-doped TiO<sub>2</sub> NR and corresponding elemental mapping of the as-synthesized NR. In this figure, the dark field image of an individual NR and the elemental maps of Ti-K and La-M are shown. The dark field image of the NR provides a reference to locate the particles in the elemental map. From the elemental mapping it was confirmed that lanthanum was distributed homogeneously throughout the rods. Thus from STEM and line scanning analysis (Fig.4.5 (D)) it can be proved that the as-synthesized TiO<sub>2</sub> NRs were homogeneously doped with lanthanum and no secondary phase was present.

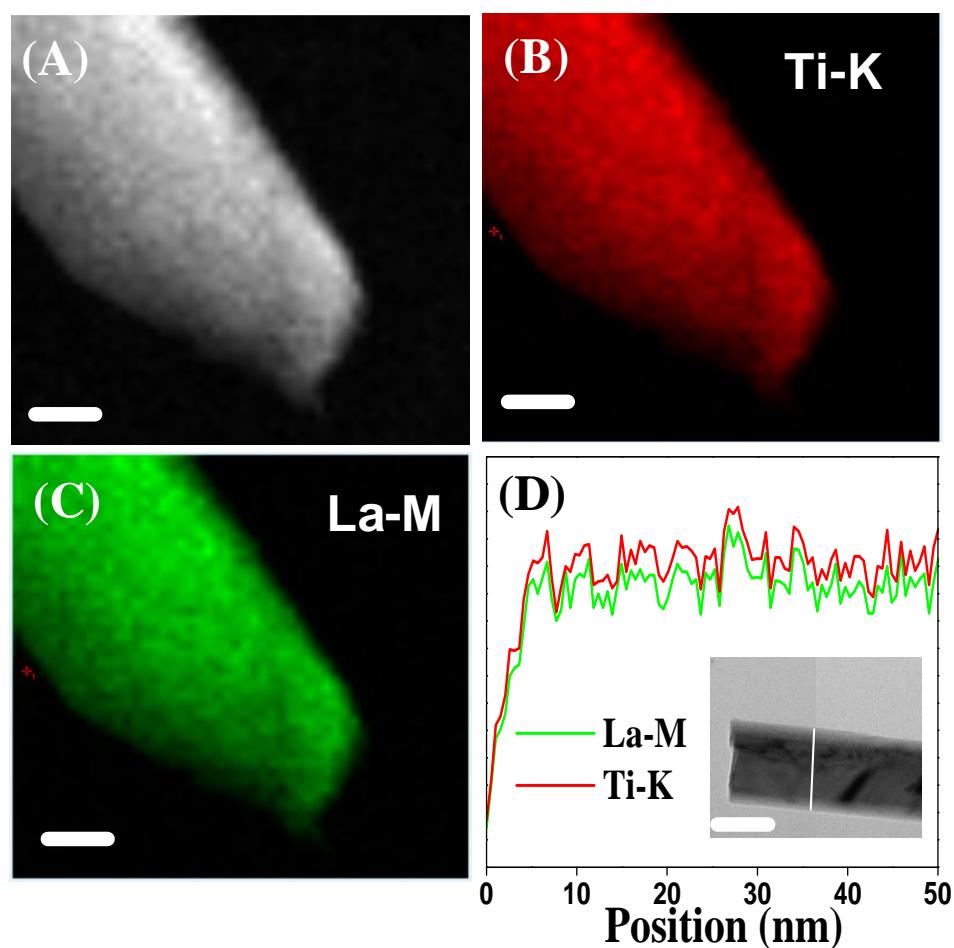


**Fig. 4.5:** (A) STEM image of a representative 2 mol % La-doped  $\text{TiO}_2$  NR. (B, C) The corresponding elemental mapping of (B) Ti-K (C) La-M (100 nm scale bar for all). (D) Line scanning analysis across the single NR indicated by the line as shown in the inset (scale bar 50 nm).

### 4.3.3 Optical properties

#### 4.3.3.1 UV-vis-DRS spectra

In order to study the effect of La-doping on the optical properties of  $\text{TiO}_2$  NRs the UV-vis-DRS spectra of the doped and undoped NRs was measured. All the samples showed sharp absorption edge around  $\sim 420$  nm ( $E_{\text{bg}} \sim 3.0$  eV). It is found that the shape of the curve remained almost unchanged but with doping, the amount of absorption increased (Fig.4.6A).

As discussed earlier, due to huge size difference of  $\text{La}^{3+}$  and  $\text{Ti}^{4+}$  ions it is difficult to incorporate  $\text{La}^{3+}$  ions in  $\text{TiO}_2$  lattice and that is the main reason for not changing the absorption curve shape with doping. The increase in absorption may be due to the presence of surface state caused by oxygen vacancy.<sup>15-16</sup> All the doped and undoped samples exhibited broad absorption below 420 nm. This can be due to interband electron transition of the rutile  $\text{TiO}_2$  at its band gap energy *i.e.* around 3 eV. The tail around 420-500 nm can be attributed to the surface states.<sup>16</sup> Thus, it can be said that lanthanum doping did not give rise to any new spectral phenomena. Assuming that the rutile  $\text{TiO}_2$  NRs possess a direct transition, the band edge energy of the as-synthesized NRs are calculated by plotting  $(\alpha h\nu)^2$  against  $h\nu$  (where  $\alpha$  is absorption coefficient and  $h\nu$  is photon energy). After calculating the band gap from the intercepts (Fig.4.6B) it is found that with doping a little amount of red shift take place from 3.0 eV to 2.9 eV.

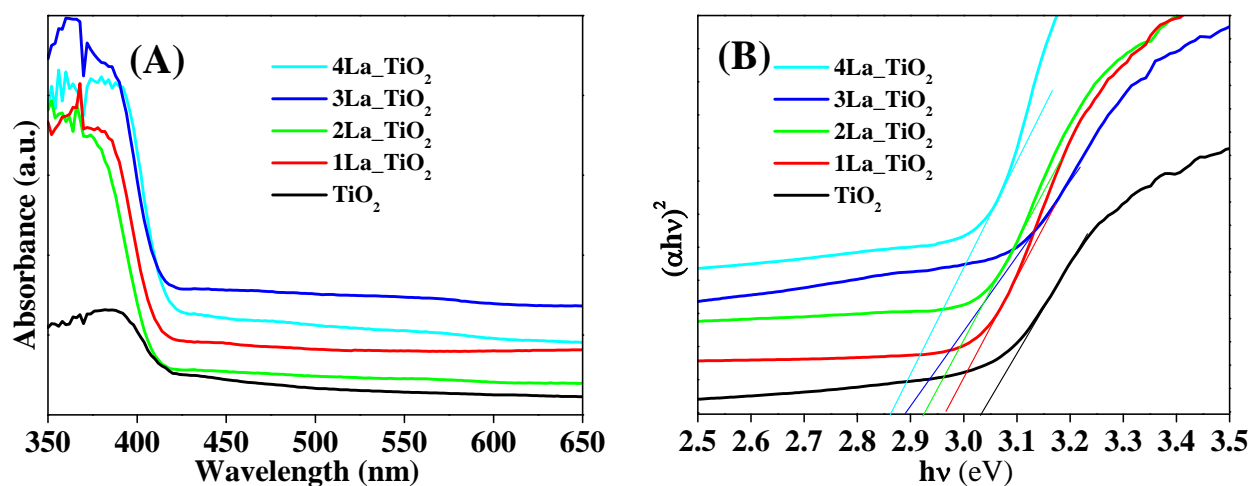


**Fig. 4.6 :** (A) UV-visible DRS spectra, (B) the dependence of the absorption coefficient as a function of energy plot for pure  $\text{TiO}_2$  and La-doped  $\text{TiO}_2$  NRs with various amounts of doping.

### 4.3.3.2 Photoluminescence study

Fig.4.7 shows the photoluminescence property of the as-synthesized doped and undoped TiO<sub>2</sub> NRs grown on FTO. It is known that if stable chemical state of dopant has half-filled or full-filled outer electron configuration then normally it will not generate a different PL phenomena as it is unable to capture electrons.<sup>17</sup> So it is found that TiO<sub>2</sub> and La-doped TiO<sub>2</sub> exhibit similar type of PL signals with no difference in curve shape. The doped and undoped NRs show strong and wide PL signal at a range from 400 to 500 nm at 380 nm excitation wavelength. The reason behind this wide range of PL emission may be attributed to binding excitons.<sup>14-15</sup> The peak around ~415 nm (~ 2.98 eV) is due to band-band emission of rutile TiO<sub>2</sub> NRs as the photoexcited electrons radiatively return back from conduction band to valence band.<sup>20</sup> The peak around 464 nm is the characteristic peak of rutile TiO<sub>2</sub>.<sup>18</sup> This peak is due to metal-ligand charge transfer transition from Ti<sup>4+</sup> to oxygen anions in TiO<sub>6</sub><sup>8-</sup> complex. Although the doped and undoped sample exhibit almost similar type of curve shape but the PL intensity of the peaks can be heavily influenced as a result of the change in surface structure of the material due to alternation of oxygen vacancy.<sup>17,19</sup> It is found that the PL intensity increased gradually as the amount of La-dopant increased. This trend is followed till the amount of La content is 3 mol%. But after that, the intensity of the PL peaks decrease as the amount of dopant increases. The decrease in PL intensity can be due to the presence of large number of Ti-O-La bonds which can decrease the content of surface oxygen vacancy. Moreover the effective area of TiO<sub>2</sub> for absorbing light can be less.<sup>14</sup>

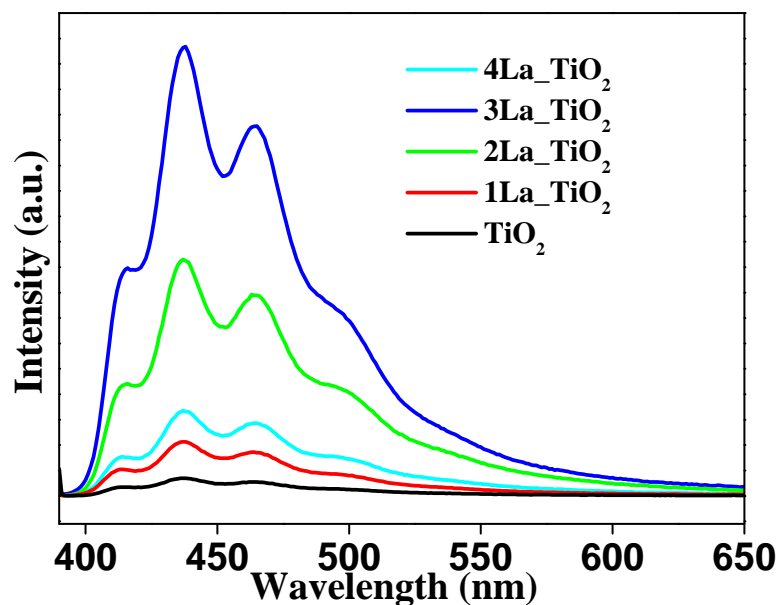
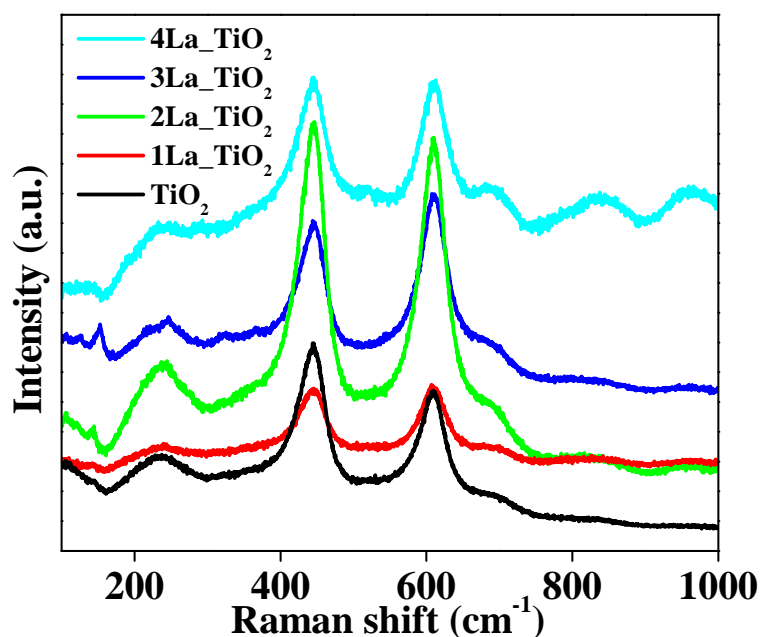


Fig. 4.7 : PL spectra, for pure  $\text{TiO}_2$  and La-doped  $\text{TiO}_2$  NRs with various amounts of doping.

#### 4.3.3.3 Raman study

Fig.4.8 shows the Raman spectra of  $\text{TiO}_2$  and La-doped  $\text{TiO}_2$  NRs at room temperature. In both pure and doped samples the characteristic peaks for rutile  $\text{TiO}_2$  nanocrystals were found which again supports the formation of rutile structure. The two Raman active fundamental modes,  $E_g$  ( $\sim 444 \text{ cm}^{-1}$ ) and  $A_{1g}$  ( $\sim 610 \text{ cm}^{-1}$ ) and the second order effect at  $\sim 244 \text{ cm}^{-1}$  due to multiple phonon vibration of  $B_{1g}$  mode can be clearly distinguished.<sup>19-20</sup> It is found that in La-doped sample the principle peak at  $444 \text{ cm}^{-1}$  gradually shifted to higher frequency ( $448 \text{ cm}^{-1}$ ) up to 3 mol% and then again a slight red shift takes place at 4 mol% ( $442 \text{ cm}^{-1}$ ). This peak shift can be a cause to an increase in oxygen vacancy which can also be proved from PL spectra.<sup>19</sup> It also indicates that the Ti-O bond is slightly shorter and stronger due to bond contraction in case of lanthanum doping. No peak of La-O is seen in the spectra

which supports the XRD result. It can be due to interstitial doping of lanthanum. For that reason La is incorporated in the interstitial site of  $\text{TiO}_2$  lattice.



*Fig. 4.8: Raman spectra, for pure  $\text{TiO}_2$  and La-doped  $\text{TiO}_2$  NRs with various amounts of doping.*

### 4.3.4 Electrochemical study

Electrochemical impedance measurement was done to study the role of La-doping on the transport properties of the NRs. Fig.4.9 shows the Mott-Schottky plot of  $\text{TiO}_2$ , 2 and 3 mol% La-doped  $\text{TiO}_2$  NRs. All the samples show a positive slope which is the property of the n-type semiconductor.<sup>22</sup> Compared to  $\text{TiO}_2$  NRs, the doped one showed smaller slopes which indicate that charge carrier density increases with doping. The flat-band potential ( $V_{\text{FB}}$ ) and carrier density of the doped and undoped NRs were calculated from Mott-Schottky equation.

$$\frac{1}{C^2} = \left( \frac{2}{e_0 \epsilon \epsilon_0 N_d} \right) \left[ (V - V_{FB}) - \frac{kT}{e_0} \right]$$

where  $e_0$  is the fundamental charge constant,  $\epsilon$  the dielectric constant of  $\text{TiO}_2$ ,  $\epsilon_0$  is the permittivity of vacuum,  $N_d$  the donor density,  $V$  the electrode applied potential,  $V_{FB}$  the flat-band potential and  $kT/e_0$  is a temperature-dependent correction term. It was found from calculation that with increase in doping concentration donor density increases. The calculated results are shown in Table 4.3. As no evidence of core/shell structure was found from TEM and STEM analysis so the possibility of carrier concentration gradient can be ruled-out.

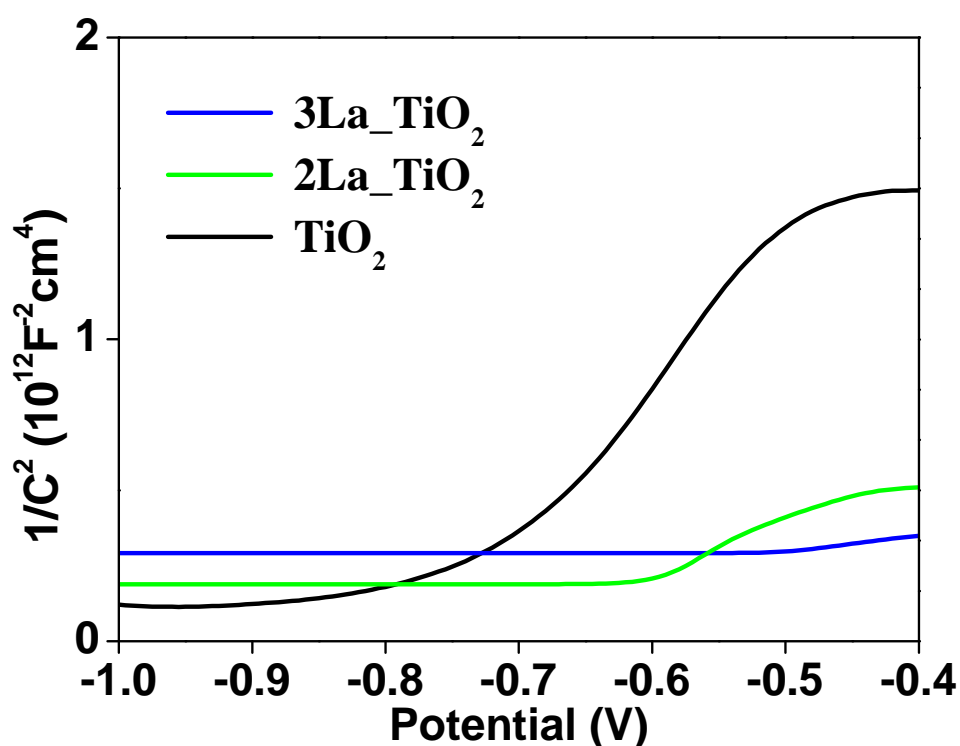


*Fig. 4.9: Mott-Schottky plots measured at a frequency of 10 kHz at 298 K in 3M KCl solution for  $\text{TiO}_2$  and 2 and 3 mol% La-doped  $\text{TiO}_2$  NRs.*

**Table 4.3.** Flat band potential ( $V_{FB}$ ) and donor density ( $N_d$ ) Of  $TiO_2$  and La-doped  $TiO_2$  NR

| Samples      | $V_{FB}$ (V) | $N_d$ ( $10^{18}$ ) $cm^{-3}$ |
|--------------|--------------|-------------------------------|
| $TiO_2$      | -0.532       | 0.56                          |
| 1La_ $TiO_2$ | -0.615       | 1.39                          |
| 2La_ $TiO_2$ | -0.735       | 6.41                          |
| 3La_ $TiO_2$ | -0.832       | 8.73                          |
| 4La_ $TiO_2$ | -0.862       | 8.75                          |

### 4.3.5 Photovoltaic property

These single-crystalline, oriented NRs grown on FTO substrates can effectively act as photoanode in DSSC. Due to the single crystalline structures of these NRs, rapid and efficient transfer of electrons takes place from the sensitizer to collecting conducting substrate. Moreover, as the NRs are directly synthesized on the transparent substrate, so more incident light can be passed through the backside of the photoelectrode and hence able to generate more photoelectrons. Fig.4.10 showed the current density-voltage curves of the assembled solar cell under  $100\text{ mW/cm}^2$  illumination. The average performance characteristics of the cells in terms of short-circuit photocurrent density ( $J_{SC}$ ), open-circuit voltage ( $V_{OC}$ ), fill factor (FF) and photoelectric conversion efficiency ( $\eta$ ) are summarized in Table 3.4. It is found that with doping,  $V_{OC}$  value increases from 0.704 V to 0.749 V. The increase in open circuit voltage is due to the elevation of flat band potential as conduction band edge of the doped  $TiO_2$  NRs is shifted towards more negative potential.

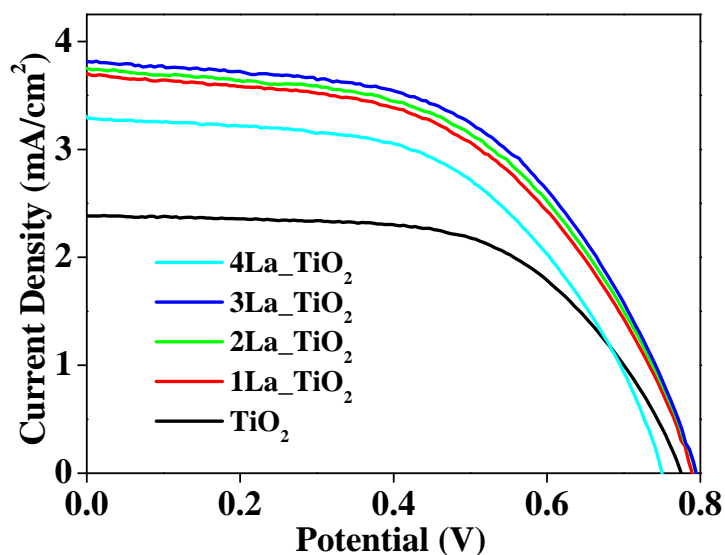


**Fig. 4.10:** Current density vs. potential curves for dye sensitized solar cell fabricated from pure  $\text{TiO}_2$  and La-doped  $\text{TiO}_2$  NRs grown on FTO glass substrates.

**Table 4.4.** Photovoltaic Properties of DSSCs Assembled with  $\text{TiO}_2$  and La-doped  $\text{TiO}_2$  NRs

| Samples             | $J_{\text{SC}}$ ( $\text{mA cm}^{-2}$ ) | $V_{\text{OC}}$ (V) | FF (%) | $\eta$ (%) |
|---------------------|---|---------------------|--------|------------|
| $\text{TiO}_2$      | 2.38                                    | 0.704               | 60.48  | 1.39       |
| 1La_ $\text{TiO}_2$ | 3.69                                    | 0.789               | 52.95  | 1.54       |
| 2La_ $\text{TiO}_2$ | 3.74                                    | 0.793               | 53.48  | 1.58       |
| 3La_ $\text{TiO}_2$ | 3.81                                    | 0.794               | 54.29  | 1.64       |
| 4La_ $\text{TiO}_2$ | 3.28                                    | 0.749               | 55.22  | 1.69       |

### 4.4 Conclusion

In summary, single crystalline oriented La-doped TiO<sub>2</sub> NRs have been synthesized on FTO substrates. Homogeneous doping of lanthanum throughout the NRs has been proved by STEM analysis. Detailed optical studies of the as synthesized doped and undoped NRs have been done through UV, PL and Raman spectroscopy. Electrochemical impedance measurement was done to investigate the band edge position and to know the trend of electron carrier density in the doped NRs. The La-doped TiO<sub>2</sub> NRs have been successfully used as photoanode in DSSC. Photon to electron power conversion efficiency was increased 21% after doping the TiO<sub>2</sub> NRs with 4 mol% lanthanum. This simple hydrothermal synthesis method can be applied considerably to homogeneously dope any metal cations with titanium ion. Systematic investigation of doping of metal cations with Ti<sup>4+</sup> ions for synthesis of homogeneously doped single crystalline NRs directly grown on substrate will provide valuable information for designing high-performance photoelectrochemical device.

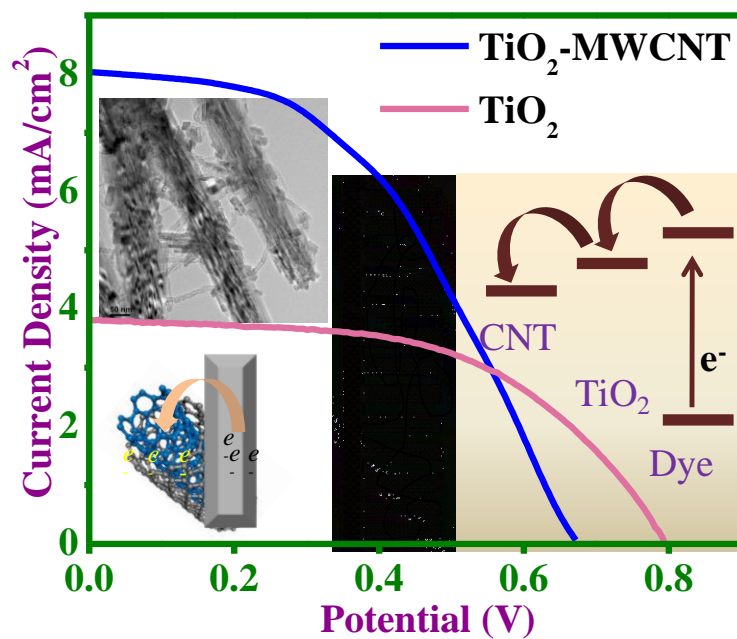
### 4.5 References:

1. M. Yang, B. Ding, S. Lee and J. Lee, *J. Phys. Chem. C*, 2011, **115**, 14534–14541.
2. L. Wang, Z. Xue, X. Liua and B. Liu, *RSC Adv.*, 2012, **2**, 7656–7659.
3. J. Bang and P. Kamat, *Adv. Funct. Mater.*, 2010, **20**, 1970–1976.
4. H. Wang, Y. Bai, H. Zhang, Z. Zhang, J. Li and L. Guo, *J. Phys. Chem. C*, 2010, **114**, 16451–16455.
5. S. Sadhu, A. Jaiswal, S. Adyanthaya and P. Poddar, *RSC Adv.* 2013, **3**, 1933-1940.
6. A. K. Chandiran, F. Sauvage, L. Etgar and M. Graetzel, *J. Phys. Chem. C*, 2011, **115**, 9232-9240.
7. H. Zhu, J. TaO and X. Dong, *J. Phys. Chem. C*, 2010, **114**, 2873-2879.
8. X. Feng, K. Shankar, M. Paulose and C. Grimes, *Angew. Chem*, 2009, **48**, 8095-8098.
9. X. J. Feng, K. Shankar, O. K. Varghese, M. Paulose, T. J. Latempa and C. A. Grimes, *Nano Lett.*, 2008, **8**, 3781-3786.
10. B. Liu and E. S. Aydil, *J. Am. Chem. Soc.*, 2009, **131**, 3985-3990.
11. A. Kumar, A. R. Madaria and C. W. Zhou, *J. Phys. Chem. C*, 2010, **114**, 7787-7792.
12. H. E. Wang, Z. H. Chen, Y. H. Leung, C. Y. Luan, C. P. Liu, Y. B. Tang, C. Yan, W. J. Zhang, J. A. Zapien, I. Bello and S. T. Lee, *Appl. Phys. Lett.*, 2010, **96**, 263104-1-3.
13. J. Zhang, Z. Zhao, X. Wang, T. Yu, J. Guan, Z. Yu, Z. Li and Z. Zou, *J. Phys. Chem. C*, 2010, **114**, 18396-18400.
14. J. Liquiang, S. Xiaojun, X. Baifu, W. Baiqi, C. Weimin and F. Honggang, *J. Solid State Chem.*, 2004, **177**, 3375-3382.
15. L. Yang, Y. Zhang, W. Ruan, B. Zhao, W. Xu and J. Lombardi, *J. Raman Spectrosc.*, 2010, **41**, 721-726.

- 16.. H. Wu, L. Deng, S. Wang, B. Zhu, W. Huang, S. Wu, S. Zhang, *J. Dispersion Sci. Technol.*, 2010, **31**, 1311-1316.
17. J. Liqiang, Q. Yichun, W. Baiqi, L. Shudan, J. Baojiang, Y. Libin, F. Wei, F. Honggang, and S. Jiazhong, *Sol. Energy Mater. Sol. Cells*, 2006, **90**, 1773-1787.
18. W. Zhou, X. Liu, J. Cui, D. Liu, J. Li, H. Jiang, J. Wang and H. Liu, *CrystEngComm*, 2011, **13**, 4557-4563.
19. Y. HuO, J. Zhu, J. Li, G. Li and H. Li, *Journal of Molecular Catalysis*, 2007, **278**, 237- 243.
20. Z. Sun, J. Kim, Y. Zhao, F. Bijarbooneh, V. Malgars, Y. Lee, Y. Kang and S. Dou, *J. Am. Chem. Soc.*, 2011, **133**, 19314-19317.
21. S. Amin, A. Nicholls and T. Xu, *Nanotechnology*, 2007, **18**, 445609 (5pp).
22. M. Xu, P. Da, H. Wu, D. Zhao and G. Zheng, *Nano Lett.*, 2012, **12**, 1503-1508.

## Chapter V

**In situ synthesis of one dimensional  $\text{TiO}_2$  – MWCNT  
nanocomposites and study their optoelectronic properties for  
photovoltaic applications**



### Outline

-----

Template-free synthesis of phase-pure, 1D, single-crystalline, rutile titania NRs or NWs at low temperature, still remains a challenging task due to its complex nature of surface chemistry. In these 1D structures, charge transport is highly favored. To further modify the electrical conductivity and optoelectronic properties of these 1D nanostructures, various methods such as doping of TiO<sub>2</sub> with metal and non-metal, synthesis of branched and hybrid structures are developed. If these hybrid structures can be directly synthesized on substrate, the transport of electron will improve due to reduce grain boundary and exciton recombination. We have developed a method of simultaneous, one-step synthesis of 1D-rutile TiO<sub>2</sub>-multiwalled carbon nanotube (MWCNT) composite film directly grown on FTO substrate along-with 1D-rutile TiO<sub>2</sub>-MWCNT composite powder. The as-grown NR films were single-crystalline and oriented vertically with respect to the substrate, having average height of ~ 2 μm. The well-connected network of TiO<sub>2</sub> with MWCNTs was observed through electron microscopy. The composite film shows positive movement of the flat-band edge and an increase in the charge carrier density. The TiO<sub>2</sub>-MWCNT composite was successfully used as photoanode in a DSSC and exhibits a 60 % increase in energy-conversion efficiency compared with only TiO<sub>2</sub> NRs.

-----

### 5.1 Introduction

Template free synthesis of phase pure, 1D, single-crystalline rutile titania NRs or NWs at low temperature, still remains a challenging task due to its complex nature of surface chemistry. In these 1D structures charge transport is highly favored. To further modify the electrical conductivity and optoelectronic properties of these 1D-structures, various methods such as doping of TiO<sub>2</sub> with metals and non-metals, synthesis of branched and hybrid structures are developed.<sup>1-3</sup> Carbon nanotubes (CNT) are used as semiconductor support due to their unique electrical and electronic properties and wide electrochemically stable window. Kongakanad *et al.* fabricated SWCNT on conducting carbon fiber and glass electrode in order to disperse TiO<sub>2</sub> NPs in NW network and thus to improve the photoelectrochemical performance.<sup>4</sup> Later, they also explained the mechanism of superior photon harvesting ability of SWCNT through electron charging and discharging property.<sup>5</sup> Moreover, CNTs also have high surface area, good adsorption, mechanical and thermal properties.<sup>6</sup> At room temperature, CNT can conduct electrons with almost no electrical resistance.<sup>7</sup> Besides, due to the ease of surface functionalization and superior electronic properties of MWCNTs, the incorporation of MWCNT into TiO<sub>2</sub> has attracted the attention of researchers to fabricate various optoelectronic devices.<sup>8-9</sup> The TiO<sub>2</sub>-MWCNT composites are also supposed to produce synergetic effect between the metal-oxide and MWCNT. Several studies have been done to synthesize and understand the physicochemical properties of TiO<sub>2</sub>-MWCNT nanocomposites. For example, Lee *et al.* have synthesized TiO<sub>2</sub> porous film along with various amount of MWCNT through sol-gel method and they measured charge transport resistance.<sup>8</sup> Peining *et al.* have fabricated rice-grain shaped TiO<sub>2</sub>-CNT nanocomposites by electrospinning and they found ~32% enhancement in the energy conversion efficiency in DSSC.<sup>10</sup>

If these composite structures can be directly synthesized on substrate, the transport of electron will be far better due to reduce grain boundaries and exciton recombination. Transport and recombination studies on the oriented NTs showed smooth charge transport while suppressing

recombination.<sup>11</sup> Here, we have developed a method for the one-step, simultaneous synthesis of 1D-rutile TiO<sub>2</sub>-MWCNT composite film directly grown on FTO substrate along with 1D-rutile TiO<sub>2</sub>-MWCNT composite powder. The as-grown NRs films were single-crystalline and oriented vertically with respect to the substrate, having average length of ~2 μm. The well-connected network of TiO<sub>2</sub> with MWCNT was observed through electron microscopy. The composite film showed positive movement of the flat-band edge and an increase in charge carrier density. The TiO<sub>2</sub>-MWCNT composite was successfully used as photoanode in a DSSC and it exhibits a 60 % increase in energy-conversion efficiency compared with only TiO<sub>2</sub> nanorods.

## 5.2 Materials and method

### 5.2.1 Materials

All the chemicals were of analytical grade and used as-received without any further purification, unless otherwise described. Titanium butoxide (TBOT) (purity ≥ 97%) and carboxylic acid functionalized MWCNT (average diameter and length ~9.5 nm and ~1.5 μm respectively) were purchased from Aldrich Co. FTO (fluorine doped tin oxide, sheet resistance = 8 ohm/square) substrate and N-719 dye (cisbis(isothiocyanato)bis(2,2'-bipyridyl-4-4'-dicarboxylato)-ruthenium(II)bis-tetrabutylammonium) were received from Solaronix Co.

### 5.2.2 Synthesis of TiO<sub>2</sub> and TiO<sub>2</sub>- MWCNT composites

TiO<sub>2</sub> NRs and 1D-TiO<sub>2</sub>-MWCNT composites were synthesized through a simple hydrothermal method. First the substrates were ultrasonically cleaned in a mixed solution of deionised water, acetone and isopropanol and then dried in N<sub>2</sub> flow. Thirty milliliter of H<sub>2</sub>O and 30 mL concentrated (35%) HCl were stirred for 10 min in a beaker, followed by the addition of 1 mL titanium butoxide and 5 mg of MWCNTs. The solution was then sonicated for 2 h. After that, the solution was transferred into a 100 mL Teflon vessel; and the substrates were placed horizontally within the Teflon vessel. Then the vessel was loaded inside a 100 mL autoclave and the autoclave was

kept in a furnace at 150 °C for 20 h for hydrothermal reaction. After synthesis, the substrates and the resulted product were washed vigorously with DI water and then dried in air to produce greyish TiO<sub>2</sub>-MWCNT film and powder respectively. The schematic of the synthesis method has been shown in Fig. 5.1. To synthesize TiO<sub>2</sub> NRs, same method was followed without adding MWCNTs.

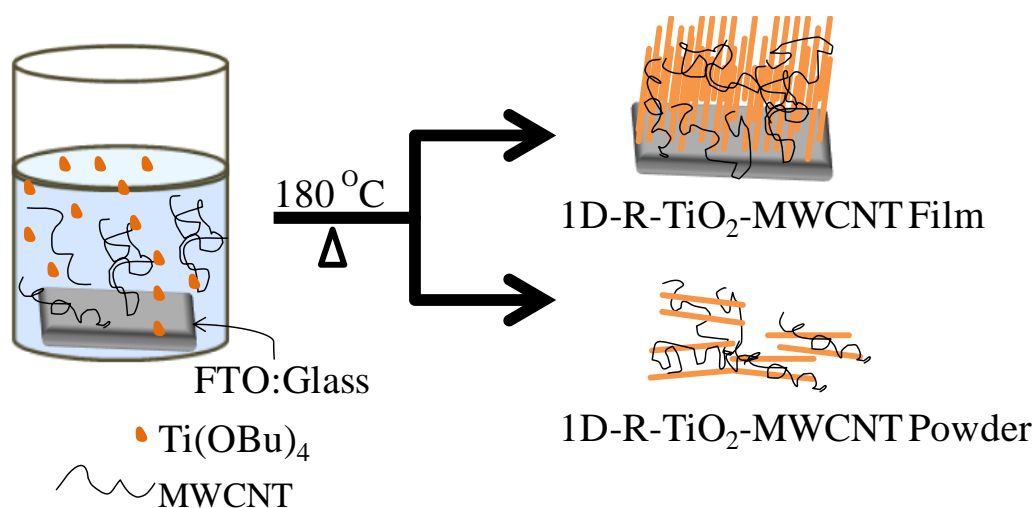


**Fig. 5.1:** Schematic of the simultaneous synthesis of 1D-R-TiO<sub>2</sub>-MWCNT film and 1D-R-TiO<sub>2</sub>-MWCNT powder.

### 5.2.3 Fabrication of DSSC

To fabricate a solar cell, at first, the as-synthesized TiO<sub>2</sub>-MWCNT composite film on FTO substrate was annealed in air at 400 °C for 30 min. Then, it was cooled to 80 °C and was immersed in a 0.5 mM ethanolic solution of N-719 dye for 24 h in order to enable sufficient adsorption of the dye which will act as the sensitizer in the presence of light. After completing the adsorption of the dye, the substrate was washed very carefully with ethanol and dried for 1 h. After that a platinum coated FTO substrate, which will be used as the counter electrode, was placed above the dye-adsorbed FTO substrate and an electrolyte containing 0.6 M 1-hexyl-2-3-dimethylimidazolium iodide, 0.1 M LiI, 0.05 M I<sub>2</sub> and 0.5 M 4-tert-butylpyridine in methoxyacetonitrile was injected into the space between the anode and the cathode to complete the assembly of the DSSC.

### 5.2.4 Characterization techniques

In order to confirm the crystalline phase of TiO<sub>2</sub> nanorods, X-ray diffraction (XRD) study was performed using a PANalytical X'PERT PRO instrument and the iron-filtered Cu- K<sub>α</sub> radiation ( $\lambda = 1.5406 \text{ \AA}$ ) in the  $2\theta$  range of  $10\text{-}80^\circ$  with a step size of  $0.02^\circ$ . To further confirm the crystalline phase and formation of composite material, Raman spectroscopy measurements were recorded at room temperature on an HR 800 Raman spectrophotometer (Jobin Yvon, Horiba, France) using monochromatic radiation (achromatic Czerny-Turner type monochromator with silver treated mirrors) emitted by a He-Ne laser (633 nm), operating at 20 mW and with accuracy in the range between 450 nm and  $850 \text{ nm} \pm 1 \text{ nm}$ , equipped with thermoelectrically cooled (with Peltier junctions), multi-channel, spectroscopic grade charge coupled detector ( $1024 \times 256$  pixels of 26 microns) with dark current lower than  $0.002 \text{ electrons pixel}^{-1} \text{ s}^{-1}$ . An objective of 50 X LD magnification was used both to focus and collect the signal from the samples. X-ray photoelectron spectroscopy (XPS) was done with an ESCALab spectrometer having Al  $k\alpha$  X-ray source ( $h\nu = 1486.6 \text{ eV}$ ) operating at 150 W using a Physical Electronics 04-548 dual Mg/Al anode and in a UHV system with a base pressure of  $\leq 5 \times 10^{-9}$  Torr. Both the incident and take off angles are  $55^\circ$  with respect to the surface normal. The analysis depth was around 10 to 15  $\text{\AA}$ . The spectra were energy-analyzed with an Omicron Nanotechnology EA 125 Hemispherical Energy Analyzer in pulse-count mode with pass energies of 50 eV for broad scan data and 25 eV for specific, narrow-range core-level transitions. The XPS data were curve-resolved using XPSPEAK4.123 after removal of a Shirley background. The curve-resolved spectra were fit with the minimum number of peaks needed to reproduce the spectral features using a Gaussian–Lorentzian product function. In order to study the thermal decomposition profile of the composite, thermogravimetric analysis (TGA) was done using SDT model Q600 of TA Instruments Inc. USA at a heating rate of  $10^\circ\text{C}/\text{m}$  under air flow at  $100 \text{ mL}/\text{m}$ . To analyze the shape and size of the NRs, field emission scanning electron microscopy (FESEM: Hitachi S-4200) was done. The specific structure details and morphology of the nanocomposite particles were obtained by using FEI Tecnai F30 high resolution transmission electron microscope (HRTEM) equipped with a

super-twin lens (s-twin) operated at 300 keV accelerating voltage with Schottky field emitter source with maximum beam current ( $> 100$  nA) and small energy spread (0.8 eV or less). The point-to-point resolution of the microscope is 0.20 nm with a spherical aberration of 1.2 mm and chromatic aberration of 1.4 mm with 70  $\mu\text{m}$  objective aperture size. The powders obtained were dispersed in hexane and then drop-casted on carbon-coated copper TEM grid with 200 mesh and loaded to a single tilt sample holder.

Optical properties of the as-synthesized  $\text{TiO}_2$  composites were investigated by UV-visible spectrophotometer. UV-vis-DRS spectroscopy measurements were performed on a Jasco UV-vis-NIR (Model V570) dual beam spectrometer operated at a resolution of 2 nm. PL spectra were acquired using a Fluorolog Horiba Jobin Yvon fluorescence spectrophotometer, equipped with a 400 W Xe lamp as an excitation source and a Hamamatsu R928 photomultiplier tube (PMT) as a detector. M-S measurements were obtained in 3M KCl solution at 298 K at frequency 10 KHz using a Solartron S1287 Electrochemical Interface and 1255B Frequency Response Analyzer (Solartron Analytical, UK).

Current-voltage characteristics were calculated by irradiating the cell with  $100 \text{ mW/cm}^2$  (450 W xenon lamp, Oriel instrument), 1 sun AM 1.5 G filter was used to simulate the solar spectrum. The active area of the cell was  $0.5 \text{ cm}^2$ . The photocurrent was measured by using a Keithley 2400 source.

## 5.3 Results and discussion

### 5.3.1 XRD analysis

Fig. 5.2 showed the XRD pattern of as-synthesized 1D  $\text{TiO}_2$ -MWCNT nanocomposite film directly grown on FTO substrate and  $\text{TiO}_2$ -MWCNT powders along with FTO substrate, only MWCNT and PDF file # 21-1276 for comparison. From the data, the synthesis of phase pure rutile structure can be confirmed. After analyzing the diffraction pattern, it was also confirmed that the highly oriented, 1D nanocomposite film were directly synthesized on the substrate along the (002) plane as the relative intensity of the (002) peak was enhanced  $\sim 10$  times from  $\sim 10\%$  to  $100\%$  in

comparison with the standard data file (PDF data file # 21-1276). The intensity ratio of ( $I_{002}/I_{110}$ ) for the standard data, the  $\text{TiO}_2$ -MWCNT powder and the  $\text{TiO}_2$ -MWCNT film were 0.1, 0.09 and 5.5 respectively. Further, to confirm the degree of orientation, the texture coefficient (TC) for (002) peak of the oriented nanocomposite film were determined and compared with the TC value of the as-synthesized  $\text{TiO}_2$ -MWCNT powder. The semi-quantitative estimation of the texture can be defined through TC, where

$$TC_{(hkl)} = \frac{I_{(hkl)}/I_{0(hkl)}}{n^{-1} \sum_n I_{(hkl)}/I_{0(hkl)}}$$

$I_{(hkl)}$  is the observe relative peak intensity,  $I_{0(hkl)}$  is the standard intensity of the plane taken from data file,  $n$  is the number of Bragg reflections considered for the sum in the denominator.<sup>12</sup> Deviation of TC values from unity implies preferred growth. A higher value of TC denotes preferred orientation of grains. The calculated  $TC_{(002)}$  values of as-synthesized nanocomposite powder and film were 1.1 and 7.9 respectively. Strong preferential alignment of the as-grown composite film along the [001] direction normal to substrate can be confirmed from the TC value which can be further established from FESEM micrograph. In the  $\text{TiO}_2$ -MWCNT powder, the diffraction peak at  $2\theta = 25.5^\circ$  is

attributable to MWCNT. Due to the higher intensity of (002) peak and presence of less amount of MWCNT, it is very hard to elicit the characteristic peak of the MWCNT in as-synthesized  $\text{TiO}_2$ -MWCNT composite.

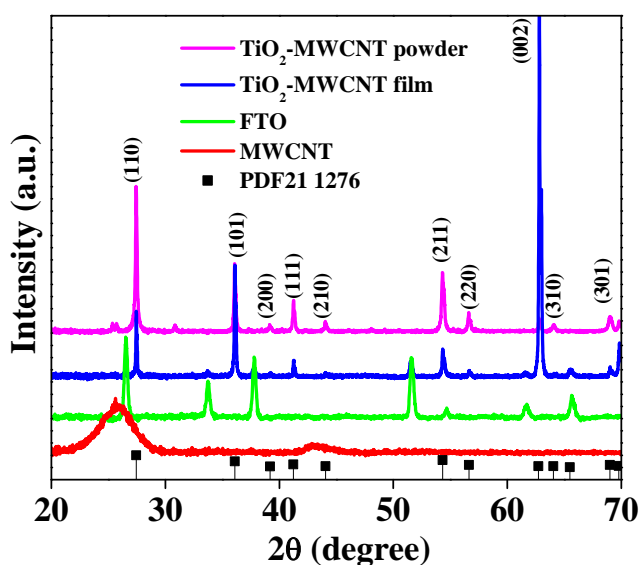


*Fig. 5.2: XRD patterns of 1D rutile  $\text{TiO}_2$ -MWCNT powder and film directly grown on FTO.*

### 5.3.2 Raman study

To further explore the effect of MWCNT loading on the local structure of the as-synthesized rutile  $\text{TiO}_2$  composite, Raman spectroscopy was used to analyze the vibrational properties of the samples. The appearance of two Raman active fundamental modes for characteristic rutile  $\text{TiO}_2$  nanocrystals at  $\sim 444 \text{ cm}^{-1}$  and  $610 \text{ cm}^{-1}$  due to  $E_g$  and  $A_{1g}$  optical phonons respectively can be clearly distinguished in as-synthesized  $\text{TiO}_2$  NRs,  $\text{TiO}_2$ -MWCNT film and  $\text{TiO}_2$ -MWCNT powder (Figs. 5.3 (A), (B), and (D)).<sup>13-14</sup> In addition, two peaks situated at  $\sim 1356$  and  $\sim 1572 \text{ cm}^{-1}$  corresponding to D and G bands of MWCNT can also be noticed in the composite samples which confirm the successful incorporation of MWCNT into  $\text{TiO}_2$  (Figs. 5.3 (A), (B)).<sup>15</sup> The presence of G-band is due to the  $sp^2$ -hybridization originating from in-plane symmetric stretching of C-C bond.<sup>16</sup> The introduction of functionalized hydroxyl groups results into the broadening of D ( $43$  to  $51 \text{ cm}^{-1}$ ) and G ( $57$  to  $65 \text{ cm}^{-1}$ ) bands, respectively. It was also seen that the full width at half maxima (FWHM) of  $E_g$  mode in the nanocomposites varied from  $50$  to  $60 \text{ cm}^{-1}$ . Such broadening of peak was observed due to confinement of optical phonons, oxygen vacancies and surface strain effect due to interface integration.<sup>17</sup>

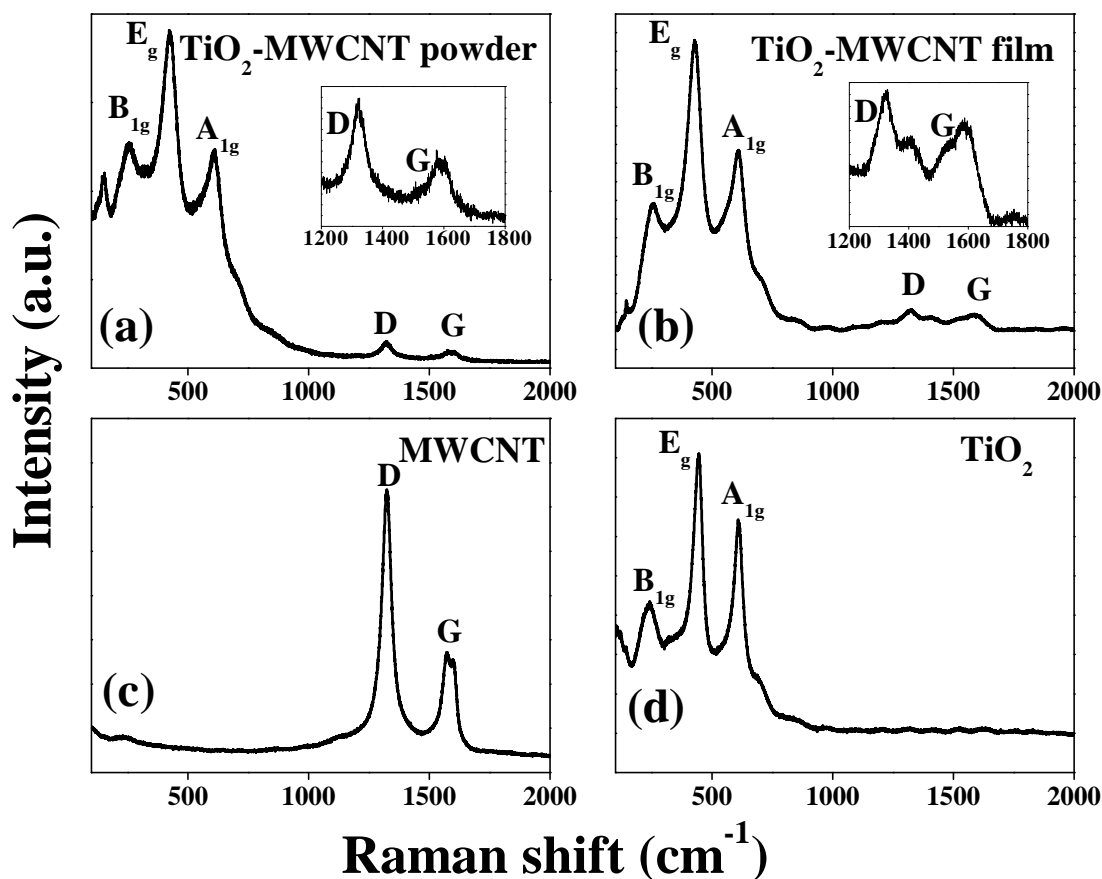


**Fig. 5. 3:** Raman spectra for (A) 1D rutile TiO<sub>2</sub>-MWCNT powder, (B) 1D rutile TiO<sub>2</sub>-MWCNT film directly grown on FTO, (C) MWCNT and (D) rutile TiO<sub>2</sub>.

### 5.3.3 XPS study

XPS study of the as-prepared composite NRs was done in order to know the chemical states of the surface elements. From the survey spectra of the NRs (Fig. 5.4(A)) the characteristics energy peaks of C, O and Ti were detected. By comparing the survey peaks of as-synthesized TiO<sub>2</sub> and TiO<sub>2</sub> - MWCNT composite in Fig. 5.4(A), it was found that the intensity of the carbon peak in the nanocomposite was increased which proves the successful incorporation of MWCNT into TiO<sub>2</sub>. The C 1s core level spectra of the nanocomposite can be deconvulated into two peaks. The main peak at

284.6 eV is due to the presence of  $sp^2$  hybridized C atom and the other peak around 285.8 eV can be assigned to carbon atom bound to oxygen atom.<sup>18</sup> The absence of any peak  $\sim 281$  eV confirms that C-doped  $TiO_2$  has not been formed. The O 1s peak can also be deconvoluted into two peaks. The peak around 530.6 eV is due to the presence of lattice oxygen in  $TiO_2$ .<sup>19</sup> The broad shoulder at 532.2 eV is due to O-C bond.<sup>35</sup> XPS spectrum of Ti 2p shows two peaks at  $\sim 459.2$  and  $\sim 464.9$  eV corresponding to spin-orbital splitting of Ti  $2p_{3/2}$  and Ti  $2p_{1/2}$  respectively, attributed to the presence of  $Ti^{4+}$  in an octahedral environment.<sup>20</sup> The binding energy of Ti is slightly shifted towards higher side than bulk rutile which proves that the atmosphere of the composite material is different from the  $TiO_2$  NRs.<sup>10</sup> No peak around 455 and 456.7 eV due to  $Ti^{2+}$  or  $Ti^{3+}$  states was observed.<sup>21</sup> So, from the XPS peak profile, the absence of impurity phases *e.g.* TiO and  $Ti_2O_3$  can be confirmed which is in consistent with the XRD data.

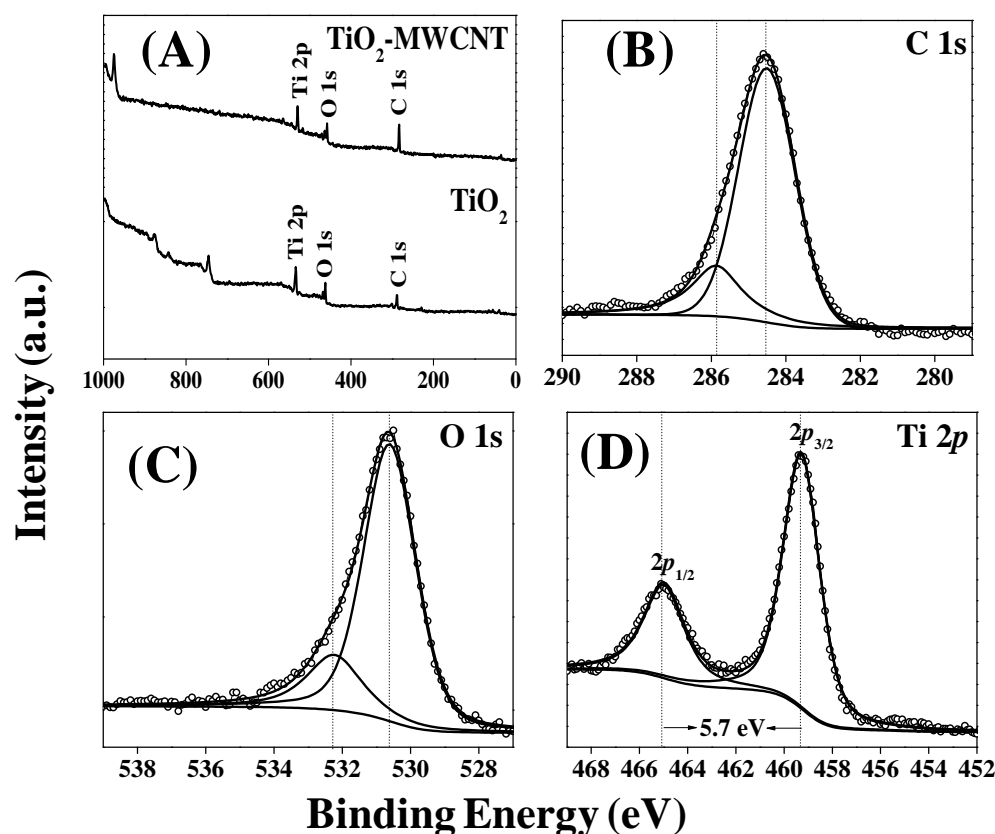


**Fig. 5.4:** (A) XPS survey spectra of  $TiO_2$  and  $TiO_2$ -MWCNT powder, (B) C 1s, (C) O 1s and (D) Ti 2p core level spectra of  $TiO_2$ -MWCNT powder.

### 5.3.4 TGA study

To know the amount of MWCNTs present in the as-synthesized composite, TGA was done in a constant airflow. Fig. 5.5 showed the TGA plot of MWCNT,  $\text{TiO}_2$  and  $\text{TiO}_2$ -MWCNT composite material. In case of MWCNTs, the curve began to decline at 380 °C and at 620 °C there was almost complete weight-loss due to the combustion of carbon in air. For the sample containing only  $\text{TiO}_2$ , the weight loss around 50 °C is due to the vaporization of water and further there was no weight loss. Similar weight loss  $\sim 50$  °C was also observed in  $\text{TiO}_2$ -MWCNT composite following the oxidation of MWCNT around 350 °C and it continued till  $\sim 620$  °C, forming  $\text{CO}_2$  attributed to the  $\sim 21\%$  weight-loss. Above 620 °C, the thermogravimetric curve exhibits nearly flat characteristic and no weight loss was further observed which proves that no residue of MWCNT was left to burn out, indicating the presence of only  $\text{TiO}_2$  residue in the composite.

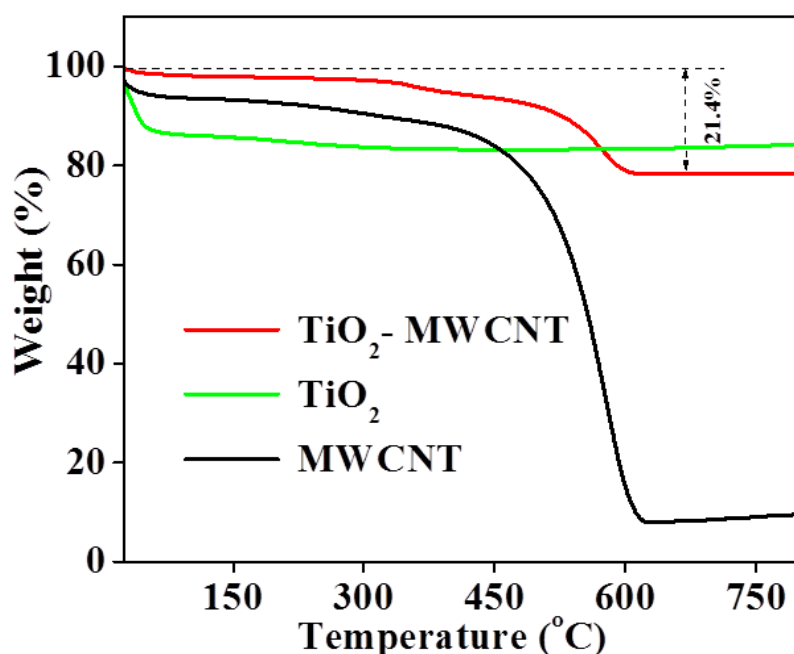
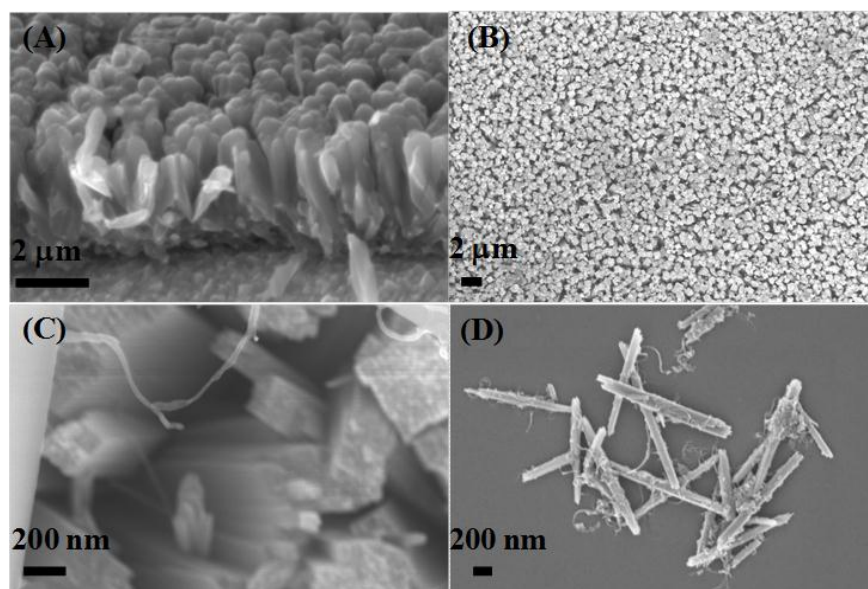


Fig. 5.5: TGA graph of  $\text{TiO}_2$ ,  $\text{TiO}_2$ -MWCNT powder and MWCNT.

### 5.3.5 FESEM study

In order to identify the morphology of the as-synthesized composites, FESEM was done. In Figs. 5.6 (A) and (B), the cross-sectional and top-view FESEM micrographs of the MWCNT-TiO<sub>2</sub> film on FTO substrate can be viewed, respectively. The rods in the as-grown 1D-composite were found to be closely packed and strongly aligned in the out of plane direction with respect to the substrate. The square shape top facets of the rods were the inveterate proof of the synthesis of tetragonal rutile structure. The whole substrate was uniformly covered with the 1D- composite film and the average length and diameter of the as-grown rods were 2 μm and 250 nm, respectively. The zoom view of the composite film (Fig. 5.6 (C)) clearly shows the entanglement of MWCNTs into the rods. Fig. 5.6 (D) showed the FESEM micrograph of as- synthesized TiO<sub>2</sub>-MWCNT powders, which also revealed the well-connected network of MWCNTs with TiO<sub>2</sub> rods.



**Fig. 5.6:** FESEM images of 1D rutile TiO<sub>2</sub>-MWCNT film directly grown on FTO (A) cross-sectional view, (B) top view (C) zoom view of (B) and (D) 1D rutile TiO<sub>2</sub>-MWCNT powder.

### 5.3.6 TEM analysis

To further get acquainted with the microstructure and formation niceties of the composite in more detail, TEM study was done. Figs. 5.7 (A)-(D) showed the TEM images of the as-synthesized 1D composite with different magnifications. It is cleared that in the composite MWCNT were interwoven with TiO<sub>2</sub> rods having diameter ~100 nm. The MWCNT properly bridged contact with the TiO<sub>2</sub> rods. The lattice fringes with interplanar distance of  $d_{220} = 0.16$  nm corresponding to the rutile phase of TiO<sub>2</sub> can be clearly distinguished (Fig. 5.8(A)). Further the fast Fourier transform (FFT) (Fig. 5.8 (A) inset) and sharp selected area electron diffraction (SAED) pattern of the nanorods can be visualized along  $[1\bar{1}0]$  zone axis, which proves the single crystalline nature of the nanorods. In Fig. 5.8(C), the reciprocal lattice points corresponding to the c-plane were masked and inverse FFT (IFFT) image was generated (Fig. 5.8 (D)) to acquire clearer structure with high crystallinity and minimal distortion.

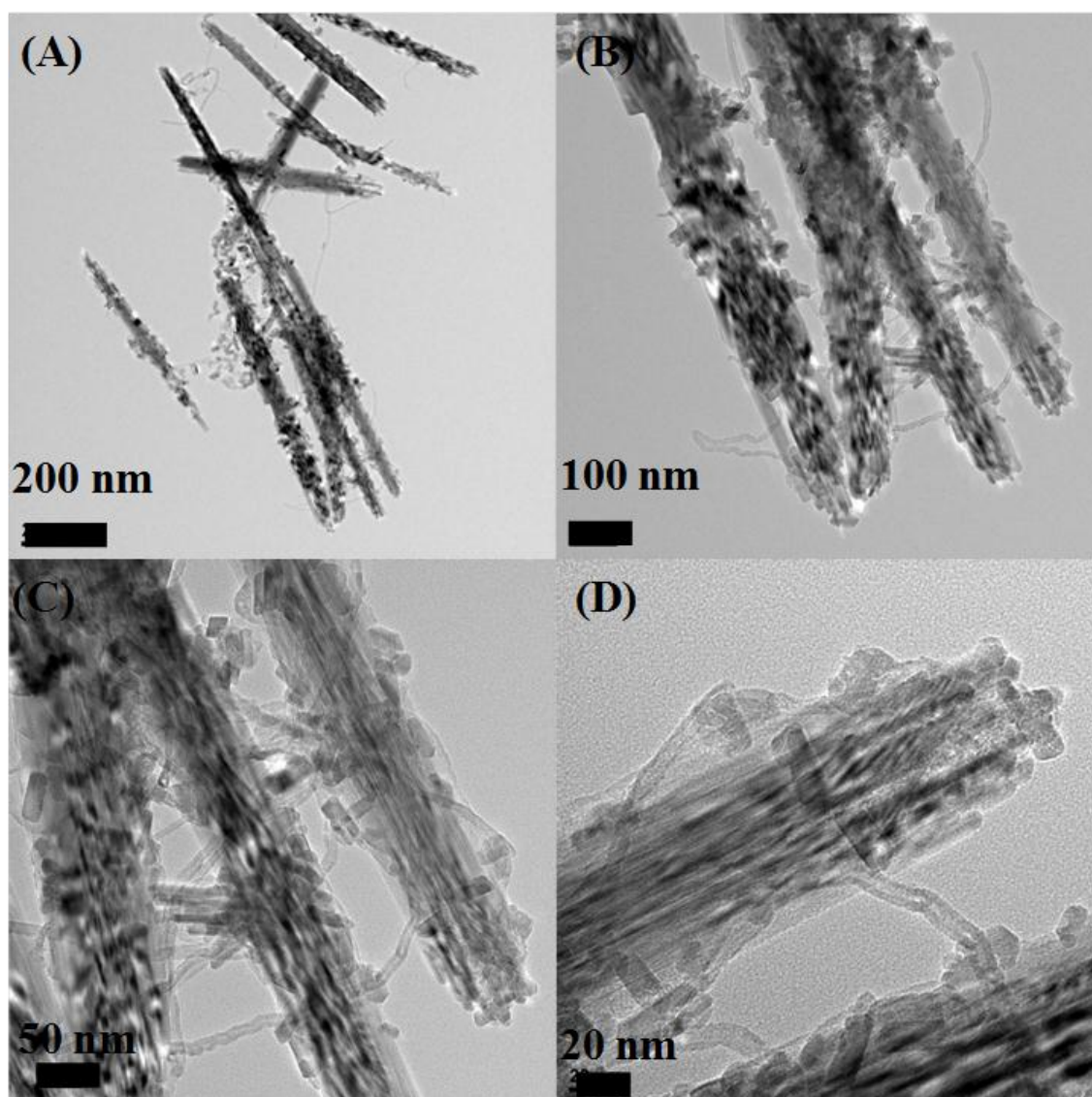


*Fig. 5.7: (A)–(D) TEM images of 1D-rutile  $\text{TiO}_2$ -MWCNT powder with different magnifications.*

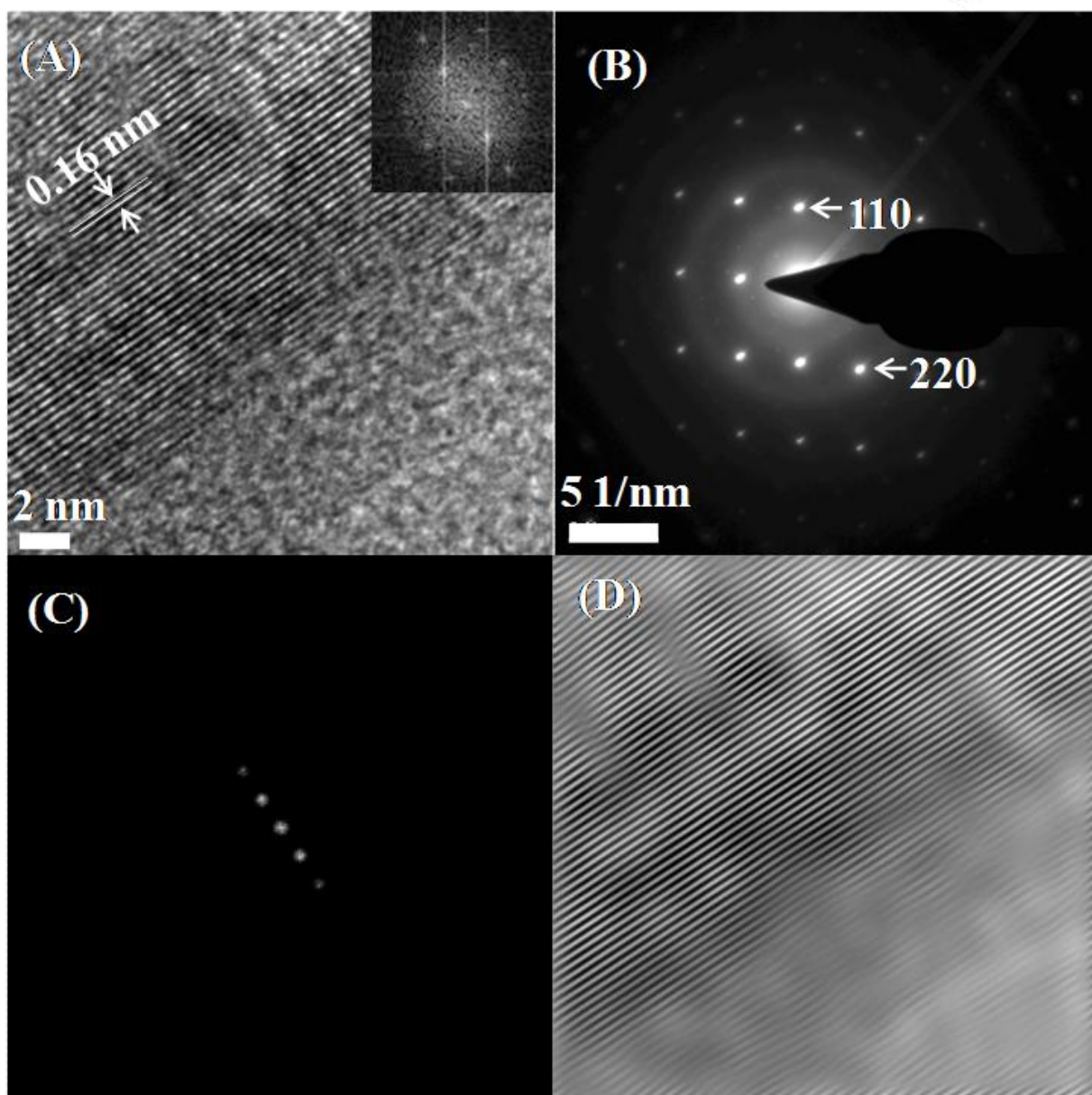


**Fig. 5.8:** (A) HRTEM image with inset showing FFT pattern, (B) SAED pattern of 1D-rutile  $\text{TiO}_2$ -MWCNT powder, (C) masked reciprocal lattice points corresponding to  $(110)$  plane and (D) Results of IFFT based on the lattice points shown in (C).

### 5.3.7 Optical properties

#### 5.3.7.1 UV-vis-DRS spectra

Further the optical properties of the as-synthesized samples were studied through UV-vis DRS and photoluminescence spectroscopy. In DRS spectra, both the samples exhibit an intense transition around ~400 nm as a consequence of electron transition from valence band to conduction band ( $O_{2p}-Ti_{3d}$ ) (Fig. 5.9).<sup>22</sup> It was cleared from the figure that the absorption capability of  $TiO_2$  was enhanced after incorporation of MWCNT. The enhancement of light absorption capability indicated the betterment of light harvesting potential.<sup>23</sup> It can be suggested that the surface electric charge on the oxides of the composite get enhanced due to the enhancement of absorption in the visible range which can modify the fundamental process of exciton formation. The spectrum of  $TiO_2$ -MWCNT underwent a ~ 10 nm red shift (from ~410 nm in only  $TiO_2$  to 420 nm in composite) due to the interaction between  $TiO_2$  and MWCNT and this implied a relative ease of charge transfer between CNT and  $TiO_2$ .<sup>21</sup> Assuming that the rutile  $TiO_2$  NRs possess a direct transition, the band edge energy of the as-synthesized NRs are calculated by plotting  $(\alpha hv)^2$  against  $hv$  (where  $\alpha$  is absorption coefficient and  $hv$  is photon energy). After calculating the band gap from the intercepts (Fig. 5.9) it is found that with inclusion of MWCNT a little amount of red shift take place from 3.0 eV to 2.9 eV.

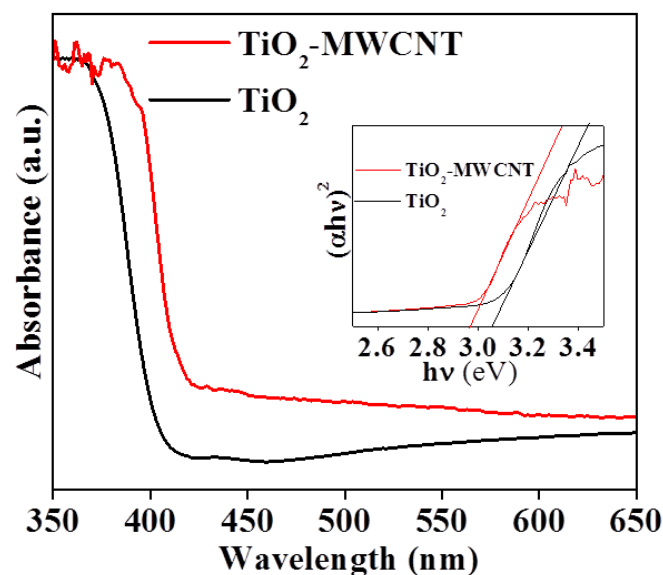


*Fig. 5.9 : (A) UV-vis-DRS spectra with inset showing the dependence of the absorption coefficient as a function of energy plot for TiO<sub>2</sub> and 1D rutile TiO<sub>2</sub>-MWCNT film.*

### 5.3.7.2 PL study

As PL emission occurs from the recombination of photogenerated charge carrier, so the study of PL spectra is useful to divulge the behavior of charge carrier trapping, separation and to understand the fate of excitons in semiconductor materials. Fig. 5.10 showed the room temperature PL spectra of TiO<sub>2</sub> and TiO<sub>2</sub>-MWCNT composite at a range from 400 to 650 nm, excited at the wavelength of 380 nm. Both the samples showed three emission spectra at 414, 434 and 460 nm respectively due to band-band emission and metal-ligand charge transfer transition.<sup>3</sup> The shapes of all the emission spectra were similar. There was a certain decrease in the intensity of the PL signal after incorporation of MWCNT which could be due to the electron transfer process from the conduction band of TiO<sub>2</sub> to MWCNT attributable to efficient charge separation.<sup>24</sup> The emission peaks were also slightly broadened in the composite. Several reasons could be found to explain the decrease in PL intensity. There might be a decline of radiative recombination process which is attributed to weak PL signal for

the composite.<sup>25</sup> MWCNTs encompass light harvesting property similar to dyes and they possess pi-conjugated structure which could make them an efficient electron accepting material and could obstruct the recombination of electron-hole pairs.<sup>16</sup> The efficient charge separation in the composite system will aid both the photovoltaic and photocatalytic properties of the material.

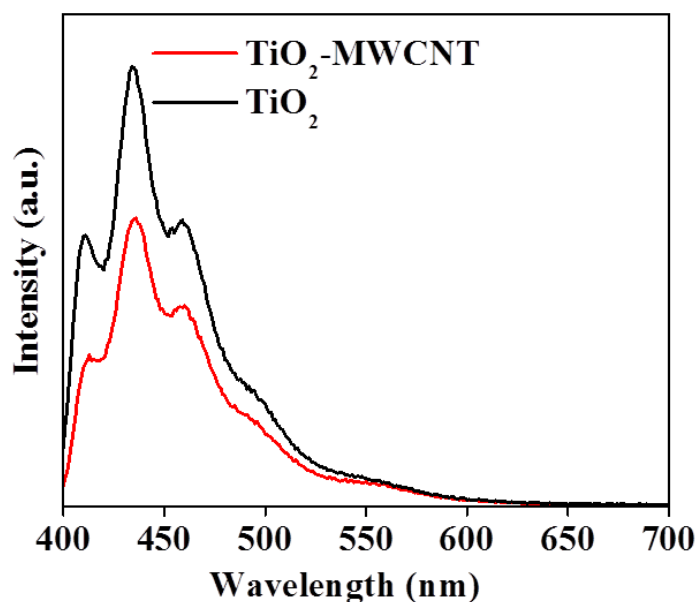


*Fig. 5.10: PL spectra of TiO<sub>2</sub> and 1D rutile TiO<sub>2</sub>-MWCNT film.*

### 5.3.8 Mott-Schotky study

Electrochemical impedance measurement is a common tool to study the transport properties of the semiconducting materials. The M-S plot, calculated from the electrochemical measurements provides a deep understanding of the materials composition and the nature of the donor levels. Fig. 5.11 showed the M-S plot of as-synthesized TiO<sub>2</sub> and TiO<sub>2</sub>-MWCNT NRs on FTO substrate. Both the samples exhibit positive slopes due to n-type semiconducting properties of TiO<sub>2</sub>. Compared to the only TiO<sub>2</sub> NRs, the composite materials showed much smaller slopes, which signify the increase in charge carrier density with inclusion of MWCNT. The flat-band potential ( $V_{FB}$ ) and carrier density of

the doped and undoped nanorods were calculated from M-S equation

$$\frac{1}{C^2} = \left( \frac{2}{e_0 \epsilon \epsilon_0 N_d} \right) \left[ (V - V_{FB}) - \frac{kT}{e_0} \right]$$

where  $e_0$  is the fundamental charge constant,  $\epsilon$  the dielectric constant of  $\text{TiO}_2$ ,  $\epsilon_0$  is the permittivity of vacuum,  $N_d$  the donor density,  $V$  the electrode applied potential,  $V_{FB}$  the flat-band potential and  $kT/e_0$  is a temperature-dependent correction term. The  $V_{FB}$  value of only  $\text{TiO}_2$  and  $\text{TiO}_2$ -MWCNT were determined to be -0.717 and -0.314 V respectively. The positive movement of the flat-band edge is probably due to the shift of the conduction band edge of the as-synthesized composite towards lower potential attributable to the incorporation of MWCNT. Thickness of the space-charge layer ( $W$ ) can also be calculated from the given equation

$$W = \left[ \frac{2\epsilon\epsilon_0(V - V_{FB})}{e_0 N_d} \right]^{1/2}$$

The charge carrier or donor density ( $N_d$ ) and thickness of the space-charge layer at the semiconductor/electrolyte interface of  $\text{TiO}_2$  and  $\text{TiO}_2$ -MWCNT was calculated to be  $6.1 \times 10^{16}$  and  $2.2 \times 10^{17} \text{ cm}^{-3}$  and 340 and 257 nm respectively. A potential of 1.0 V was chosen to calculate the space charge region. As the thickness of the space-charge region is smaller than the film thickness so there is a possibility to increase the photocurrent.<sup>26</sup>

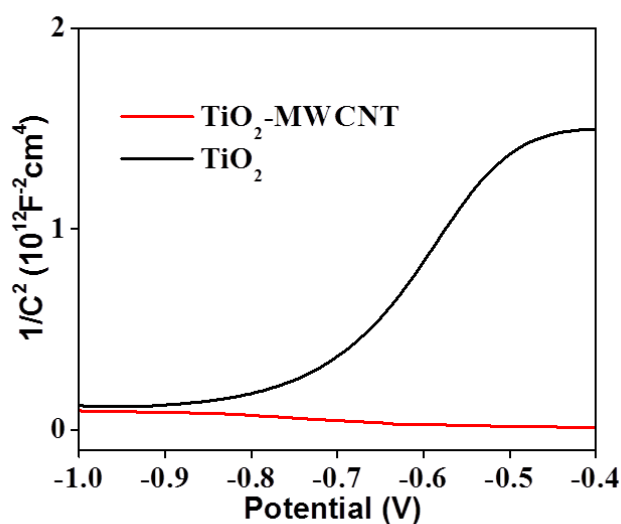


*Fig. 5.11: Mott-Schottky plots measured at a frequency of 10 kHz at 298 K in 3M KCl solution for  $TiO_2$  and 1D rutile  $TiO_2$ -MWCNT film.*

### 5.3.9 BET study

Oxides having higher specific surface area are always preferred for harvesting light due to the presence of more surface active sites leading to the enhancement of adsorption capacity of sensitized molecules. Hence, to study the effect of MWCNT intrusion on the specific surface area of the as-synthesized composite materials Brunauer–Emmett–Teller (BET) adsorption analysis was performed. According to Brunauer–Demming–Demming–Teller (BDDT) classification, the  $N_2$  adsorption-desorption isotherms (Fig.5.12) of  $TiO_2$  and composite nanorods can be attributed to type IV isotherms with  $H_2$  type hysteresis loop, indicating the presence of mesopores.<sup>23</sup> Using BET multipoint method, the specific surface area of  $TiO_2$  and  $TiO_2$ -MWCNT were found to be 24 and 50  $m^2/g$ , respectively. After incorporation of MWCNT the surface area of  $TiO_2$  was increased upto two times which also aid the rapid diffusion of charges.<sup>20</sup>

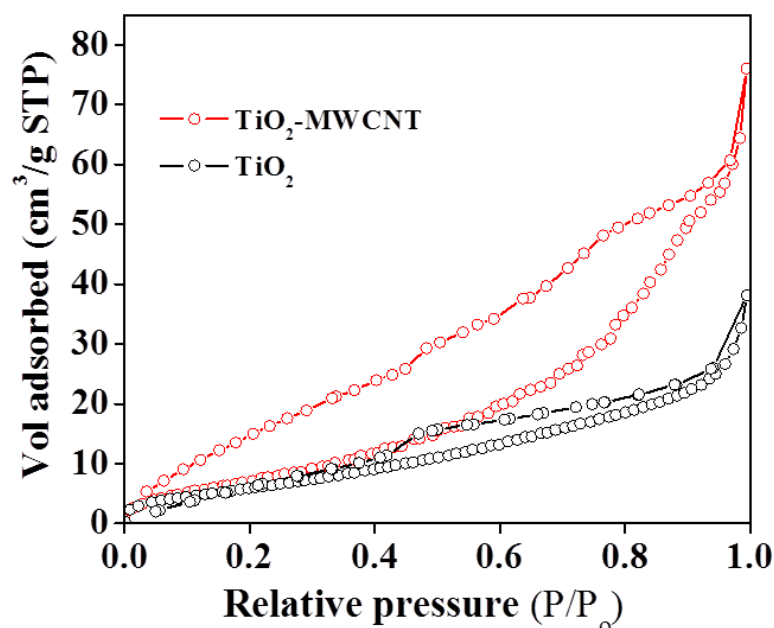
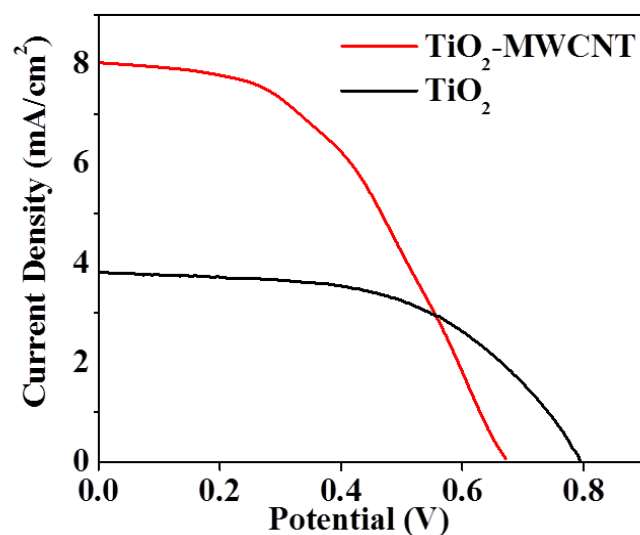


Fig. 5.12:  $N_2$  adsorption and desorption isotherm of  $TiO_2$  and 1D rutile  $TiO_2$ -MWCNT powder.

### 5.3.10 Photovoltaic study

To study the light harvesting property of the as-synthesized 1D  $TiO_2$ -MWCNT composite film, the material was sensitized with N719 dye. The photoelectric conversion measurements were done by fabricating a DSSC. The 1D, highly crystalline oriented composites, grown on FTO substrates can effectively act as photoanode in sensitized solar cells. As the composite film were directly grown on the transparent substrate, so there is an enormous possibility of increasing the generation of photoelectrons as more incident light can be passed through the backside of the photoelectrode. Fig. 5.12 showed the current density-voltage curves of the assembled solar cell under  $100 \text{ mW/cm}^2$  illumination using dye adsorbed  $TiO_2$  and  $TiO_2$ -MWCNT as photoanode. It was found that after incorporation of MWCNT, the photocurrent density ( $J_{SC}$ ) increased from  $3.94$  to  $7.49 \text{ mA cm}^{-2}$ , the open-circuit voltage ( $V_{OC}$ ), decreased from  $0.78$  to  $0.69 \text{ V}$ . The fill factor and the photon to electron

conversion efficiency of the composite increased from 0.49 to 0.52 and from 1.5 to 2.4 %, respectively. There can be few reasons behind the enhancement of  $J_{sc}$  and hence, the efficiency of the solar cell. The inclusion of CNTs into the  $TiO_2$  NRs favors faster transport and collection of photoexcited electrons from the dye to the electrode surface through the  $TiO_2$  network and hence increases the photocurrent density. Further, the rate of exciton recombination is also decreased due to better charge separation and transfer of a fraction of electrons from  $TiO_2$  to CNT.<sup>7</sup> Due to larger positive  $V_{FB}$  value of the composite materials (as calculated from the M-S plot), the effective driving force of the photoelectrons got enhanced which led to the augmentation of electron injection efficiency from the excited state of the dye to the semiconductor.<sup>27</sup> Moreover, due to the increase in the specific surface area of the material after incorporation of CNT, the amount of dye loading is also increased, leading to the increase in  $J_{sc}$  value. The decrease in  $V_{OC}$  value is due to the positive shift of the Fermi level, which can be known from the value of the  $V_{FB}$ . But, it is notable that despite the decrease in the  $V_{OC}$ , the overall efficiency of the DSSC increased by 60 % in the composite material compared to only  $TiO_2$  which supports the beneficial effect of inclusion of MWCNT into  $TiO_2$  nanorods.



**Fig. 5.13:** Current density vs. potential curves for dye-sensitized solar cell fabricated from  $TiO_2$  and 1D rutile  $TiO_2$ -MWCNT film.

### 5.4 Conclusion

In summary, in this contribution, we have synthesized oriented, single-crystalline, 1D rutile TiO<sub>2</sub>-MWCNT composite film on FTO substrates along with 1D rutile TiO<sub>2</sub>-MWCNT powder all in one step through a simple low temperature hydrothermal method. Formation of pure rutile phase and incorporation of MWCNTs with TiO<sub>2</sub> nanorods were confirmed through XRD, XPS and Raman analysis. Detailed optical studies revealed that the TiO<sub>2</sub>-MWCNT composite efficiently act as quencher and with incorporation of MWCNT, rate of recombination decreases and thus it could be efficiently used in photovoltaics and photocatalysis applications. Electrochemical impedance measurement was done to calculate the band edge position and electron carrier density of the composite material and found that the donor density was increased almost 10 times with incorporation of MWCNT in TiO<sub>2</sub> nanorod network. The composite film was successfully used as photoanode in a DSSC and the photon to electron conversion efficiency was increased by 60 % after inclusion of MWCNT. This simple hydrothermal synthesis of composite material can find a number of applications in not only photovoltaics or photocatalysis but also in lithium ion batteries, photonic crystals, self cleaning membranes and designing optoelectronics devices.

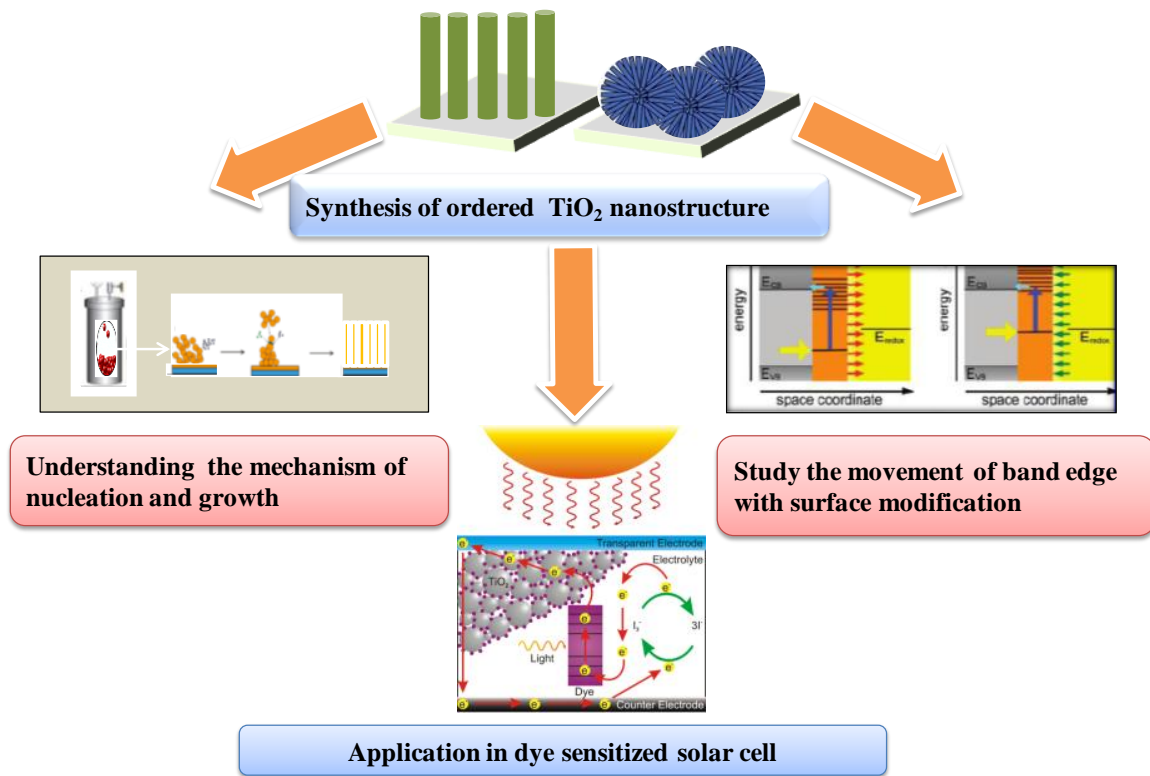
### 5.5 References

1. K. Woan, G. Pyrgiotakis, and W. Sigmund, *Adv. Mater.*, 2009, **21**, 2233–2239.
2. S. Muduli, W. Lee, V. Dhas, S. Mujawar, M. Dubey, K. Vijayamohanan, S.H. Han and S. Ogale, *ACS Appl. Mater.Interfaces.*, 2009, **1**, 2030–2035.
3. S. Sadhu and P. Poddar, *RSC Adv.*, 2013, **3**, 10363-10369.
4. Kongkanad, R. M. Dominguez, and, P. V. Kamat, *Nano Lett.* 2007, **7**, 676–680.
5. A. Kongkanad, and, P. V. Kamat, *ACS Nano*, 2007, **1**, 13–21.
6. S. Iijima, *Nature*, 1991, **354**, 397-399.
7. C. Yen, Y. Lin, S. Liao, C. Weng, C. Huang, Y. Hsiao, C. Ma, M. Chang, M. H. Shao, M. Tsai, C. Hsieh, C. Tsai, and F. Weng, *Nanotechnology*, 2008, **19**, (9pp).
8. K.M. Lee, C.W. Hu, H.W. Chen and K.C. Ho, *Sol. Energy Mater. Sol. Cells*, 2008, **92**, 1628–1633.
9. T.Y. Lee, P.S. Alegaonkar and J.B. Yoo, *Thin Solid Films*, 2007, **515**, 5131–5135.
10. Z. Peining, A. S. Nair, Y. Shengyuan, P. Shengjie, N. K. Elumalai and S. Ramakrishna, *J. Photochem. Photobiol., A*, 2012, **231**, 9-18.
11. K. Zhu, N. Neale, A. Miedaner and A. Frank, *Nano Lett.* 2007, **7**, 69–74.
12. G. Zoppi, K. Durose, S. Irvine and V. Barrioz, *Semicond. Sci. Technol*, 2006, **21**, 763-770.
13. Z. Sun, J. Kim, Y. Zhao, F. Bijarbooneh, V. Malgars, Y. Lee, Y. Kang and S. Dou, *J. Am. Chem. Soc.*, 2011, **133**, 19314-19317.
14. S. Amin, A. Nicholls and T. Xu, *Nanotechnology*, 2007, **18**, 445609 (5pp).
15. J. Yu, T. Ma, and S. Liu, *Phys. Chem. Chem. Phys.*, 2011, **13**, 3491-3501.
16. L. Gu, J. Wang, H. Cheng, Y. Zhao, L. Liu, and X. Han, *ACS Appl. Mater.Interfaces.*, 2013, **5**, 3085–3093.
17. Y. Zhu, H. I. Elim, Y. L. Foo, T. Yu, Y. Liu, W. Ji, J. Y. Lee, Z. Shen, A. T. S. Wee, J. T. L. Thong and C. H. Sow, *Adv.Mater.*, 2006, **18**, 587-592.

18. C. Y. Yen, Y. F. Lin, C. H. Hung, Y. H. Tseng, C. C. M. Ma, M. C. Chang, and H. Shao, *Nanotechnology*, 2008, **19**, 045604 (11pp).
19. F. X. Xiao, J. Miao, H. Y. Wang and B. Liu, *J. Mater. Chem. A*, 2013, **1**, 12229-12238.
20. M. Y. Ryu, K. N. Jung, K. H. Shin, K. S. Han, and S. Yoon, *J. Phys. Chem. C*, 2013, **117**, 8092–8098.
21. S. Zhang, H. Niu, Y. Lan, C. Cheng, J. Xu, and X. Wang, *J. Phys. Chem. C*, 2011, **115**, 22025–22034.
22. Y.J. Xu, Y. B. Zhuang and X. Z. Fu, *J. Phys. Chem. C*, 2010, **114**, 2669-2676.
23. J. Yu, J. Fan and B. Cheng, *J. of. power. Sources.*, 2011, **196**, 7891-7898.
24. Z.Peining, A. S. Nair, P. Shengjie, Y. Shengyuan and S. Ramakrishna, *Appl. Mater. Interfaces*, 2012, **4**, 581-585.
25. J. G. Yu, L. Yue, S. W. Liu, B. B. Huang and X. Y. Zhang, *J. Colloid Interface Sci.*, 2009, **334**, 58–64.
26. A. Wolcott, W. A. Smith, T. R. Kuykendall, Y. Zhao, and J. Z. Zhang, *small*, 2009, **1**, 104 - 111.
27. J. Liu, H. Yang, W. Tan, X. Zhou, and Y. Lin, *Electrochimica Acta*, 2010, **56**, 396-400.

# Chapter VI

## Conclusion



## **Outline**

---

This chapter describes the brief summary of the results achieved during the thesis work and the future scope for possible further research.

---

### 6.1 Summary of the work

Among different types of nanostructures, one-dimensional (1D) rods or wires of titania are extremely important owing to their unique optoelectronic properties which arise as a result of their anisotropic shape. Single-crystalline semiconductors, directly grown on transparent conducting oxide (TCO) glass substrates, transport electron faster due to the absence of grain boundaries and reduced electron trap sites. In order to control the charge separation and recombination kinetics of these 1D nanostructures, it is essential to study the nucleation and growth mechanism of these NCs in detail. We have studied the growth mechanism of single-crystalline titania NRs on various substrates. Our results show strong influence of the crystallinity of the substrate layer on the crystallinity of the as-grown TiO<sub>2</sub> NRs where we could fabricate TiO<sub>2</sub> NRs in two different planes if the characteristic of the substrate is changed from crystalline to amorphous. We also demonstrate that it is possible to tune the diameter of the titania NRs by further coating the FTO substrates with thin gold layer which results in an increase in the hydrophilicity of the substrates.

Due to the combination of micro and nanometer scale building-blocks, 3D-structures composed of several 1D units show distinctive properties compared to only 1D structures. After studying the nucleation and growth mechanism of oriented titania NRs on TCO substrates, we planned to synthesize oriented, template-free, rutile 3D microspheres, composed of bundles of single-crystalline NWs, directly on FTO substrates through a simple, low-temperature, surfactant-free hydrothermal method. The effect of titanium precursor on the formation morphology of the microspheres has also been studied and it was found that, for the synthesis of TiO<sub>2</sub> microspheres, simultaneous addition of two precursors is required. The time dependent growth of TiO<sub>2</sub> microspheres has also been investigated. Detailed optical

studies revealed that the microspheres grown on FTO substrates after 10 h of reaction time showed effective light scattering, leading to the better harvesting of photon. The rutile TiO<sub>2</sub> microspheres have been successfully used as photoanode and as DSSC. The as-grown microspheres on FTO for 10 h showed significant improvement of photon to electron conversion efficiency (45%) due to the synergistic effect of larger surface area and enhanced photon scattering compared to 2 h growth. The photocatalytic activity of the as-synthesized microspheres was also explored for the first time and it was found that the activity remained almost unchanged upto three consecutive cycles. Moreover, The microsphere film showed superhydrophilicity without any prior UV irradiation. Due to the presence of bundles of almost parallel nanowires, micro-capacitors were generated which showed stable dielectric performance.

The Ti<sup>4+</sup> ions in TiO<sub>2</sub> have emblematic electronic configuration for which incorporation of atomic impurity can tailor the band gap and electrical conductivity of titania. Therefore, we have tried to dope lanthanum homogeneously in single crystalline TiO<sub>2</sub> NR-arrays. The homogeneous distribution of lanthanum in titania lattice is confirmed by STEM elemental mapping and line scanning analysis. After doping with lanthanum, there is a negative shift of the flat-band potential of the TiO<sub>2</sub> NRs. For the first time, we have synthesized oriented, single-crystalline, La-doped TiO<sub>2</sub> NRs directly on FTO substrates through a simple, low-temperature hydrothermal method and performed detail optical studies of the doped and undoped rutile titania NRs. The La-doped TiO<sub>2</sub> NRs have been successfully used as photoanode in DSSC. Photon to electron power conversion efficiency was increased 21 % after doping the TiO<sub>2</sub> NRs with 4 mol% lanthanum.

In another approach to further modify the electrical conductivity and optoelectronic properties of these 1D titania nanostructures, synthesis methods of hybrid structures were

developed. Carbon nanotubes (CNT) are used as semiconductor support owing to their unique electronic properties and wide electrochemically stable window. Besides, due to the ease of surface-functionalization and superior electronic properties of MWCNTs, the incorporation of MWCNTs into  $\text{TiO}_2$  has attracted the attention of researchers worldwide. We have synthesized oriented, single-crystalline, rutile  $\text{TiO}_2$  NRs-MWCNT composites directly on FTO substrates along with 1D-rutile  $\text{TiO}_2$ -MWCNT composite powder through a simple low temperature hydrothermal method and calculated the change of flat-band potential ( $V_{\text{FB}}$ ) and carrier density of the  $\text{TiO}_2$  NRs with incorporation of MWCNTs through Mott-Schottky measurement. The donor density increased by almost 10 times with the incorporation of MWCNTs in the  $\text{TiO}_2$  NR network leading to enhanced transport properties. Detailed optical studies revealed that the  $\text{TiO}_2$ -MWCNT composites efficiently act as a quencher and with the incorporation of MWCNTs, the rate of recombination decreases and thus, these composites can be efficiently used in photovoltaics and photocatalysis applications. The rutile  $\text{TiO}_2$  NRs-MWCNT composites film has been successfully used as photoanode in DSSC. Photon to electron power conversion efficiency increased 60 % after incorporation of MWCNTs into the  $\text{TiO}_2$  NRs.

### 6.2 Scope for future study

During my PhD work, there are some unanswered questions, which need to be answered. We have synthesized oriented  $\text{TiO}_2$  NRs on FTO substrates. It is assumed that as there is a very little lattice mismatch between the FTO substrate and rutile titania, oriented growth is taking place. But recently oriented anatase  $\text{TiO}_2$  NRs were also synthesized directly on FTO substrates and surprisingly lattice mismatch between anatase titania and FTO substrate is more than 15 %. So, further study is required to know the exact reason behind the

motive of oriented growth, whether the growth is caused by epitaxy, anisotropy or there are other reasons. Still, it is very difficult to synthesize desired faceted and hybrid titania structures due to lack of knowledge of nucleation and growth mechanism at the seed level. Therefore, to achieve the control for synthesis of titania nanostructures, with the desired facet and shape, further research is required to study the growth mechanism at molecular stage. Various methods, like combination of *in situ* microscopy with dynamic and static light scattering, along with fluorescence correlation spectroscopy, is required to understand the apposite growth mechanism of titania NCs in molecular echelon. For that, simulation study is also required. In order to study different 3D-assembly, it is obligatory to know how blending of different polar and nonpolar solvents occur at the interface as for the growth of 3D-assembly, interface of the solvents plays a major role owing to deviation of surface energy from the bulk phase and variation in Hansen solubility parameter. It is also required to know whether changing the polarity of the solvent, to achieve the desire phase, can vary the ratio of anatase to rutile. It is known from the literature that lanthanum inhibits the growth of titania NCs and in our experiment we also observed that the density of the doped NRs grown on FTO substrate decreases as the amount of lanthanum increase in the solution. But still, the proper reason behind the inhibition of growth of titania NRs in addition of lanthanum is not cleared.

Till now, the band edge shift picture of titania nanostructures with doping of anion and cation is not cleared completely. It is also required to know how the shifting of band edge takes place with interstitial and substantial doping and how the shifting is affected by the presence of oxygen vacancy. Transport property of electrons through a single nanorod needs to be explored further. The exact position and presence of oxygen vacancies can be clearly understood through the aberration corrected high resolution TEM. To know the presence of

vacancy-type crystalline defects in as-synthesized NRs, the study of positron lifetime and Doppler broadening spectroscopic measurements are needed to be executed.

Nanobranched semiconductor structures are capable to attain fast electron transport in order to improve charge collection competence. To increase the overall efficiency of a sensitized solar cell, it is imperative to chemically synthesize the combination of two different metal oxide materials in a tree like nanostructure, where, one material will stand like the stem of the tree and the other one will be similar to the branch for better cell recital. ZnO is highly favorable material for application in DSSC, since it can be grown in single crystalline NRs using facile methods and having very high electron mobility comparable to TiO<sub>2</sub>. However, the main disadvantage of ZnO is that dyes partially dissolve the ZnO and form a harmful Zn<sup>2+</sup>-dye surface complex. The TiO<sub>2</sub> NPs provide a superior surface for the dye-attachment compared to ZnO. So, combination of these two oxides will provide fast transport of electrons as well as better attachment of dye.

Above all, the simple, low temperature, surfactant free synthesis method for synthesis of 1D titania and modified titania nanostructures directly on substrates has huge applications in different types of photoelectrochemical as well as optoelectronic devices which further needs to be explored.

## **List of publications**

1. “Surface Chemistry, Growth Mechanism of Highly Oriented, Single crystalline TiO<sub>2</sub> Nanorods on Transparent Conducting Oxide Coated Glass Substrates”, **Subha Sadhu**, Adhish Jaiswal, Suguna Adyanthaya and Pankaj Poddar\*, *RSC Adv.*, **2013**, 3, 1933–1940.
2. “Growth of oriented single crystalline La-doped TiO<sub>2</sub> nanorod arrays electrode and investigation of optoelectronic properties for enhanced photoelectrochemical activity”, **Subha Sadhu** and Pankaj Poddar\* *RSC Adv.*, **2013**, 3, 10363–10369.
3. “Modulation of reaction kinetics allows tunable synthesis of Au NP and QCs: Application of Au QC as turn-off sensing probe for Sn<sup>4+</sup> ions”, Puneet Khandelwal, Dheeraj K. Singh, **Subha Sadhu** and Pankaj Poddar\*, *ChemPlusChem.*, **2014**, 79, 134 – 142.
4. “Template Free One Pot Synthesis of Oriented Single Crystalline 1D Rutile TiO<sub>2</sub>-MWCNT Composite for Enhanced Photoelectrochemical Activity”, **Subha Sadhu** and Pankaj Poddar\*, *J. Phys. Chem. C*, **2014**, 118, 19363–19373.
5. “Photoelectrochemical & Photocatalytic Applications of Superhydrophilic, Oriented, Single-crystalline, Surfactant-Free, 3D-TiO<sub>2</sub> Microsphere Arrays on Transparent Conducting Oxide Substrate”, **Subha Sadhu** and Pankaj Poddar\*(communicated)